TRANSIENT DYNAMICS OF NONLINEAR OSCILLATORS WITH APPLICATIONS TO CENTRIFUGAL PENDULUM VIBRATION ABSORBERS

By

Ryan James Monroe

A DISSERTATION

Submitted to
Michigan State University
in partial fulfillment of the requirements
for the degree of

DOCTOR OF PHILOSOPHY

Mechanical Engineering

2011

ABSTRACT

TRANSIENT DYNAMICS OF NONLINEAR OSCILLATORS WITH APPLICATIONS TO CENTRIFUGAL PENDULUM VIBRATION ABSORBERS

By

Ryan James Monroe

We consider the transient behavior of centrifugal pendulum vibration absorbers (CPVAs), specifically, the overshoot problem encountered when these absorbers are suddenly activated. CPVAs are passive devices used to address torsional vibrations in rotating systems, for example, helicopter rotors and crankshafts of internal combustion engines. They consist of pendulums mounted on a rotor, driven by system rotation, and tuned in such a manner that in steady-state operation they counteract engine-order fluctuating torques acting on the rotor, thereby smoothing vibrations. The primary feature of these devices is that they are order tuned, that is, tuned to a given multiple of the rotation rate, as opposed to the more common frequency tuned absorbers. Recently these absorbers have been proposed to expand the operating envelope for cylinder deactivation in variable displacement engines, in order to improve fuel economy. In these applications, the system encounters conditions in which the absorbers are suddenly activated and undergo a beating-type transient motion, resulting in overshoot of the absorber amplitude before it reaches steady-state. This overshoot depends on a number of parameters, including the difference between the absorber's natural frequency and the frequency of excitation, the ratio of absorber inertia to rotor inertia, the system damping, and system nonlinearities. An approximate analytical model is developed, using perturbation methods, that predicts the overshoot in terms of these parameters, and the model results are verified by simulations of the equations of motion and by experiments

using a fully instrumented spin rig. The predictive results are found to provide a useful bound on the overshoot, and will be of use when designing absorber systems so that they do not exceed rattle space constraints during startup. It is found that absorbers with near tautochronic paths behave much like linear absorbers, and when lightly damped and start from small initial conditions, they have an overshoot close to 100%. For absorbers with softening paths, such as the commonly used circular path absorbers, the overshoot can reach up to 173%, depending on system and input parameters.

To my wife, Anna, and my family

ACKNOWLEDGMENT

I would like to thank my wife, Anna, for her support during my time as a graduate student; her encouragement during the last five years has been instrumental in my success. In addition, I would like to thank my family for their constant support and encouragement. I would like to acknowledge my advisor, Steve Shaw, whom I simply cannot thank enough. I am truly grateful to have been given the opportunity to work under his guidance on such a fascinating topic. It has been a pleasure to work for him at Michigan State University, where I have learned and grown so much over the last three years as a doctoral student.

Many thanks to Alan Haddow, Pete Schmitz, and Nate Verhanovitz for their assistance with the experimental rig, and Bruce Geist, Brendan Vidmar, and Brian Feeny for the many fruitful discussions. Thanks go to Ranjan Mukherjee and Hassan Khalil for being a part of my committee. I am grateful for Neil Wright and Tom Pence for their mentorship during my first two years as a masters student. I would also like to acknowledge my fellow lab mates (both past and present) of the vibrations lab, including Nick Miller, Venkat Ramakrishnan, Thomas Theisen, Scott Strachan, Carl Coppola, and Rickey Caldwell. Thanks also to Clifford E. Weil for his LaTeX files that met the Graduate School formatting requirements. Many thanks to the wonderful Mechanical Engineering staff, which includes: Suzanne Kroll, Aida Montalvo, Mary Pease, and Lindsay Niesen. The work associated with this dissertation was supported by grants from the National Science Foundation (CMMI-0700307) and Chrysler Group, LLC. Additional support came from the Graduate School Dissertation Completion Fellowship.

TABLE OF CONTENTS

LIST OF TABLES

LIST OF FIGURES

Chapter 1

Introduction

Centrifugal Pendulum Vibration Absorbers (CPVAs) are passive devices used to address torsional vibrations in rotating systems, for example, helicopter rotors [77] and internal combustion engine crankshafts [55]. As shown in Fig. 1.1 (a), a CPVA consists of a pendulum mounted on a rotor, driven by system rotation, and tuned in such a manner that in steady-state operation the system dynamics lead to a torque from the pendulum that counteracts engine-order fluctuating torques acting on the rotor, thereby smoothing rotor torsional vibrations. Multiple CPVAs are placed around a rotor for balancing, and each is typically constructed using a bifilar (two point) suspension, as shown in Fig. 1.1 (b). These absorber designs consists of the following essential components: an absorber mass (D) and two rollers (A), which suspend the absorber from a flange (C) that is fixed to the rotor. The rollers ride on surfaces (B) on the absorber and flange, which are identical but inverted, and are machined so that the absorber follows a user-designed path. This path, along with the absorber mass and placement (distance from the rotor center), are the essential design ingredients for an absorber system. For example, Fig. 1.1 (c) shows an implementation of

four absorbers mounted on a helicopter rotor, for which the absorbers follow a cycloidal path [38]. In this chapter we describe some current motivations for using CPVAs in automotive engines, provide a basic description of how they work, and include a discussion of previous work in the area.

1.1 Motivation

As pressures to improve fuel economy and reduce emissions continue to increase [1], cylinder deactivation, which shuts down inessential cylinders during low-power operating conditions, remains a viable technology. The fuel savings for these engines is typically in the 5-10% range, accruing from reductions in pumping losses [22]. However, there is a current limitation on the range of engine speeds over which one can deactivate cylinders, and this is limited on the low-rpm end primarily by vibration issues. Therefore, if absorbers can be designed such that they reduce torsional vibration (in the cylinder deactivated mode), then one can expand the engine speed range over which the engine can deactivate cylinders, resulting in additional fuel savings. Absorber design considerations for steady-state operation are already well understood, and have proven to work well, even down to idle speeds for a prototype V8/V4 engine [55]. However, transient absorber motions, specifically, those induced by abrupt transitions from full cylinder (non-resonant excitation) to reduced cylinder (resonant excitation) are not well understood, and the issues associated with these transient responses, for example, bumper impacts and non-synchronous responses, are directly relevant to the acceptance and implementation of CPVAs in these engines. Furthermore, a literature search on analytical treatments of transient dynamics in nonlinear systems turned up only a handful of publications [2, 15, 20, 32, 39, 42, 64], and none have considered the percent overshoot

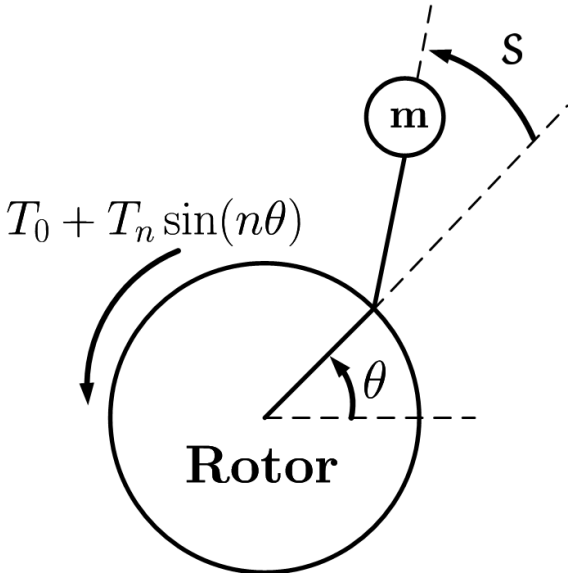

(a)

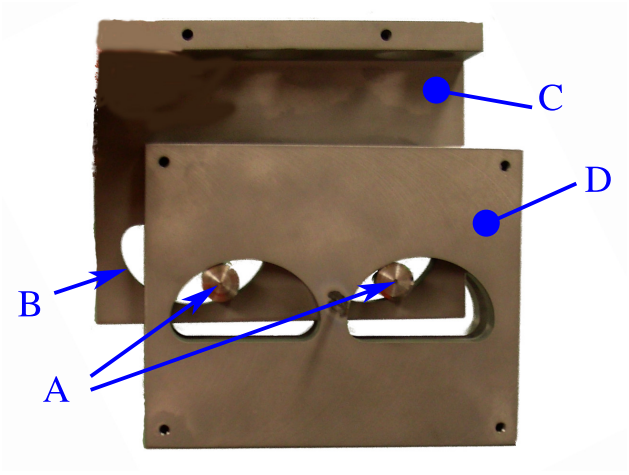

(b)

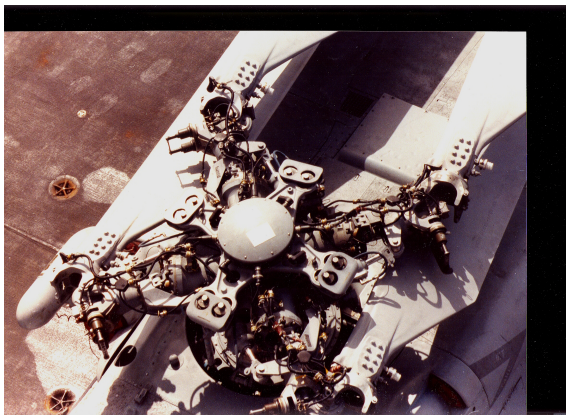

(c)

Figure 1.1: (a) Depiction of the basic CPVA model, consisting of a pendulum (absorber) attached to a rotor, which is driven by a mean torque and and fluctuating torque of order n. (b) The basic elements of a bifilar absorber shown in a deflected (off-center) position (the device shown was designed and fabricated by Chrysler for experimentation in the MSU lab); elements A are the rollers used for the bifilar suspension, B is one of the machined surfaces that dictates the path followed by the absorber, C is a flange that is attached to the rotor, and D is the absorber mass; note that the machined surfaces on the flange and absorber are identical but inverted. (c) Helicopter rotor with 4 bifilar absorbers attached (photo by S. Shaw, aboard the USS Nimitz, 1991). *For interpretation of the references to color in this and all other figures, the reader is referred to the electronic version of this dissertation.*

of a nonlinear oscillator suddenly subjected to harmonic excitation, which is precisely the information needed for the current investigation.

Successful reduction of torsional vibrations using CPVAs has other applications for improving fuel economy. Several automotive manufacturers are working to develop high-torque, fuel-efficient, four-cylinder engines, which typically operate with high compression ratios and at low speeds, which inherently lead to large torsional oscillations. These engines can be more aggressively tuned for fuel economy, for example, by running at lower engine speeds, if torsional vibration issues are addressed. Also, in cars with automatic transmissions, the torque converter is the source of significant losses. When the torque converter is locked there is an essentially rigid link between the engine and wheels, which minimizes these losses. The ability to initiate torque converter lockup is dictated by the level of torsional vibrations between the engine and downstream powertrain components, and thus improved efficiency of the powertrain can be achieved if one can reduce engine torsional vibrations. Another feature of future engines that is relevant to transient absorber response is that of start-stop technology, which stops the engine entirely for zero load conditions, for example, when stopped at traffic lights. These engine technologies provide transient environments under which the absorbers must be able to survive without unwanted dynamics.

Thus, the primary goal of this work is to develop a fundamental understanding of the transient dynamics in nonlinear systems, so that it can be applied to the design of absorber systems for automotive applications. Thus, a systematic analytical and experimental study of transient absorber response is carried out for a parameterized family of absorber paths that includes those of practical interest. This is accomplished by building on the current knowledge of absorber responses, including work on linear and nonlinear absorber models [58,

59, 69], as well as taking advantage of the existing experimental facility used in previous studies [26, 52, 53, 70].

The main technical results of this dissertation are organized around chapters on various topics, as follows: in Chapter 2 we improve the absorber system model by accounting for the roller dynamics and investigating the effects of the rollers on system response and performance; in Chapter 3 we derive an analytical method for the computing the percent overshoot of a nonlinear Duffing oscillator subject to a suddenly applied harmonic force with general initial conditions, and testing the results against simulations; in Chapters 4 & 5 we apply the analytical results to CPVA models, including theoretical predictions compared with simulations (Chapter 4), and experimental verification (Chapter 5) for circular path and near tautochronic path absorbers.

1.2 Basic Operation of a CPVA

In an internal combustion engine, engine-order fluctuating torques are a result of the net torque applied to the crankshaft as each cylinder fires in succession as the crank rotates. In many situations, this applied torque is dominated by a mean component T_0 and the first harmonic of order n, $T_n \sin n\theta$, where $\theta \approx \Omega t$ and Ω is the mean rotor speed and n is the order of excitation. [1] For example, for a four-stroke engine with K cylinders, $n = K/2$. The order of excitation n has the same connotation as an angular frequency, except that n is dimensionless. The mean torque T_0 maintains the mean rotor speed Ω, and the fluctuating excitation torque produces torsional oscillations about this mean speed. If an absorber can

[1] Higher harmonic torques, at orders $2n$, etc., exist, but their amplitudes are generally negligible in comparison to the first and are often ignored in practice.

be tuned correctly, it will respond to this excitation and produce a counter-torque, thereby reducing torsional oscillations of the rotor. The primary feature of CPVAs is that they are order tuned, as opposed to the more common frequency tuned absorbers, so that the absorber's natural frequency ($\omega_a = \tilde{n}\Omega$) stays tuned relative to the excitation frequency ($\tilde{n} \approx n$) at all engine speeds (Ω). Therefore, the absorber is effective at reducing torsional vibrations across an entire range of rotor speeds. In contrast, a frequency tuned device can be tuned only to a single rotor speed.

In order for a CPVA to be effective at reducing the torsional vibration of the rotor, the absorbers tuning order should be near to, or slightly greater than, that of the excitation order, that is, $\tilde{n} \approx n$ with $\tilde{n} \geq n$; this is referred to as over-tuning [31]. This tuning results in steady-state operation in which the absorber response is *out of phase* relative to the excitation torque, which reduces torsional vibrations of the rotor. If one under-tunes an absorber, it is closer to the absorber/rotor system resonance and its amplitude grows rapidly as the torque is increased, leading more quickly to nonlinear behavior. A possible disastrous nonlinear behavior is the jump bifurcation that results in large amplitude steady-state absorber response that is *in phase* relative to the excitation, resulting in amplification of rotor torsional vibrations [5,56]. Another important nonlinear effect is symmetry-breaking bifurcations in systems composed of multiple absorbers [4,5,11,68]. All of these bifurcations are possible due to the system nonlinearities that arise from both the absorber path, as well as the kinematic coupling to the rotor.

The absorber natural frequency of oscillation is determined by its free vibration response when the rotor spins at a constant speed Ω; this frequency is proportional to Ω and generally depends on amplitude through nonlinear effects determined by the absorber path. This

frequency consists of a linear part $\tilde{n}\Omega$, determined by the curvature of the path at its vertex, and a nonlinear part dictated by a parameter λ that describes how the path curvature varies as a function of travel along the path. The restoring force acting on the absorber is the component of the centrifugal load tangential to the absorber path, and the path curvature determines the nature of this force. For instance, a circular path, which has constant curvature, results in an oscillator containing a nonlinear softening restoring force (that is, the effective stiffness decreases as a function of amplitude), resulting in a softening nonlinear dynamic response. As one might expect, there exists a path which results in a linear restoring force, resulting in a simple harmonic response for all amplitudes; this path is referred to as the *tautochronic* path, and is known to be a particular epicycloid. Section 2.2.1 provides more details about the path parameters and their geometric interpretation. Paths also exist which exhibit nonlinear hardening restoring forces, such as the cycloidal path described in the patent by Madden [38]. Denman [17] has introduced a very convenient framework for describing paths that include circles, cycloids, and epicycloids, using a two parameter ($\tilde{n}$ and λ) path, as described in Section 2.2.1.

The path nonlinearities described above directly affect the forced response of the rotor/absorber system. However, in the forced vibration case, the excitation acts on the rotor, and rotor/absorber inertial coupling comes into play, which results in additional system nonlinearities. For circular path absorbers, the path nonlinearity is dominant over a large range of absorber motions. However, for the tautochronic path, which has a neutral path in terms of nonlinearity, the system is slightly softening as a result of kinematic coupling to the rotor. However, when the rotor is driven, the effect of the applied torque is reduced at large amplitudes by kinematic effects, with the net effect being an overall slight hardening behavior

for forced vibration [49]. In addition, for all absorbers, the response is also affected by the dynamics of the rollers, which introduce additional kinematic path nonlinearities through their inertia. Lastly, the situation can become even more complicated when multiple absorbers are attached to a rotor [4, 5, 11, 68]. For such systems the absorbers can exhibit non-synchronous steady-state responses, even when the absorbers are identical [4, 5, 11, 68]. Therefore, it is important to understand how system parameters and nonlinearities affect the dynamic response, so that these systems can be designed to operate effectively in a passive manner.

1.3 Background

CPVAs have been in use for about 100 years, and studied scientifically for about 80 years. The contributions, in chronological order, go from initial experimentation and implementation in industrial applications, to linear modeling of the steady-state response, and finally to the more recent contributions about the nonlinear steady-state response, both analytically and experimentally; this history is briefly summarized below. Up to the present, the focus has always been on the steady-state response, which is applicable in aerospace applications. However, the renewed interest in automotive applications has raised the issue of system transient response, and that is the main thrust of the study described herein.

Our knowledge of absorber system dynamics has come along way since the first known conceptual design, which dates back to 1911 [31]. In 1911, the first frequency tuned vibration absorber was proposed in a U.S. patent by Frahm [23]. In the early 1930s the basic principles of operation of order-tuned vibration absorbers were first disclosed in patents [62, 63]. The general idea behind the order-tuned absorbers was that of mounting a mass to a rotating

system such that it is free to oscillate and react in the desired manner to reduce fluctuations in the rotor speed, that is, torsional vibrations. Taylor was the first to realize the importance of the order-tuned device and introduced it into industry [73]. Constructions of order-tuned devices were first carried out by R. Chilton of the Wright Aeronautical Corporation, who used the bifilar design, and E.A. Ryder and G.L. Williams of the Pratt and Whitney Aircraft Company, who used a roller design [27]. The bifilar design (see Fig. 1.1 (c)) is still the typical implementation used in applications today, including light aircraft engines and helicopter rotors.

The mathematical and dynamics modeling of absorber systems began with investigating the absorber system's linear dynamic response, in order to determine how to tune an absorber to be effective at counteracting an order n excitation. The absorber COM paths initially used were circular, with curvature selected to meet the small amplitude (linear) tuning condition [41]. Den Hartog [28] was the first to clearly describe the detuning caused by nonlinear effects that arise at modest amplitudes for these absorbers. In regards to linear theory, Den Hartog [27] investigated how viscous damping and detuning an absorber (the relative tuning between the absorber tuning order and the excitation order) affect the resulting linear steady-state torsional vibration of the rotor. Den Hartog was also the first to account for the nonlinearity in the pendulum free vibration response, showing that the softening restoring force of the circular path resulted in a detuning of the pendulum, which grew with increasing amplitude (i.e. the absorber tuning order decreased with increasing amplitude of oscillation). He suggested overtuning the absorber to account for this effect. Newland [56] (a Den Hartog Ph.D. student), investigated the forced vibration response of circular path absorbers and showed that the softening restoring force can result in the devastating non-

linear jump bifurcation described above. To avoid this jump, Newland [56], quantified the required level of over-tuning for circular path absorbers. He provided guidelines for robust tuning to avoid the jump bifurcation, while maintaining absorber effectiveness in terms of reducing torsional vibrations. These types of results, which were originally carried out using harmonic balance methods [56], were recently extended using perturbation calculations to consider a more general family of paths, and to determine the dynamic stability of single and multi-absorber systems [5, 68].

Due to the potentially disastrous non-linear jump response associated with the circular path, another phase of research has involved the study of non-circular paths that can avoid the jump. These studies also consider the effects of the path on absorber effectiveness at reducing order n vibrations, while avoiding amplification of higher harmonic vibrations, i.e., $2n, 3n....$ It turns out that for an over-tuned absorber, the jump bifurcation is only possible for softening paths, and this is why non-circular paths that are either tautochronic or hardening are advantageous [5, 68]. These paths, when over-tuned, have only one possible steady-state amplitude response (for a system with a single absorber), which is the desired response that is out of phase with the excitation. Madden [38] was the first to suggest a non-circular path that was capable of overcoming the jump response, specifically by using a cycloid, which is the solution of the classical brachistochrone problem, and the less well-known tautochrone problem.[2] The cycloidal path suggested by Madden produces a slightly hardening response. The brachristochrone/tautochrone epicycloidal path for a centrifugal

[2]The brachistochrone is the solution to the problem posed in June 1696 by Johann Bernouilli: "Given two points A and B in a vertical plane, find the curve that a point M, moving on a path AMB must follow such that, starting from A, reaches B in the shortest time under its own gravity." It turns out that the cycloid actually solves both the minimum time (brachristochrone) and the equal time independent of starting amplitudes (tautochrone) problem for a gravitational field.

field was known to Huygens, but brought to use in absorbers by Denman [16]. Denman's work simplified the study of absorber paths, since it provides a general framework in which the equations of motion can be developed for a two-parameter family of paths. The parameter $\tilde{n}$ sets the linear tuning, while the parameter λ allows one to vary paths from circular (strongly softening), to tautochronic (neutral), to cycloidal (hardening) [17]. This formulation provided a means by which perturbation studies can be performed to systematically investigate the effects that path parameters have on the system response. A study by Lee & Shaw [33] showed that, although the epicycloidal path results in a favorable simple harmonic absorber response (for constant rotor speed), the torque that the absorber puts back on the rotor is not a pure harmonic of order n, due to the nonlinear kinematic coupling of the absorber to the rotor. This implies that the tautochronic epicycloid, while avoiding detuning, is not able to exactly counteract a purely harmonic torque, as is desired. A solution to this problem was a subharmonic absorber system, which consists of a pair of identical absorbers riding on epicycloidal paths tuned to one half the order of the excitation torque. These generated, via a subharmonic response, a torque that is exactly a pure harmonic over a wide range of amplitudes [34, 35]. Further analyses by Chao & Shaw [12, 13] incorporated path imperfections in the analysis and determined design guidelines for systems of identical, multiple, subharmonic absorber pairs.

The subharmonic absorber system is actually one of a number of non-synchronous steady-state responses that can result from symmetry-breaking bifurcations inherent in systems with multiple identical absorbers. Except for the subharmonic absorber, non-synchronous responses are not desired in practice, since the absorbers do not function in an optimal manner with minimal amplitudes. This observation has motivated several investigations

into determining system parameter conditions that result in non-synchronous responses, so that absorbers can be designed to operate synchronously in the steady-state. In fact, multiple absorber systems are typically required in applications, in order to balance the rotating system, by placing sets of absorbers symmetrically about the rotor center. Chao & Shaw [11] and Shaw & Geist [68] showed that for tautochronic and nearly-tautochronic path absorbers, a critical excitation torque magnitude exists which, if exceeded, results in loss of stability of the synchronous response, resulting in nonsynchronous absorber responses. This bifurcation can be avoided by sufficient levels of absorber damping and/or intentional absorber mistuning, both of which degrade absorber performance in terms of reducing rotor torsional vibrations. In a related study, Chao & Shaw [14] found that the post-bifurcation dynamics are dominated by a stable steady-state solution branch in which one absorber undergoes a much larger amplitude of motion relative to the others, essentially a form of nonlinear localized response. A similar study by Alsuwaiyan and Shaw showed that for hardening and softening paths (i.e., paths that are not nearly tautochronic), the bifurcation to a non-synchronous response can be avoided for softening paths if the absorber is designed with an over-tuning level that is greater than or equal to a value set by the viscous damping coefficient and the excitation order n [4, 5]. It was also found that for sufficiently over-tuned neutral (tautochronic) and hardening paths, the non-synchronous response is not possible, nor is the jump, and these properties make epicycloidal and cycloidal paths quite appealing. To extend these results to nearly tautochronic paths, a recent study by Shaw & Geist [68] describes analytical results for the stability of the synchronous absorber response against both jump and symmetry-breaking bifurcations, in terms of the two path parameters. The mathematical tools needed to investigate the stability of the synchronous response in multiple

absorber systems include circulant matrices, which are thoroughly covered in [57].

To validate the steady-state response analytical results, a number of experiments were performed using both single and multiple absorber systems. These were carried out using an experimental rig described in detail in [26] and Chapter 5 of this dissertation. This apparatus allows one to input a specified excitation torque signal (in terms of order and amplitude), and measure the resulting response of the rotor and up to four attached absorbers. The torque signal is specified in LabVIEW and then sent to a servo motor which excites the rotor and the attached absorbers. The responses of the rotor and absorbers are recorded in LabVIEW for post-processing the data. The steady-state experiments performed to date have included excitation order sweeps (at constant excitation amplitude) and excitation amplitude sweeps (at constant excitation order). These results show excellent agreement with theoretical predictions for circular path pendulum-type absorbers [26, 52–54], as well as for tautochronic path absorbers [65, 70]. As expected, non-synchronous motions were observed in the multiple absorber experiments for cases when the absorbers tuning order was near the excitation order (i.e. $\tilde{n} \approx n$) [52–54]. However, the non-synchronous motions observed in the experiments involving four absorbers did not agree in form with the previous analytical predictions. In particular, Nester et al. [52–54] found that for low torque levels, a subset of the four absorbers were essentially inactive (almost zero amplitude), and that as the excitation amplitude was increased, more absorbers became active, and eventually synchronous with the active set of absorbers, one at a time, until all four were active. These results deserve further investigation, and some suggestions based on recent observations during the course of this work are given in Chapter 6. More recently, Vidmar [75] performed an analytical and experimental study accounting for both Coulomb and viscous damping

using the same circular path pendulum-type absorber as described in Nester [53, 54]. The Coulomb friction was adjusted by tightening the screw on the bearing about which the absorber swings, and it was found that the Coulomb friction resulted in a sticking (zero rotational velocity relative to the rotor) of the absorber up to a certain level of torque. As expected, this resulted in no reduction in torsional vibration, until the absorbers broke free and began to move [75].

As discussed in Section 1.1, these absorbers have been proposed to expand the operating envelope for cylinder deactivation in variable displacement engines, which offers improved fuel economy by reductions in pumping losses. In these engines, cylinders are deactivated depending on the loading conditions. This is accomplished by closing the intake and exhaust valves and stopping fuel transmission to the deactivated cylinders. Currently, these engines are required to operate in full cylinder mode in the low-RPM range due to vibration issues associated with the reduced cylinder mode at low speeds. Therefore, vibration absorbers tuned to the reduced cylinder mode excitation order have the potential to allow such engines to run at lower speeds, and higher loads, in reduced cylinder mode. In fact, if idle can be reached within allowable vibration limits, significant improvements in mileage will be realized for the standard driving cycle that is used to establish official vehicle mileage. It was shown in an experimental study on a prototype Ford V8/V4 engine that these absorbers allowed one to operate at much lower engine speeds, thereby expanding the operating range for reduced cylinder operation, and improving fuel savings [55]; this is the only known experimental study of absorbers on a variable displacement automotive engine. Another experimental study by Albright et al. [3] using a roller type absorber, showed the absorber to work well when the excitation exists at integer orders of crankshaft rotation, without the added amplification of

a torsional resonance which occurred in their high power V8 drag motors.

While known to be effective for steady-state operation, the transient behavior of absorbers is a looming question when considering them for automotive implementations. A transient event that is especially important in engines that employ cylinder deactivation is that of the deactivation event, in which the fluctuating torques on the crankshaft change quite suddenly in terms of the order and amplitude. In general, the engine order is reduced (typically by a factor of 1/2, when half the cylinders are deactivated) and the amplitude is increased by a factor of about 2-3 (due to fewer harmonic cancellations). If the absorbers are tuned for the reduced-cylinder mode of operation, this abrupt change corresponds to a transition from non-resonant to near-resonant excitation for the absorber response, the effects of which are amplified by the increase in excitation level. This leads to a beating-type transient motion, resulting in overshoot of the absorber response before it reaches steady state conditions [58, 69]. An experimental and theoretical transient investigation by Palmer for softening paths showed that simulations of the averaged equations provided a satisfactory prediction of the experimental results for circular path absorbers [59]. Palmer suggested that the averaged equations provide an efficient way to determine the bounds on the overshoot, the beating frequencies, and the decay rates. A subsequent study investigated the transient response of exactly tautochronic paths, and scaled the amplitudes so that a closed form solution of the envelope of the transient response could be obtained [53, 54]. This linear analysis provided explicit formulae for many important quantities, including peak amplitude, steady-state amplitude, settling time, and beat period. This thesis extends and amplifies these previous studies.

1.4 Summary of Results

The main contributions of this work include the following: We have provided a model of the absorber that includes the dynamics of the support rollers used in bifilar suspensions, and derived, for the first time, a tautochronic path for this case. In terms of problem formulation, we combined the two types of path scalings introduced by Shaw et al. [5,11,14,26,52,53,68,70] into a single framework from which an approximate analytical method for the transient overshoot of a CPVA system can be obtained. In addition, a unique rescaling of the averaged equations was introduced that combines the order detuning, the amplitude of excitation, and the system nonlinearity, into a single parameter, χ. The analytical predictions are based on the method of averaging, and for an undamped system the prediction of overshoot involves solving the roots of a pseudo-energy equation. When the dominant nonlinearity arises from the path, the undamped overshoot result is obtained in closed form, as the roots of a quartic polynomial that depend solely on χ. This result follows from an analysis of the transient response of a standard Duffing oscillator with suddenly applied near-resonant harmonic excitation, a treatment that is, to the author's knowledge, original. For paths that are nearly tautochronic, an additional parameter γ is required, and the overshoot roots must be found numerically. The addition of damping introduces a dissipation parameter D for all paths, and the predictions require simulation of the averaged equations. These analytical predictions are compared against simulations of the original equations of motion, simulations of the averaged equations, and experiments performed using a circular path absorber and a near-tautochronic path absorber. The main results are presented in Fig. 5.6 (a) & (b), which show that the analytical overshoot predictions provide a useful upper bound to the data, thus making it a convenient tool for conservative absorber designs. As expected, the full

equations of motion do the best at predicting the overshoot in general cases, but simulations of the averaged equations are also quite accurate. Lastly, as shown in Fig. 5.7 (a) & (b), more aggressive absorber designs can be obtained if a bound on the absorber damping is known.

Chapter 2

Accounting for Roller Inertia in the Bifilar CPVA System Model

2.1 Introduction

A bifilar suspended CPVA employs a pair of cylindrical rollers which suspend the absorber mass as shown in Fig. 2.1. This arrangement results in the absorber mass translating, but not rotating, relative to the rotor. Other implementations do exist such as a roller type absorber system [30], but the bifilar suspension has been most common in practice. An important aspect of these absorbers is their tuning, which is determined by the path along which their center of mass moves. This tuning, which for these absorbers is order tuning rather than frequency tuning, consists of linear and nonlinear components. The linear part sets the small amplitude vibration characteristics, and has long been understood [28, 31]. The linear tuning order is set to be close to the order of excitation, so that the absorber responds to the excitation in such a manner so as to reduce torsional vibrations of the rotor.

The softening nonlinear aspects of the commonly-used circular path absorbers were known to cause problems, since their frequency of free oscillation decreases as a function of vibration amplitude, thereby resulting in detuning [28,56]. Absorber paths that overcome this problem have been proposed and studied, and include cycloids, epicycloids, and generalizations of these [5,17,38]. Much of this work simply ignored the inertial effects of the rollers. However, Denman [17] included the roller inertia in a study of absorbers with quite general paths, and derived a means of including the effects of roller inertia for the linear tuning. His work included the nonlinear dynamics of the rollers in the equations of motion, but does not provide a systematic investigation of how to design nonlinear aspects of the dynamics to account for rollers. That work also included a thorough description of the zero roller inertia *tautochronic* absorber path, that is, the path that renders the absorber frequency as constant for all physically realizable amplitudes of response, i.e., a path such that the absorber is neither softening nor hardening out to large amplitudes.

Although the roller masses are small in comparison to the absorber mass, it is important to know how the overall system dynamics are affected by the inertia of the rollers. This is obvious for the linear tuning, since a slight off-tuning dramatically affects the system response in terms of absorber effectiveness and operating range [5, 68]. The purpose of the present work is to systematically quantify the effects of rollers on the linear and nonlinear system response, so that one can design absorber systems that fully account for the dynamics of the rollers.

We begin with a derivation and description of the equations of motion in a nondimensional form that is convenient for analysis; this, and many subsequent steps, follow previous work on CPVAs, cf. [11, 68]. The absorber path and the attendant linear and nonlinear tuning

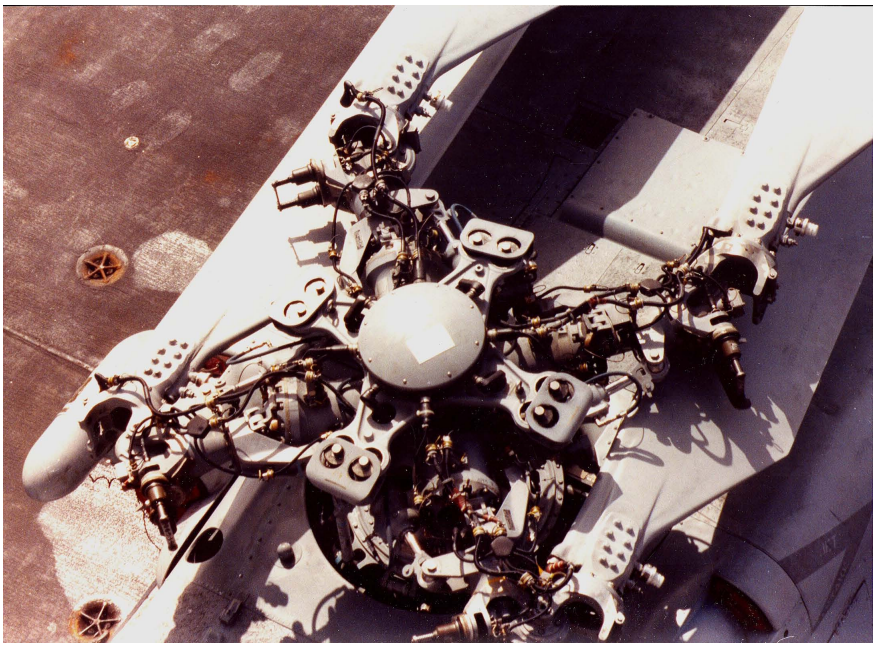

Figure 2.1: Picture taken by Steve Shaw of a helicopter rotor with four bifilar absorbers attached (taken aboard the USS Nimitz).

parameters are then considered, and the tautochronic path that accounts for rollers is derived. This is followed by a perturbation analysis of the system dynamics, and an example is presented that demonstrates the influence of rollers on the system response. It is seen that so long as the rollers are accounted for in the linear tuning, and the nonlinear tuning is close to tautochronic, then the overall system response is largely insensitive to small variations in the nonlinear tuning, which is influenced by the inertia of the rollers. In fact, the rollers are found to provide a slight hardening effect on the absorber response, which actually shifts the system away from potential jumps in the absorber response. This chapter closes with a brief discussion of the results.

2.2 Dynamic Model

In this section the dynamic model for a CPVA suspended in a bifilar configuration by a pair of rollers is constructed. The model is introduced by defining parameters for a single absorber with general inertial properties and a pair of rollers that are assumed to roll without slipping.[1] After these basic features and some nondimensional parameters are introduced, the equations of motion for a system composed of a rotor with N CPVAs riding on rollers are derived by a Lagrangian approach. Here we simply outline the steps of the derivation, since the details are available in previous work [5,17]. The equations of motion are then presented for a single absorber which are non-dimenionalized and re-scaled for the purpose of doing analysis. This includes a perturbation calculation which is used to determine the effects that the rollers have on the system response; these steps also follow previous work [11, 68], but here include the effects of rollers.

The bifilar construction of CPVAs using rollers consists of four essential components: a rotor, an absorber mass, and two rollers, as shown in Fig. 2.2. The rotor is subjected to a fluctuating torque, resulting in torsional vibrations of the rotor. The absorber mass is a generalized centrifugal pendulum and will be referred to herein simply as the *pendulum*. The pendulum is suspended from the rotor by the rollers, which roll along two cutouts in the rotor, as shown in Fig. 2.2. The rollers also roll along identical, inverted cutouts on the pendulum. This arrangement kinematically forces the pendulum center of mass (COM) to follow a path that is dictated by the shape of the cutouts. In many applications, for ease of manufacturing, these cutouts are simply circles. In general, the dynamic model for the bifilar construction is described by the motion of the COM of N identical pendulums, each of mass

[1] We have examined the motions of such rollers in an experimental rig and found that they indeed roll without slipping in all situations observed.

m_P and moment of inertia I_P about the pendulum's COM. These are attached to a rotor which has a moment of inertia I_C about the center of rotation, point 0, as shown in Fig. 2.2. As previously mentioned, it is assumed that the two rollers, each of mass m_R, radius A, and moment of inertia i_R about their COM, roll without slip along the cutouts. Note that in this arrangement the arclength distance S displaced by the COM of the pendulum along its path is twice that moved by the COM of each of the rollers along their respective paths [17]. The positions of both the pendulum and the rollers' COM relative to the rotating coordinate system at point O can be conveniently expressed in terms of a function $R_P(S)$, which is the distance from the center of the rotor O to the pendulum COM at a position corresponding to S. Here all absorber paths are taken to be identical and symmetric about a vertex at $S = 0$ such that $R_P(-S) = R_P(S)$. Here we denote $R(0) = c$, which is the largest value of $R_P(S)$. Under these assumptions the dynamic system consists of $N + 1$ degrees of freedom, corresponding to the positions S_i of the pendulums and the rotor orientation θ. We present a derivation for this system and then specialize to the case $N = 1$ which is sufficient for the present study.

The system kinetic energy is given by

$$T_t = T_C + \sum_{i=1}^{N} (T_{P_i} + T_{R_i}), \tag{2.1}$$

where T_C accounts for the rotational kinetic energy of the rotor, T_{P_i} is the total kinetic energy of the i^{th} pendulum, and T_{R_i} is the total kinetic energy of the the i^{th} pair of rollers. For the pendulum and rollers we compute the kinetic energy using the translation of the

COM and rotation about the COM. The total kinetic energy can then be written as

$$
\begin{aligned}
T &= T_C(\dot{\theta}) + \sum_{i=1}^{N} \Big\{ T_{R_i}(\dot{\theta}, \dot{S}_i, S_i) + T_{P_i}(\dot{\theta}, \dot{S}_i, S_i) \Big\} \qquad (2.2) \\
&= \frac{1}{2}\Bigg(J + \sum_{i=1}^{N} \Bigg(m_P R_P^2(S_i) + 2m_R \Big(H^2 + \\
&+ (c/2 - D)^2 + (c/2 - D) Y_P(S_i) + \frac{1}{4} R_P^2(S_i) \Big) + 2i_R \Bigg) \Bigg) \dot{\theta}^2 \\
&+ \sum_{i=1}^{N} \Bigg((m_P + \frac{1}{2} m_R) G(S_i) + \frac{1}{2} m_R (2D - c) \frac{\partial X_P(S_i)}{\partial S_i} - i_R/A \Bigg) \dot{S}_i \dot{\theta} \\
&+ \sum_{i=1}^{N} \frac{1}{2} \Bigg(m_P + \frac{1}{2} m_R + \frac{1}{2} (i_R/A^2) \Bigg) \dot{S}_i^2,
\end{aligned}
$$

where $J = I_c + N I_P$ is the total inertia of the rotor and the pendulums about their respective COM, A is the roller radius, and D and H are, respectively, the vertical and horizontal distances from the rotor center O to the roller COM when the pendulum is at its vertex; see Fig. 2.2. The terms $X_P(S)$ and $Y_P(S)$ locate the pendulum's COM position relative to the rotor-fixed $X - Y$ coordinate system, and $R_P^2(S) = X_P^2(S) + Y_P^2(S)$ (see [17] or Appendix B for further details). Lastly, $G(S) = \sqrt{R_P^2(S) - \frac{1}{4}(\partial R_P^2(S)/\partial S)^2} = R_P \sqrt{1 - (\partial R_P(S)/\partial S)^2}$, is R_P times the cosine of the angle between the local tangent to the absorber path at S and the normal to the radial line passing through O and the point at S on the path [68]. Therefore, $G(0) = R(0) = c$, and $G(S) = 0$ corresponds to the absorber moving directly towards the rotor center, which gives the maximum achievable value of S, denoted by S_{max}, for many absorber paths. This limit will be investigated further during the perturbation calculations, for which the absorber path and the maximum possible

absorber amplitude will be important.

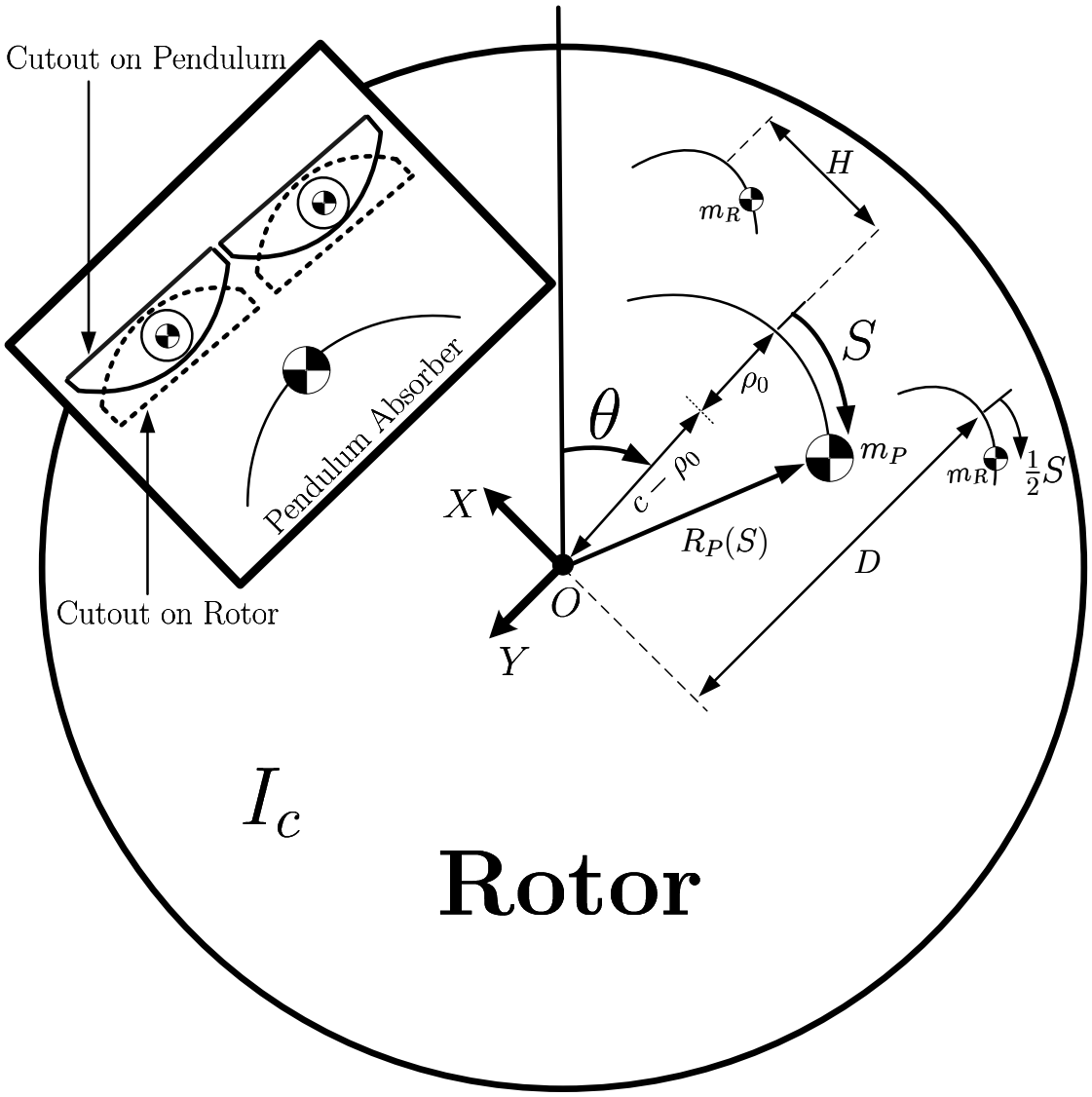

Figure 2.2: Depiction of a bifilar roller-suspended pendulum (left) attached to a rotor, and the paths of the pendulum COM and rollers' COM (right).

Using the kinetic energy in equation (2.2), and generalized forces from dissipation and applied loads, one can derive the equations of motion for the system using the Euler-Lagrange method. These derivations, and subsequent non-dimensionalization and rescaling, with the rollers absent, are described in previous work [11,14]. An important step in the development

of the equations of motion is that the rotor angle θ is used to replace time as the independent variable, which converts nonlinear θ-dependent torques into external excitation terms. The equations of motion are presented by first introducing a number of variables and parameters, after which we present the absorber and rotor equations of motion. These equations are, of course, coupled in the following way: the absorber response is driven by the torsional acceleration of the rotor, and the rotor dynamics are affected by torques produced by the absorbers as they move along their paths. The goal is to design the absorbers such that these torques counteract an applied fluctuating torque that acts on the rotor, that is, the torque that produces the unwanted torsional vibrations.

We first introduce s, g, x_P, y_P, r_P, and a as non-dimensional versions of their corresponding upper case versions given in equation (2.2), in which physical system lengths are normalized by the distance c, ϵ is defined as the absorber to rotor inertia ratio $m_P c^2/J$, and many parameters that are known to be small are scaled by ϵ for convenience. The nondimensional rotor speed is denoted by ν, which is the rotor speed $\dot{\theta}$ normalized by the mean rotor speed Ω; thus torsional vibrations are represented by fluctuations in ν and the desired constant rotor speed operating state is represented by $\nu = 1$. The effects of damping and applied torques are included by their generalized forces, and are specified below. Using these definitions, and following the steps of previous derivations [11, 14], the equation of motion for a single absorber ($N = 1$) is found to be

$$\begin{aligned} & (1+\epsilon\delta+\epsilon\xi)\nu^2 s'' + \Bigg((1+\epsilon\delta+\epsilon\xi)s' + \\ + \quad & (1+\epsilon\delta)g(s) - 2\epsilon\xi a - 2\epsilon\delta\ell \frac{\partial x_P(s)}{\partial s} \Bigg) \nu'\nu + \\ - \quad & \nu^2 \left(\frac{1}{2} \frac{\partial r_P^2(s)}{\partial s} (1+\epsilon\delta) + 2\epsilon\delta\ell \frac{\partial y_P(s)}{\partial s} \right) = -\epsilon\mu s'\nu, \end{aligned} \tag{2.3}$$

where primes indicate derivatives with respect to θ, $\epsilon\mu$ is an effective viscous damping coefficient along the absorber path, and $\epsilon\delta$, $\epsilon\xi$, and ℓ are the non-dimensional terms introduced by the rollers. Table 2.1 provides definitions of these nondimensional roller parameters in terms of physical variables, from which one can see that ℓ is related to the placement of the roller relative to the absorber (see Fig. 2.2), while $\epsilon\delta$ and $\epsilon\xi$ are related to the roller mass and moment of inertia, respectively. Note that these parameters are related to one another in a manner that depends on the details of the roller's inertial properties and placement on the rotor. These three coefficients capture the effects of the rollers, which is the primary subject of this work.[2]

The rotor equation of motion is similarly derived, and is found to be relatively complicated. It is therefore given here in expanded form, which to first order in ϵ is given by,

$$\begin{aligned} \nu\nu' &= \epsilon\Big(\Gamma\sin(n\theta) + \Gamma_0 - \mu_0\nu\Big) - \epsilon\Bigg(\nu\nu' r_P^2(s) + \\ &+ \nu\nu' g(s)s' + \nu^2\frac{\partial r_P^2(s)}{\partial s}s' + \nu^2\frac{\partial g(s)}{\partial s}s'^2 + \nu^2 g(s)s''\Bigg) + \mathcal{O}(\epsilon^2), \end{aligned} \tag{2.4}$$

where $\nu\nu'$ is the rotor angular acceleration (the normalized value of $\ddot{\theta}$ with θ as the independent variable, specifically, $\nu\nu' = \ddot{\theta}/\Omega^2$ [11]), $\Gamma\sin(n\theta)$ is the order n component of the fluctuating torque (the source of the rotor torsional vibrations), Γ_0 is the mean torque acting on the rotor, $\mu_0\nu$ is the equivalent viscous rotor bearing resistance torque, and the remaining terms are the torque on the rotor resulting from the motion of the absorber (as can be seen since they are proportional to the nondimensional absorber inertia, ϵ). Details

[2]Note that many designs require that $\ell > -0.5$, which according to Fig. 2.2 means that the roller COM is closer to the rotor center then the pendulum COM. The situation of $\ell < -0.5$, which is the configuration shown in Fig. 2.2, is avoided because it can cause out-of-plane instabilities in the absorber motion unless the absorber motion is restricted.

of this derivation and the relationships between physical system parameters and the non-dimensional quantities (other than those associated with the rollers) can be found in [11,14], and the full equation is given in Appendix A. It is worth noting that the effects of the rollers do not appear explicitly at this order, since they are order ϵ compared to the absorber inertia, and therefore appear at order ϵ^2 in $\nu\nu'$. However, the rollers have a significant affect on the absorber response s, since the system is acting near resonance and the rollers affect the linear tuning. Finally, it should be noted that the assumptions that the nondimensional

Table 2.1: Relationship between the non-dimensional roller and physical system parameters.

$\epsilon\delta$	$\epsilon\xi$	ℓ
$\frac{1}{2}(m_R/m_P)$	$\frac{1}{2}\left\{i_R/(m_P A^2)\right\}$	$\frac{1}{2} - D/c$

damping parameters, torques, and absorber to rotor and roller to absorber inertia ratios, are small, and thus scaled by ϵ, are consistent with parameter ranges found in most applications.

2.2.1 Formulation of the Absorber Path

In order to completely specify the equations of motion, the path of the absorber COM must be prescribed. In practical implementations this path is dictated by the shape of the cutouts shown in Fig. 2.2, which are designed to achieve desired absorber performance. After an absorber path is specified, equations (2.3) and (2.4) can then be solved (by numerical or perturbation methods) for the response of the absorber and rotor. As one might expect, the shape of the path plays an important role in the system response and the effectiveness of the absorber in attenuating the rotor torsional vibrations, and several studies have considered these effects [5, 68]. As in previous work, we specify these paths using the two-parameter family of curves introduced by Denman [17]. This class of paths is uniquely determined

by linear and nonlinear tuning parameters, as follows: we denote $\tilde{n}$ as the linear absorber tuning order and λ as the nonlinear tuning parameter. The linearized absorber frequency of oscillation for constant rotor speed Ω is given by $\tilde{n}\Omega$ in the dimensional case, or simply by the order $\tilde{n}$ in the nondimensional case. The nonlinear tuning parameter controls the frequency-amplitude dependence of the absorber's vibration response, that is, its hardening or softening effects. Both of these path parameters can be introduced into the equations of motion through the pendulum's position $r_P(s)$, as is now described. It should be noted that in the following $\tilde{n}$ is the tuning order and that $\tilde{n}_0$ is the tuning order for the special case of zero roller inertia, and it has a special geometric interpretation, described subsequently.

In order to specify the equations of motion in terms of the parameters $\tilde{n}$ (or $\tilde{n}_0$) and λ, we need to formulate the pendulum position function $r_P(s)$ as a function of these parameters. Denman [17] provides a detailed development of this formulation, the highlights of which are presented here and in Appendix B. This path formulation is valid for a family of epicycloidal paths described by nonlinear tuning values in the range $0 \leq \lambda < 1$, with limiting cases of circles ($\lambda = 0$) and cycloids ($\lambda = 1$) [17, 24].

We first consider the linear tuning problem. The linear tuning order without rollers $\tilde{n}_0$ is well known [17] and is dictated by the ratio of the distance from the effective pendulum pivot point to the rotor center, $c - \rho_0$, to the effective pendulum length, ρ_0, specifically,

$$\tilde{n}_0 = \sqrt{\frac{c - \rho_0}{\rho_0}} = \sqrt{\frac{c}{\rho_0} - 1}. \tag{2.5}$$

We will use $\tilde{n}_0$ throughout the rest of this chapter as a convenience instead of using its full expression which is related to the path curvature ρ_0 as well as the distance c as shown in equation (5); however, it is important to note that only when considering the zero roller

inertia case does $\tilde{n}_0$ correspond to the linear tuning parameter $\tilde{n}$.

In order to consider the entire path, including nonlinear effects, one utilizes the non-dimensional version of the general path expressions provided in Appendix B, specifically,

$$r_P^2(s) = 1 + \left(\frac{\lambda^2}{\lambda^2 - 1}\right)s^2 + 2\left(\frac{\lambda^2 - \lambda_{e0}^2}{(\lambda^2 - 1)^2}\right)\left(1 - \lambda_{e0}^2 - \frac{\partial x_P}{\partial s}\sqrt{(1 - \lambda_{e0}^2)^2 - s^2\lambda^2} - s\lambda^2\frac{\partial y_P}{\partial s}\right) \quad (2.6)$$

where

$$\frac{\partial y_P}{\partial s} = \sin\left(\frac{1}{\lambda}\sin^{-1}\Big(\lambda(\tilde{n}_0^2 + 1)s\Big)\right),$$

$$\frac{\partial x_P}{\partial s} = \cos\left(\frac{1}{\lambda}\sin^{-1}\Big(\lambda(\tilde{n}_0^2 + 1)s\Big)\right),$$

$$\lambda_{e0} = \tilde{n}_0/\sqrt{\tilde{n}_0^2 + 1}. \quad (2.7)$$

Note that λ_{e0} is a special zero-roller nonlinear tuning parameter described below. The reader is reminded that $\tilde{n}_0$ is a tuning parameter only for zero roller inertia, that is, for $\epsilon = 0$.

It is important to account for the rollers when selecting the tuning parameters $\tilde{n}$ and λ, because improper path selection can lead to poor performance, and even instabilities in the desired response [5]. To avoid these undesirable effects, one typically takes $\tilde{n}$ to be slightly larger than n (i.e., the absorber is slightly over-tuned linearly), and the nonlinear tuning parameter is selected so that the path is neutral, $\lambda = \lambda_e$, or slightly stiffening, that is, $\lambda_e < \lambda \leq 1$, where λ_e is defined below [5, 56, 68].

2.3 The Tautochronic Path with Rollers

It is known that if roller inertia is neglected the pendulum can be modeled as an equivalent point mass, with its moment of inertia about its COM included with that of the rotor, since

in a bifilar suspension the absorber rotates identically with the rotor [17]. In that case there is a special absorber path for which the absorber behaves like a linear oscillator, even for large amplitude motions. This *tautochronic*, or equal time, path is known to be a particular epicycloid [17], and it renders the absorber to have the same frequency, or, more precisely, the same order, out to large amplitudes. The absorber amplitude in this case is limited by the cusp on the epicycloidal path, which occurs at $s = s_{max}$, at which $g(s_{max}) = 0$. A previously unanswered question is whether or not such a tautochronic path exists when roller inertia is accounted for in the model. In this section we show that such a path indeed exists, and we derive its form.

To consider this problem, we take the absorber equation of motion (2.3) with zero damping ($\mu = 0$) and a constant rotor speed ($\nu = 1$, $\nu' = 0$), yielding

$$(1 + \epsilon\delta + \epsilon\xi)s'' - \frac{1}{2}\frac{\partial r_P^2(s)}{\partial s}(1 + \epsilon\delta) - 2\epsilon\delta\ell\frac{\partial y_P(s)}{\partial s} = 0, \tag{2.8}$$

where $\partial r_P^2/\partial s$ is given by

$$\frac{\partial r_P^2}{\partial s} = 2\left(\frac{\lambda^2}{\lambda^2 - 1}\right)s + 2\left(\frac{\lambda_{e0}^2 - \lambda^2}{\lambda^2 - 1}\right)\frac{\partial y_P}{\partial s}. \tag{2.9}$$

The goal here is to show that there exists a nonlinear tuning parameter $\lambda = \lambda_e$ that renders this as a linear oscillator with a fixed order $\tilde{n}$ for all amplitudes. It will be shown that this special path is described by an epicycloid in the two parameter family developed above.

Before turning to the general case, we first consider the roller-free tautochrone, for which $\delta = \xi = 0$ in equation (2.8). In this case it is not difficult to show that the choice of $\lambda = \lambda_{e0} = \tilde{n}_0/\sqrt{\tilde{n}_0^2 + 1}$ renders equation (2.9) as $\partial r_P^2/\partial s = -2\tilde{n}_0^2 s$, resulting in the linear oscillator

$s'' + \tilde{n}_0^2 s = 0$ for equation (2.8). The attendant path function is $r_{P0}(s) = \sqrt{1 - \tilde{n}_0^2 s^2}$, corresponding to the roller-free tautochronic epicycloid of order $\tilde{n}_0$.

For the development that includes roller inertia it is convenient to express the equation of motion (2.8) in a Taylor series in s. Using the given expressions for $\partial y_P/\partial s$ and $\partial r_P^2/\partial s$, expanding in s, and recognizing a pattern in the series, the equation of motion can be written as

$$s'' + \tilde{n}^2 s + \left(\frac{\chi}{1+\epsilon\delta+\epsilon\xi}\right) \sum_{k=1}^{\infty} \left(\frac{\left((\tilde{n}_0^2+1)s\right)^{2k+1}}{(2k+1)!} \prod_{i=1}^{k} \left((2i+1)^2\lambda^2 - 1 \right) \right) = 0, \quad (2.10)$$

where $\chi = (1+\epsilon\delta)(\lambda^2 - \lambda_{e0}^2) - 2\epsilon\delta\ell(\lambda^2 - 1)$. It is immediately seen that a (linear) tautochronic absorber of order $\tilde{n}$ is recovered for $\chi = 0$.[3] This condition results in the following simple expression for the tautochronic value of λ,

$$\lambda_e = \sqrt{\frac{\tilde{n}^2(1+\epsilon\alpha)}{1+\tilde{n}^2(1+\epsilon\alpha)}}, \quad (2.11)$$

where $\alpha = \xi/(1+\epsilon\delta)$ contains the effects from the rollers. Selection of this value for λ yields the linear oscillator $s'' + \tilde{n}^2 s = 0$, as desired. Note that although we have retained the (typically small) parameter ϵ in this analysis, the results are exact and do not depend on small roller inertia, or any other small parameters. The (small) correction in the nonlinear

[3] One can also obtain the tautochrone condition by substituting equation (2.9) into equation (2.8) and realizing that tautochronic motion implies that terms proportional to $\partial y_P/\partial s$ must vanish. The present approach, however, is cleaner in terms of keeping conditions on the tuning parameters separate.

tuning parameter due to roller inertia can be approximated by expanding in ϵ, which yields,

$$\lambda_e^2 = \lambda_{e0}^2 - \epsilon\left(\frac{2\ell\delta}{1+\tilde{n}_0^2}\right) + \mathcal{O}(\epsilon^2), \tag{2.12}$$

showing that λ_e may be larger or smaller than λ_{e0}, depending on the sign of ℓ, since $\epsilon,\ \delta > 0$.

The linear tuning order $\tilde{n}$ falls out directly from the coefficient of s in the expansion and can be expressed in terms of $\tilde{n}_0$, which dictates the vertex curvature of the path (and the roller-free linear tuning) and the roller parameters, as follows,

$$\tilde{n}^2 = \frac{\tilde{n}_0^2(1+\epsilon\delta(1-2\ell)) - 2\epsilon\ell\delta}{1+\epsilon\delta+\epsilon\xi}. \tag{2.13}$$

This expression, which is a nondimensional form of the linear tuning equation derived by Denman [17], directly shows the influence of the rollers on the linear tuning parameter. To achieve good absorber performance, $\tilde{n}$ and $\tilde{n}_0$ will differ by at most a few percent, but this difference is important since the system operates near resonance.

For absorber path design one chooses a value of $\tilde{n}$ that gives the desired system response from the coupled rotor/absorber equations of motion, and the corresponding path is determined by the following steps. First, solve equation (2.13) for $\tilde{n}_0$ in terms of $\tilde{n}$ and the roller parameters, yielding a special value denoted as $\tilde{n}_{0e}$, which fixes the path vertex curvature by equation (2.5). The absorber path is then generated by utilizing $\tilde{n}_0 = \tilde{n}_{0e}$ and $\lambda = \lambda_e$ in equations (B.4) and (B.5) in Appendix B, and scaling up $(x_P(s), y_P(s))$ and s by the factor c to obtain $(X_P(S), Y_P(S))$, and taking $-S_{max} < S < S_{max}$. From this one can generate the cutouts for the rollers shown in Fig. 2.2, which are given by $\frac{1}{2}(X_P(S), Y_P(S))$ and placed

at coordinates given by D and H as shown in Fig. 2.2.[4] We now turn to examples.

In the following comparisons of paths we assume that the distance c is fixed, which is typically the case, since a designer wants to maximize the absorber moment arm within the allowable space. In designing a vibration absorber for a given application one must satisfy constraints on absorber mass, absorber amplitude, and the absorber placement, all of which are limited in some manner by c. Within these constraints one chooses an absorber path that will give good performance and will avoid instabilities throughout the torque range of interest. Typically, the required path is linearly overtuned and nonlinearly tuned between an epicycloid and a cycloid, that is, is neutral or hardening (i.e. $\tilde{n} \geq n$ and $\lambda_e \leq \lambda \leq 1$) [68].

Shown in Fig. 2.3 (a) are cycloidal, circular, and three epicycloidal paths, all with the same linear tuning $\tilde{n}$. The epicycloidal paths are tautochronic paths for three values of the roller inertia, corresponding to $\delta = 0$, $1/4$, and $1/2$. The cycloidal and circular paths have $\delta = 0$ and are shown to convey the boundaries of typical paths between the circular and cycloidal paths. To generate the tautochronic paths, which are seen to be nearly identical, we fix the linear tuning $\tilde{n}$, and choose δ and ξ, and then solve equation (2.11) for λ_e. We also use the assumption of a solid roller which implies that $\delta = 2\xi$ for the tautochronic paths. Note that while the three tautochronic paths appear to be nearly identical, they have slightly different vertex curvatures, as required to have the same $\tilde{n}$ for different roller inertias.

Figure 2.3 (b) depicts how the path vertex curvature depends on $\tilde{n}$ for three values of the roller inertia, with tuning near 1.5. Note that in order to achieve a specific linear tuning the path curvature increases as the roller inertia increases, assuming all other parameters are

[4]Note that achieving a specific geometry that provides the desired value of tuning is a complicated iterative process since the shape of the cutouts, their placement, the location of the absorber COM, the roller paths, and the tuning parameters are all interdependent. This process can be automated in a computer program [24].

fixed. Note that the roller inertia also affects the value of the nonlinear tuning coefficient λ_e, as seen from equation (2.12), and that it may increase or decrease, depending on the sign of ℓ.

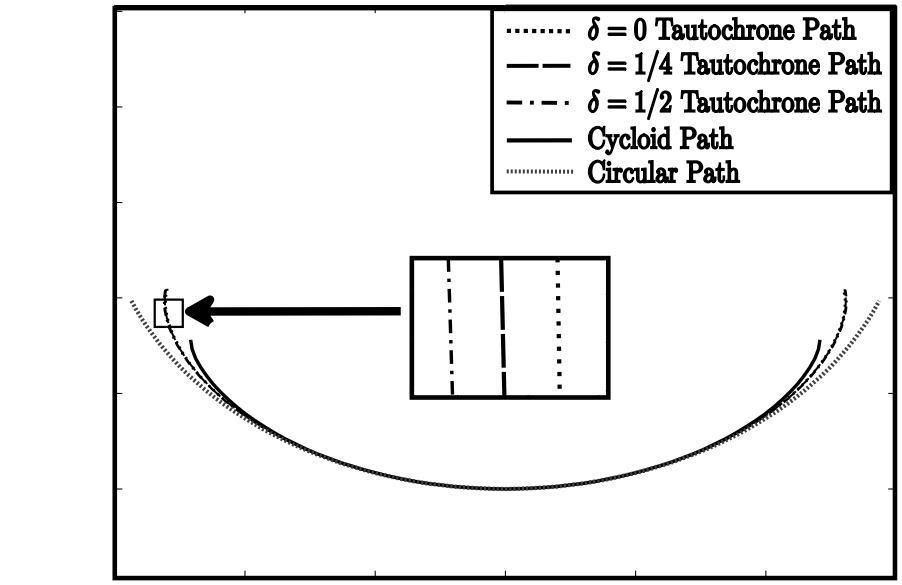

(a)

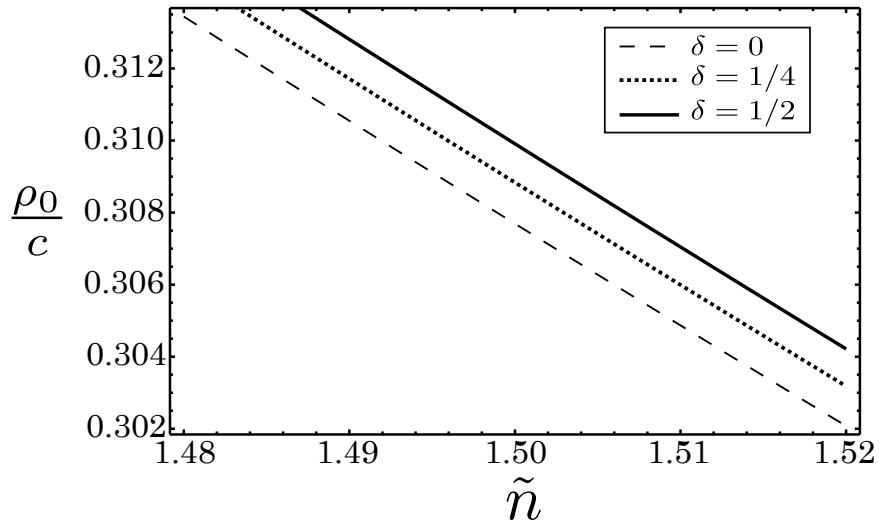

(b)

Figure 2.3: Influence of roller inertia on the absorber COM path, for $\epsilon = 0.10$ and $\ell = -0.25$. (a) Five sample paths: a circle, a cycloid, and three epicycloids, for $\tilde{n} = 1.5$. (b) Vertex curvature vs. $\tilde{n}$ for three values of roller mass.

2.4 Perturbation Analysis

Here we consider the dynamic response of the system, paying special attention to the effects of the rollers. We take a perturbation approach similar to previous work [5, 11, 70], here incorporating the effects of the relatively small rollers by inclusion of the terms involving $\epsilon\delta$, $\epsilon\xi$, and ℓ. The perturbation analysis will make use of a base system that has the tautochronic path without rollers, represented by parameters $\tilde{n}_0$ and λ_{e0}. It is noted that in light of the existence of a tautochronic path with rollers, a perturbation could be performed about that path instead of the roller-free tautochronic path. This was investigated and it was found that the formulation is significantly more complicated than the perturbation approach presented here. One minor complication with the present approach is that one has to transform results obtained for the values of $\tilde{n}_0$ and λ_{e0} into values of $\tilde{n}$ and λ_e, using equations (2.13) and (2.11), in order to obtain the desired path.

To obtain the equations in a form suitable for perturbation calculations, further expansions on equations (2.3) and (2.4) are carried out such that we obtain an oscillator equation that governs the absorber dynamics, with the rotor coupling and roller corrections appearing at order ϵ, along with the damping. This is possible due to the small inertia ratio, which represents the rotor-absorber coupling, as described in [11, 68, 70]. To begin, we note from equation (2.4) that the torques acting on the rotor are all of order ϵ, which results in the rotor speed being nearly unity. It is then reasonable to assume the form $\nu = 1 + \epsilon w + \mathcal{O}(\epsilon^2)$, where w captures the torsional fluctuations of the rotor. If we use this assumption, and the fact that steady rotor oscillations require a balance of mean torque and rotor bearing resistance, stated as $\Gamma_0 - \mu_0\nu = \mathcal{O}(\epsilon)$, we can use equation (2.4) to express the rotor acceleration

$\nu\nu' = \epsilon w' + \mathcal{O}(\epsilon^2)$, where

$$w' = \Gamma \sin(n\theta) - \frac{\partial r_P^2(s)}{\partial s} s' - \frac{\partial g(s)}{\partial s} s'^2 - g(s) s''. \tag{2.14}$$

We next expand the absorber equation of motion (2.3) about $\epsilon = 0$ and substitute the expansion $\nu = 1 + \epsilon w + \mathcal{O}(\epsilon^2)$, and keep only order ϵ terms, one obtains

$$s'' - \frac{1}{2}\frac{\partial r_P^2(s)}{\partial s} = \epsilon\left(2\delta\ell \frac{\partial y_P(s)}{\partial s} - \frac{\xi}{2}\frac{\partial r_P^2(s)}{\partial s} - \mu s' - (s' + g(s))w'\right) + \mathcal{O}(\epsilon^2). \tag{2.15}$$

Equation (2.14) can then be substituted into equation (2.15), which uncouples the absorber equation of motion from the rotor equation of motion. Note that this uncoupling process results in an oscillator equation that governs the absorber dynamics, and it includes the excitation acting on the absorber through the rotor acceleration, which is expressed to leading order in terms of the applied torque and the absorber dynamics. To get the desired form of the absorber equation, we introduce a nonlinear detuning parameter κ, substitute $\lambda = \lambda_{e0} + \epsilon\kappa$ into the absorber path derivatives ($\partial y_P/\partial s$ and $\partial r_P^2/\partial s$) in equation (2.15), and expand about $\epsilon = 0$. This results in an oscillator that is weakly nonlinear, with weak forcing, and weak damping, expressed in the form

$$s'' + \tilde{n}_0^2 s = \epsilon f(s, s', \theta) + \mathcal{O}(\epsilon^2), \tag{2.16}$$

where

$$f(s,s',\theta) = -\mu s' + 2\delta\ell \frac{\partial y_P}{\partial s}|_{\lambda_{e0}} + \xi\tilde{n}_0^2 + \tag{2.17}$$
$$-2\kappa\tilde{n}_0\sqrt{1+\tilde{n}_0^2}\left((1+\tilde{n}_0^2)s - \frac{\partial y_P}{\partial s}|_{\lambda_{e0}}\right) +$$
$$-[s' + g_0(s)]\left(\Gamma\sin(n\theta) + 2\tilde{n}_0^2 s' s - \frac{\partial g_0(s)}{\partial s}s'^2 + g_0(s)\tilde{n}_0^2 s\right),$$

and $(\partial y_P/\partial s)|_{\lambda_{e0}}$ is the path derivative $(\partial y_P/\partial s)$ evaluated at $\lambda = \lambda_{e0}$. Also, the term $g_0(s) = \sqrt{1-\tilde{n}_0^2(1+\tilde{n}_0^2)s^2}$ is the leading order part of $g(s)$, that is, its $\epsilon = 0$ version, or, equivalently, its roller-free tautochronic version. In addition, to obtain equation (2.17), $-\tilde{n}_0^2 s$ is substituted for s'' in equation (2.14), which is valid to leading order in ϵ, as can be seen from equation (2.16). Note that the substitution of $\lambda = \lambda_{e0} + \epsilon\kappa$ gives the desired form for equation (2.16), amenable to the method of averaging. It introduces a parameter κ in the order ϵ terms which controls the variation of the nonlinear tuning parameter λ from the roller-free case. Specifically, when accounting for rollers in the averaged equations one must select $\kappa = (\lambda - \lambda_{e0})/\epsilon$ for the desired value of λ and λ_{e0} (that is, $\tilde{n}_0$). This, along with $\tilde{n}$, allows one to investigate a two-parameter family of absorber paths near the perfectly tuned tautochronic path, with one parameter each for linear and nonlinear tuning. See [68] for a similar formulation of multi-absorber systems without rollers.

Finally, it is important to note that these equations of motion, while weakly nonlinear, are not restricted to small amplitudes, that is, no amplitude expansions have been carried out. This is a consequence of the tautochronic nature of the unperturbed absorber path, and it results in equations that are valid for all physically realizable amplitudes, that is, up to limits imposed by motion-limiting snubbers, or at most, the cusps on the epicycloidal

absorber path.

2.4.1 Application of the Method of Averaging

To obtain approximate solutions to the equations of motion, we apply the method of averaging. The absorber response is expressed in terms of polar coordinates of the form

$$\begin{aligned} s(\theta) &= Z(\theta)\cos\big(n\theta+\psi(\theta)\big) \\ s'(\theta) &= -nZ(\theta)\sin\big(n\theta+\psi(\theta)\big), \end{aligned} \tag{2.18}$$

where $Z(\theta)$ and $\psi(\theta)$ are the absorber amplitude and phase, which will, under conditions of practical operation, be slowly varying functions of the rotor angle θ . This coordinate transformation imposes a constraint on $Z'(\theta)$ and $\psi'(\theta)$, as follows

$$Z'(\theta)\cos\big(n\theta+\psi(\theta)\big)-\psi'(\theta)Z(\theta)\sin\big(n\theta+\psi(\theta)\big)=0. \tag{2.19}$$

Substitution of the transformation in equation (2.18) into equation (2.16) results in an equation with only first order derivatives of $Z(\theta)$ and $\psi(\theta)$. This result and equation (2.19) are linear in $Z'(\theta)$ and $\psi'(\theta)$ and are easily solved for $(Z'(\theta),\psi'(\theta))$. The resulting equations each have terms of order ϵ and a term with the factor $(n^2-\tilde{n}_0^2)$. This term results from the fact that the solution to equation (2.16) with $\epsilon=0$ is simply the linear solution with frequency (order) $\tilde{n}_0$, whereas the coordinate transformation assumes a frequency (order) of n. The presence of the $\epsilon << 1$ terms results in slowly varying amplitudes and phases, except for the fast phase drift due to the difference between n and $\tilde{n}_0$. Since absorbers are effective only when tuned near the excitation order, the difference between n and $\tilde{n}_0$ is small, and so

we define an excitation order detuning parameter Δ via

$$\epsilon\Delta = n^2 - \tilde{n_0}^2. \tag{2.20}$$

With this assumption, the equations for $Z'(\theta)$ and $\psi'(\theta)$ become slowly varying, that is, all terms are $\mathcal{O}(\epsilon)$, and can thus be averaged in θ over one period, $2\pi/n$. This results in autonomous equations for the average values of Z and ψ, which are denoted as z and ϕ. The averaging in this problem is non-trivial due to the nature of terms like $\partial y_P/\partial s$ and $g_0(s)$. Exact analytical expressions for the averages of these terms is not available, and so some terms will be left in the form of integrals that are computed numerically. Approximate solutions to these integrals can be computed using amplitude expansions in z, although we do not pursue that here.

The results for the averaged equations for z and ϕ are given by

$$z' = \frac{\epsilon}{n}\left(\frac{-\mu z n}{2} + \Gamma\cos(\phi)F_1(z)\right) + \mathcal{O}(\epsilon^2) \tag{2.21}$$

$$\begin{aligned}\phi' = &\frac{\epsilon}{zn}\left(-2M(z)\left(\kappa\tilde{n}_0\sqrt{1+\tilde{n}_0^2} + \delta\ell\right) - \Gamma\sin(\phi)F_2(z) + \right. \\ &+ \frac{z}{2}\left(2\tilde{n}_0(1+\tilde{n}_0^2)^{3/2}\kappa - \Delta - \tilde{n}_0^2(\xi-1)\right) + \\ &\left. + \frac{z^3}{8}\tilde{n}_0^2\left(n^2(3+\tilde{n}_0^2) - 3\tilde{n}_0^2(1+\tilde{n}_0^2)\right)\right) + \mathcal{O}(\epsilon^2),\end{aligned} \tag{2.22}$$

where F_1, F_2, and M are integrals related to the path function, and are given in Appendix C[5]. It is important to note that the only restriction on the amplitude of these equations is

[5]It is noted that the integrals $F_1(z)$ and $F_2(z)$ can be expressed as elliptic functions and this is done in Chapter 4.

that imposed by the cusps on the path, specifically, $|s| < s_{max}$, where $g(s_{max}) = 0$.

2.4.2 Steady-State Response

Now that the equations of motion have been averaged and reduced to two first-order autonomous differential equations describing the slow evolution of the amplitude and phase, one can investigate the steady-state response of the system in terms of amplitude, phase, and stability. To do this we set $z' = 0$ and $\phi' = 0$, denote the steady-state values as $(\bar{z}, \bar{\phi})$, solve equations (2.21) and (2.22) for $\cos(\bar{\phi})$ and $\sin(\bar{\phi})$, and use $\cos^2(\bar{\phi}) + \sin^2(\bar{\phi}) = 1$, resulting in an equation relating the applied torque amplitude Γ to the steady-state absorber amplitude $\bar{z}$ and the system parameters, as follows,

$$\Gamma^2 = \left(\frac{\mu \bar{z} n}{2F_1(\bar{z})}\right)^2 + \frac{1}{F_2^2(\bar{z})}\left(\frac{\bar{z}}{2}\left(2\tilde{n}_0(1+\tilde{n}_0^2)^{3/2}\kappa - \Delta + \right.\right. \tag{2.23}$$
$$\left. - \tilde{n}_0^2(\xi - 1)\right) - 2M(\bar{z})\left(\kappa\tilde{n}_0\sqrt{1+\tilde{n}_0^2} + \delta\ell\right) +$$
$$\left. + \frac{\bar{z}^3}{8}\tilde{n}_0^2\left(n^2(3+\tilde{n}_0^2) - 3\tilde{n}_0^2(1+\tilde{n}_0^2)\right)\right)^2.$$

For plotting purposes it is convenient to choose a steady-state amplitude $\bar{z}$ and compute the applied torque (which involves evaluating the integrals in F_1, F_2, and M as a function of $\bar{z}$). Once the amplitude and applied torque have been computed, the absorber steady-state phase $\bar{\phi}$ can be obtained using equations (2.21) and (2.22) set to zero.

It is also of interest to know the resulting torsional vibration amplitude of the rotor. A good measure of this is the rotor angular acceleration $\nu\nu' = \epsilon w' + \mathcal{O}(\epsilon^2)$, which is conveniently captured by $\epsilon w'$. Therefore, one can obtain an approximation of the rotor vibration amplitude from w' using equation (2.14). Of particular interest is the amplitude of the order

n harmonic of this acceleration, since that is the order which the absorber is designed to reduce. This component can be computed via the magnitude of the corresponding complex Fourier coefficient,

$$|w'|_n = \frac{n}{\pi} \mid \int_0^{2\pi/n} e^{-in\theta} w'(\theta) d\theta \mid . \tag{2.24}$$

The reader should note that the $w'(\theta)$ used here is the reduced form of equation (2.14), obtained by substitution of $\lambda = \lambda_{e0} + \epsilon\kappa$ into $\partial r_P^2/\partial s$ and $g(s)$, which results in the following expression for $w'(\theta)$, after keeping only leading order terms in ϵ,

$$w'(\theta) = \Gamma \sin(n\theta) + 2\tilde{n}_0^2 s s' - \frac{\partial g_0(s)}{\partial s} s'^2 + \tilde{n}_0^2 g_0(s) s, \tag{2.25}$$

and where, as mentioned above, $-\tilde{n}_0^2 s$ is substituted for s''. Also, note that the effects of the rollers are not explicit here, since they appear at higher order, but will affect $w'(\theta)$ via their effects on the absorber response. The steady-state response conditions for s and s' are substituted here, and the attendant non-dimensional steady-state rotor acceleration is given to leading order by $\nu\nu' = \epsilon w'$. Note that the absorber and rollers add rotational inertia, and therefore their presence reduces torsional vibrations by a flywheel effect, even if they don't move along their paths, and this must be accounted for in order to assess the dynamic effectiveness of the absorbers [68]. We therefore compare the value of $|w'|_n$ experienced with the absorber free to move, as compared to its value with the absorber locked at its vertex ($s = s' = 0$). According to equation (2.25) the reference condition is given simply by $|w'|_{n,ref} = \Gamma$ and this is denoted as the "reference line" in the following section.

In order to assess the maximum torque range over which the absorbers can operate, it will be useful to know the maximum allowable amplitude of the absorber motion. As discussed

above, this can be determined by solving $g(s_{max}) = 0$. For purposes of doing steady-state analysis within this amplitude level, we will use the approximate cusp amplitude expression derived by Denman [17], which assumes a roller-free order $\tilde{n}_0$ tautochronic path. This approximation for the maximum absorber amplitude is given by

$$s_{max} \approx s_{max,0} = \frac{1}{\tilde{n}_0\sqrt{1+\tilde{n}_0^2}}, \tag{2.26}$$

which is exact in the roller-free case. Here it is assumed that the steady state absorber amplitude must satisfy $\bar{z} < s_{max,0}$. In the examples to follow we will be using a linear tuning of $\tilde{n}_0 \approx 1.5$, for which the cusp amplitude is approximately $s_{max,0} = 0.37$. This will be a sufficient approximation for demonstrating parameter trends in the allowable torque range. In all cases we will compute steady-state responses for torque ranges up to the point where $\bar{z} = 0.36$. For further details on the path cusp points for general paths, see [17, 68].

With expressions describing the steady-state response of the absorber and rotor in hand, we now turn to a specific example of practical interest, which will emphasize how the rollers affect the steady-state system response.

2.4.3 Example

In this example we use the results derived above to investigate how the roller inertia, as determined by the parameters δ and ξ (see Tab. 2.1), affects the response of the system. Our focus here will be on a single absorber that is designed to be exactly tuned with respect to an excitation order of 1.5, that is, we take $\tilde{n} = n = 1.5$. As shown in Fig. 2.4, we will consider a 3×3 matrix of cases with three values of roller inertia and three paths, all of which are close to, or exactly, tautochronic.

We make some simplifying assumptions in order to fix some parameters. First, to simplify the number of roller parameters we can relate ξ to δ by assuming a solid uniform roller, as is typically used in practice. This assumption implies that $i_R = m_R A^2/2$, which corresponds to $\delta = 2\xi$. In addition, we fix the absorber geometry throughout all comparisons by taking $\ell = -0.25$.

	$\delta = 0$	$\delta = \frac{1}{4}$	$\delta = \frac{1}{2}$
$\tilde{n}_0,\ \lambda_{e0}$	**Case I.1** ▪▪▪▪▪ $\tilde{n} = \tilde{n}_0 = 1.5$ $\lambda = \lambda_{e0} = 0.8321$ $(\lambda_e = \lambda_{e0})$	**Case I.2** ——— $\tilde{n} = 1.504$ $(\tilde{n}_0 = 1.5)$ $\lambda = \lambda_{e0} = 0.8321$ $(\lambda_e = 0.8343)$	**Case I.3** —·— $\tilde{n} = 1.508$ $(\tilde{n}_0 = 1.5)$ $\lambda = \lambda_{e0} = 0.8321$ $(\lambda_e = 0.8364)$
$\tilde{n},\ \lambda_{e0}$	**Case II.1** ▪▪▪▪▪ $\tilde{n} = \tilde{n}_0 = 1.5$ $\lambda = \lambda_{e0} = 0.8321$ $(\lambda_e = \lambda_{e0})$	**Case II.2** — — $\tilde{n} = 1.5$ $(\tilde{n}_0 = 1.496)$ $\lambda = \lambda_{e0} = 0.8314$ $(\lambda_e = 0.8336)$	**Case II.3** · · $\tilde{n} = 1.5$ $(\tilde{n}_0 = 1.492)$ $\lambda = \lambda_{e0} = 0.8307$ $(\lambda_e = 0.8350)$
$\tilde{n},\ \lambda_e$	**Case III.1** ▪▪▪▪▪ $\tilde{n} = \tilde{n}_0 = 1.5$ $\lambda = \lambda_e = 0.8321$ $(\lambda_{e0} = \lambda_e)$	**Case III.2** —— $\tilde{n} = 1.5$ $(\tilde{n}_0 = 1.496)$ $\lambda = \lambda_e = 0.8336$ $(\lambda_{e0} = 0.8314)$	**Case III.3** • $\tilde{n} = 1.5$ $(\tilde{n}_0 = 1.492)$ $\lambda = \lambda_e = 0.8350$ $(\lambda_{e0} = 0.8307)$

Figure 2.4: A table depicting the nine roller mass cases used in the simulations shown in Figs. 2.5 and 2.6. The zero roller mass ($\delta = 0$) case (Case x.1) is the same for all three Cases I, II, and III. Whereas, the $\delta = 1/4$ (Case x.2) and $\delta = 1/2$ (Case x.3) roller mass Cases will have different linear and nonlinear tuning values as shown. Therefore, seven of the nine total Cases have unique pairs of linear and nonlinear tuning values which is why only seven response curves are shown in Fig. 2.5 with linetypes indicated in this table.

This investigation considers three values for the roller masses, which includes a range of practical interest. All of the details for the nine roller mass cases are depicted in Fig. 2.4. The first value is zero roller mass ($\delta = 0$), corresponding to linear tuning $\tilde{n} = \tilde{n}_0$ and a tautochronic path with $\lambda = \lambda_e = \lambda_{e0}$; these are labeled as Case x.1 in Fig. 2.4, where x takes on I, II, or III. We also consider $\delta = 1/4$ (Case x.2) and $\delta = 1/2$ (Case x.3), for which

the linear tuning is $\tilde{n}$ ($> \tilde{n}_0$) and the tautochronic path has λ_e ($> \lambda_{e0}$). Each of the three values of roller mass will be used for the following three cases: In Case I we fix $\tilde{n}_0 = 1.5$ which then also fixes λ_{e0}; this is the case in which the roller inertia is ignored, and thus the zero roller mass path will be exactly tautochronic. In this case, we will be able to quantify the effects of ignoring roller mass in both the linear and nonlinear tuning. The reader should realize that in Case I, the absorber COM paths for $\delta = 0$, $1/4$, and $1/2$ are exactly the same because the initial radius of curvature of the path ρ_0 is fixed for a fixed $\tilde{n}_0$ (see equation (2.5)) and λ_{e0} is independent of roller mass (recall $\lambda_{e0} = \tilde{n}_0^2/(\tilde{n}_0^2 + 1)$).

In Case II, we fix $\tilde{n} = 1.5$ and use the $\lambda = \lambda_{e0}$ corresponding to the roller-free linear tuning. This corresponds to the case in which the roller inertia is accounted for in the linear tuning, but ignored for nonlinear tuning effects. This was done in Denman [17], and was standard practice, since it was not known until the present work that a tautochronic path existed that accounts for the inertia of the rollers. As noted above, the initial radius of curvature depends on the roller mass for fixed values of $\tilde{n}$, c, and ℓ. So, in this situation the radius of curvature depends on the value of δ, both initially (ρ_0) and continually up to the cusps (λ_{e0}).

For Case III we fix $\tilde{n} = 1.5$ and use the correct tautochronic path for rollers, for which $\lambda = \lambda_e$. Similar to Case II, the absorber paths have different radii of curvature. In fact, the initial radius of curvatures will be the same for Cases II and III since the linear tuning is computed in the same way. However, Case III will have different non-linear tuning, that is, λ_e instead of λ_{e0}.

Figure 2.5 shows the steady state absorber response amplitude $\bar{z}$ versus the applied torque amplitude Γ for the three values of roller inertia for each of the three cases described above

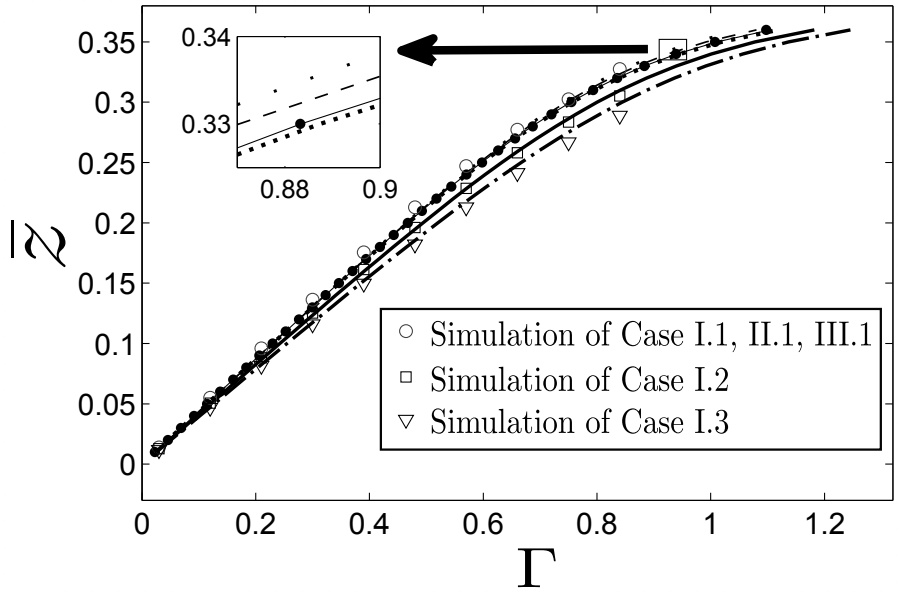

Figure 2.5: Steady-state absorber response amplitude $\bar{z}$ vs. applied torque amplitude Γ for the three Cases described in the text. The linetypes for the Case I responses are indicated in the first row of Fig. 2.4. The linetypes for the Case II responses are indicated in the second row of Fig. 2.4. The linetypes for the Case III responses are indicated in the third row of Fig. 2.4. Only one response line exists for Cases (x.1) because for $\delta = 0$ the linear and nonlinear tuning are equal for all three Cases. The final three lines of the legend correspond to results from simulations of equations (2.3) and (2.4). Only simulations of Case I is depicted since all are very close to one another. Parameter values: $\epsilon = 0.10$, $\mu = 0.30$, $\ell = -0.25$, $n = 1.5$.

and in Fig. 2.4. Note that there are seven response curves, since for zero roller inertia, $\tilde{n} = \tilde{n}_0$ and $\lambda_e = \lambda_{e0}$, and thus the response is the same for Cases (x.1) for x = I, II, III (see the first column ($\delta = 0$) in Fig. 2.4). The line types for the seven response curves are indicated in Fig. 2.4. Additionally, note that in plotting the steady-state amplitude response in all Cases, except the simulated ones as shown in Fig. 2.5, the non-linear tuning parameter λ is controlled using the parameter κ (as defined in Section 2.4). Case I, in which the rollers are ignored, is described by the first row of Fig. 2.4, and these three response curves in Fig. 2.5 show the largest deviation of the three Cases. The deviation present in Case I shows a (desirable) hardening response as the roller mass is increased. Therefore, if

an absorber is designed with a tautochronic path that ignores the rollers, they will actually gain some torque range before the cusps are reached, albeit at a slight reduction in absorber effectiveness (as shown in Fig. 2.6 and described below). For Cases II and III all plots are virtually identical to the roller-free curve from Case I (i.e. Case I.1), which implies that for the roller inertia values used here, if one accounts for the rollers in the linear tuning $\tilde{n}$, the nonlinear tautochronic roller correction is essentially inconsequential. The main point of these results is that one need only account for roller inertia in the linear tuning.

Simulations of the non-linear equations of motion (using equations (2.3) and (2.4)) are also shown in Fig. 2.5 to illustrate the accuracy of the averaged solutions. Note that only Case I is simulated because the results are virtually indistinguishable in terms of amplitude, only the torque range differs.

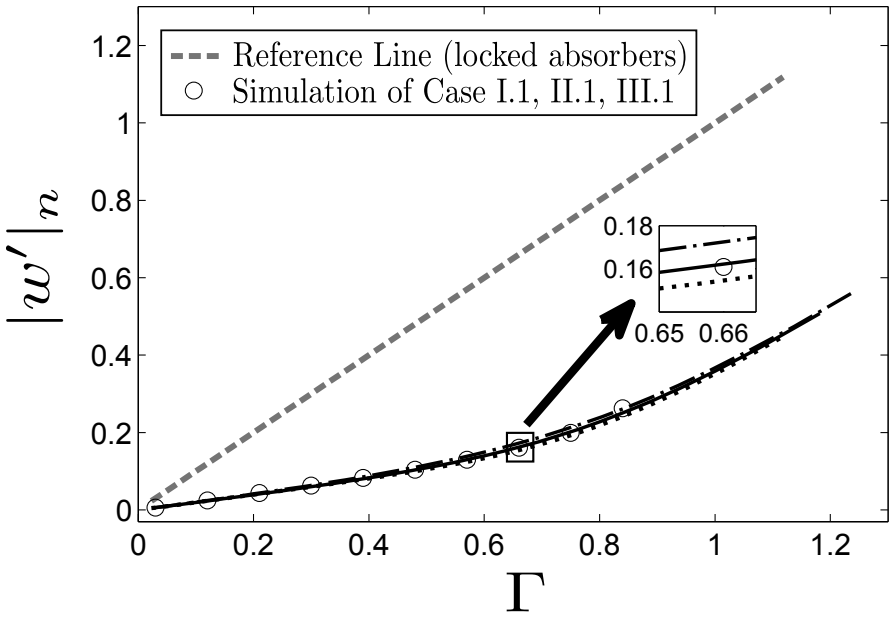

Figure 2.6: Order n harmonic amplitude of the rotor response, $|w'|_n$, vs. applied torque amplitude Γ for Case I. All absorber designs shown in the legend of Fig. 2.5 result in indistinguishable rotor response amplitudes, but different torque ranges. Only a simulation of the full nonlinear equations using $\delta = 0$ (Cases x.1) is depicted since the other roller mass values are indistinguishable. Parameter values: $\epsilon = 0.10$, $\mu = 0.30$, $\ell = -0.25$, $n = 1.5$.

Figure 2.6 shows the amplitude of the order n harmonic of the rotor, $|w'|_n$, as it depends on the level of applied torque Γ, along with the reference line. Here we show only the three curves from Case I, since all these curves fall very close to the roller-free curve of Case I, although they have different end points, set by the cusp limits. This shows the effectiveness of the absorber at attenuating torsional vibration levels at this order. It is important to note that if one ignores the effects of the rollers, the resulting response predictions are conservative in terms of the torque range, since the rollers provide an increased hardening (that is, increased effective stiffness) for the absorber response. In terms of the rotor response, if the absorber is slightly over-tuned using $\tilde{n}_0$ with respect to the excitation order n, adding roller mass results in the absorber being slightly less effective at attenuating torsional vibrations, as is seen in Fig. 2.6. This is because the tuning order will increase, which moves the absorber further away from the resonant excitation of order n. Lastly, simulation of the non-linear equations of motion using equations (2.3) and (2.4) are shown in Fig. 2.6 to illustrate the accuracy of the averaged equations. Note that only the $\delta = 0$ case is presented here because results from the other cases are virtually indistinguishable.

To compliment Figs. 2.5 and 2.6, simulations of the non-linear equations of motion are displayed in Figs. 2.7 and 2.8. Note that in these plots the independent variable is the rotor angle θ, playing the role of time. Shown in Fig. 2.7 is the steady-state absorber response, normalized by the amplitude of the order n applied torque Γ. Figure 2.7 shows that the normalized absorber amplitude s_{peak}/Γ decreases as the applied torque Γ increases, which is a result of the non-linear hardening behavior of the absorber response, as shown in Fig. 2.5. Shown in Fig. 2.8 is the normalized steady-state rotor acceleration, w'/Γ, over the same θ interval, for the applied torque levels given in Fig. 2.7, plus the case $\Gamma = 0.40$. Note that

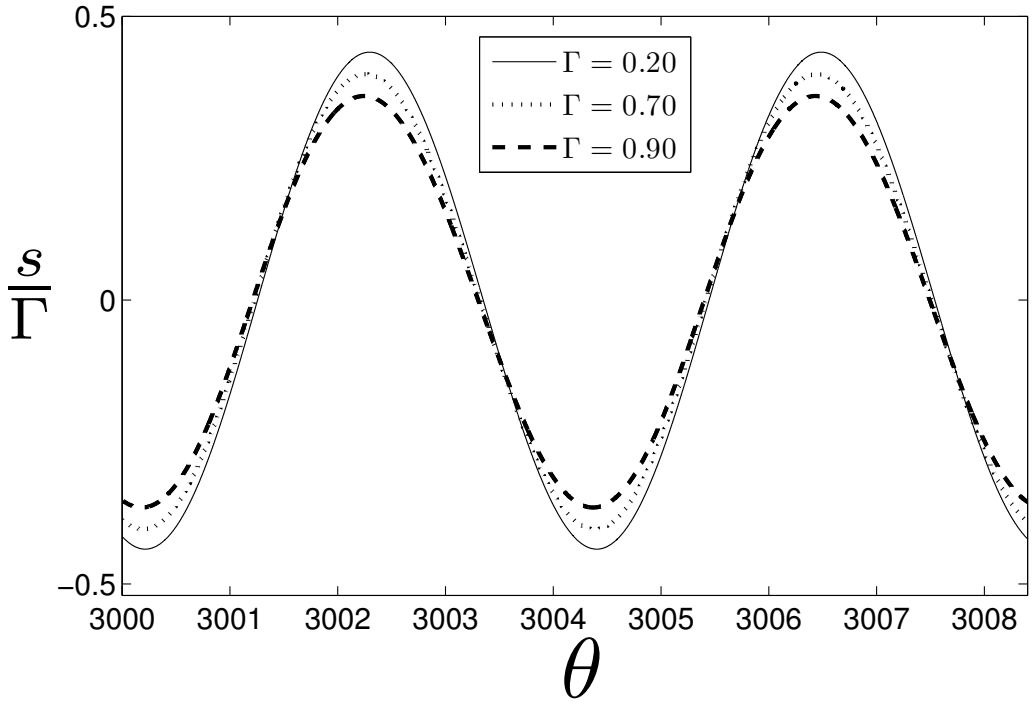

Figure 2.7: Steady-state absorber response normalized by the applied torque amplitude Γ vs. the rotor angle θ for $\delta = 1/2$ from Case III (i.e. Case III.3). The results demonstrate the hardening nature of the system. Parameter values: $\epsilon = 0.10$, $\mu = 0.30$, $\ell = -0.25$, $n = 1.5$.

the rotor acceleration contains a few significant harmonics, in fact, three, and their relative contributions change as Γ increases. Recall that if the absorbers were locked there is only an order n harmonic in the steady-state rotor acceleration, and therefore, the additional harmonics are a result of the absorber dynamics and their nonlinear interactions with the rotor. The higher harmonics are prominent since the order n harmonic is largely reduced by the absorbers.

2.5 Conclusions

There are two main contributions of this investigation. First, a tautochronic absorber path that accounts for roller inertia has been found. Second, a perturbation analysis of the

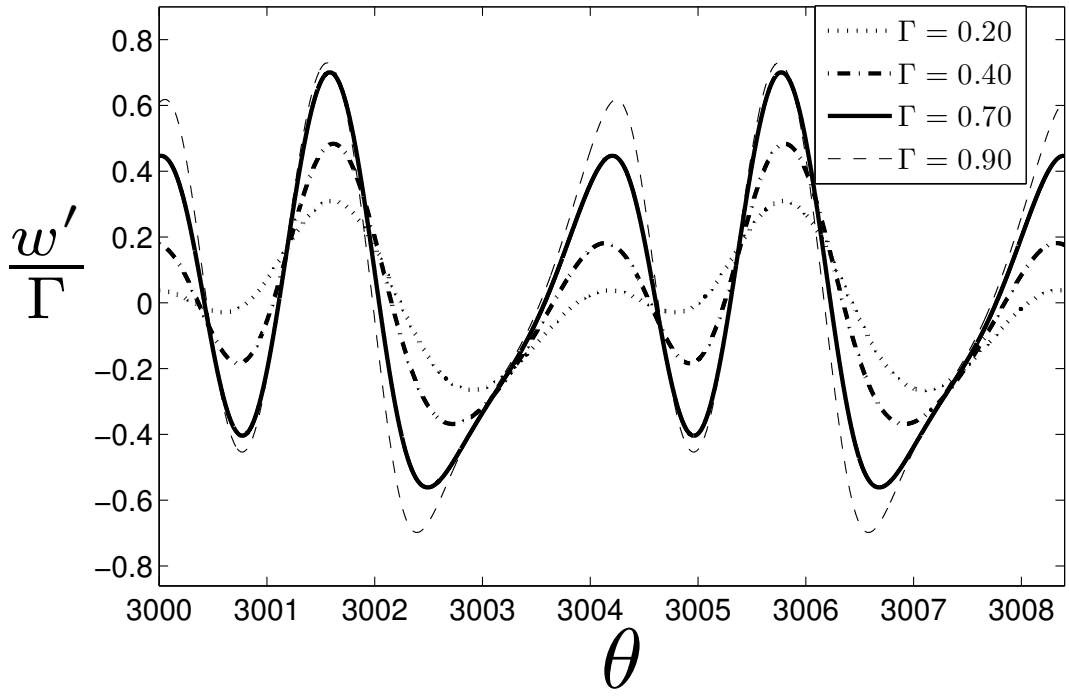

Figure 2.8: Steady-state rotor acceleration w' vs. rotor angle θ for $\delta = 1/2$ from Case III (i.e. Case III.3). Note that the rotor acceleration is composed of multiple harmonics and the relative contribution of these harmonics depends on the torque amplitude. Parameter values: $\epsilon = 0.10$, $\mu = 0.30$, $\ell = -0.25$, $n = 1.5$.

equations of motion shows that the response of a system with a nearly tautochronic absorber that includes roller inertia in the linear tuning parameter $\tilde{n}$ is largely insensitive to the choice of the nonlinear tuning parameter λ. In fact, if the rollers are ignored altogether in the absorber design, the analysis shows that the system can handle a greater torque range with virtually no change in the vibration levels of the rotor. This is mostly due to the fact that the rollers will affect the linear tuning which results in a roller-free absorber design that will be off its ideal tuning value. To a lesser degree, it is also because the rollers will provide a slight hardening effect due to their influence on the nonlinear tuning. However, it appears that for the sizes of rollers typically in use, one needs to include their effects only in the linear tuning in order to achieve satisfactory performance.

Chapter 3

Transient Response of Forced Nonlinear Oscillators

3.1 Introduction

Most studies of the response of nonlinear vibratory systems subjected to harmonic excitation focus on steady state response. Typical investigations consider periodic responses, stability and bifurcations of these, quasiperiodic responses, and chaotic responses. In this chapter we consider the transient response of the Duffing equation subjected to harmonic excitation, focusing on overshoot that occurs when the excitation is suddenly switched on. The Duffing oscillator is an archetypical nonlinear system that arises in many engineering problems [5, 7, 20, 21, 29, 51, 61, 67]. There exists a large body of work on the steady state response and its stability for this classical oscillator; see, for example, [51]. However, in certain design scenarios it is useful to know the short-term transient dynamics of the response [40]. For instance, one may have design constraints on the peak amplitude of a system response,

and the transient response amplitude may violate this constraint, even when the steady state amplitude does not. Such an application motivated the present study, specifically, the response of a vibration absorber that starts in an inactive state and is suddenly brought into conditions for it to be active, leading to beating type transients. Another consideration is that a transient can sometimes result in the system ending up in an undesirable steady state, in situations where multiple stable steady state responses exist. For nonlinear systems one can investigate such transient responses through numerical simulations, and in some cases this is the only feasible approach. However, for simple systems, analytical results can be derived and provide predictive results that are useful in design. Here we derive such results for the Duffing oscillator.

The approach for investigating the transient response of a linear oscillator is straightforward, since one can express the exact solution of the differential equation governing the system response in terms of the system and excitation parameters and initial conditions [28, 69, 74]. Another approach is to find a constant of motion for the system that relates the position, velocity, system parameters, and initial conditions, from which the peak response can be determined [10, 36, 37]. Both approaches provide exact analytical results for the transient response. However, the constant of motion approach typically does not apply for nonautonomous systems. As for nonlinear systems, the direct solution approach can be used only in a few special cases [8], whereas the latter approach can be applied to a number of nonlinear systems [9, 18, 19, 60]. In addition, the constant of motion approach is well suited for problems such as determination of the overshoot, in which the velocity is known (zero in this case) at some desired system position (peak amplitude in this case). A limitation with the constant of motion approach is that it is not directly applicable to

systems with time-dependent excitation. However, the method of averaging provides a mean of removing this time dependence for a certain class of systems, so that a constant of motion for the averaged system can be obtained [71]. Only a few treatments of transient response in non-linear systems are known to the authors, see [15, 20, 25, 32, 39, 42, 64], and we know of no published analytical results for the overshoot of the Duffing oscillator, as considered here.

The primary focus here is an analytical treatment of the transient overshoot problem of the Duffing oscillator that allows for predictions. The main result is a closed form expression for the overshoot for the case of zero damping when the system starts with zero initial conditions. It is shown that this undamped result provides a useful, conservative bound for system overshoot, one that is quite accurate for systems with light damping. The analysis is aided by a convenient scaling of the position and time such that the three system parameters (force magnitude, frequency detuning, and nonlinearity) are combined into a single parameter χ governing the response of the scaled system. The results are compared against simulations of the original non-linear oscillator and the averaged equations to demonstrate their accuracy.

3.2 The Model, Averaged Equations, and Scaling

The system of interest here is a single degree of freedom oscillator with small damping, nonlinearity, and harmonic excitation, driven near resonance, expressed as

$$x'' + \omega_0^2 x = \epsilon \left(F \sin(\omega t + \phi) - \xi x^3 - \mu x' \right), \tag{3.1}$$

where ϵ is a small parameter. In order to apply the method of averaging, we use the standard change of coordinates,

$$x(t) = a(t)\sin\left(\omega t + \psi(t)\right), \tag{3.2}$$
$$x'(t) = a(t)\omega\cos\left(\omega t + \psi(t)\right),$$

which will have slowly varying amplitude and phase when $\epsilon << 1$ and the forcing is near resonance, $\omega \approx \omega_n$. Constraining the response of equation (3.1) to be in the form (3.2), defining the frequency detuning as $\epsilon\sigma = \omega^2 - \omega_0^2$, and averaging over one period of the excitation, results in the following standard averaged equations

$$r' = -\frac{\epsilon}{2\omega}\left(F\sin(\Phi) + \mu r\omega\right), \tag{3.3}$$
$$r\Phi' = \frac{\epsilon}{2\omega}\left(\frac{3}{4}\xi r^3 - F\cos(\Phi) - \sigma r\right), \tag{3.4}$$

where r is the averaged amplitude and $\Phi = \varphi - \phi$ is the relative phase between the averaged oscillator phase φ and the phase of the forcing. In addition, since the forcing phase ϕ is constant we have replaced φ' with Φ' in equation (3.4) for convenience in the subsequent analysis. The steady state response of equations (3.3) and (3.4) has been studied extensively.

We reduce the number of system parameters by scaling the dependent variable r and the independent variable t as follows

$$t = \left(\frac{4\omega}{\epsilon\sigma}\right)\tau, \quad r = 2\left(\frac{F}{\sigma}\right)p, \tag{3.5}$$

where it is assumed that $\sigma \neq 0$. Utilizing this scaling in equations (3.3) and (3.4) results in

the rescaled averaged equations,

$$\frac{dp}{d\tau} = -\sin(\Phi) - Dp \tag{3.6}$$

$$p\frac{d\Phi}{d\tau} = 4\chi p^3 - \cos(\Phi) - 2p, \tag{3.7}$$

where

$$\chi = \frac{3}{2}\xi\left(\frac{F^2}{\sigma^3}\right) \quad \text{and} \quad D = 2\left(\frac{\mu\omega}{\sigma}\right). \tag{3.8}$$

Note that this scaling introduces a complication of the results exactly at resonance, where $\sigma = 0$. However, it will be shown that this is not a limitation for the overshoot problem since the results can be computed in the limit $\sigma \to 0$. Also, it is important to note that when $\sigma < 0$ both position and time of the scaled system become negative, since $\epsilon > 0$ and $\omega > 0$. In this case, the system is solved in reverse time, which may lead one to think the system amplitude response will grow exponentially. However, the sign of the scaled damping coefficient depends on σ as well, such that solving reverse time will result in exponential decay, as expected. In addition, the results presented subsequently are simplified by making use of the inherent symmetry in the hardening vs. softening Duffing responses, in such a manner that negative amplitude responses can be ignored. However, it will be shown that this symmetry between softening vs. hardening Duffing oscillators does not carry over to the phase response, and therefore we will need to consider the individual cases for the phase response.

3.2.1 The Steady-State Response

The steady state response of the scaled system is obtained by letting $dp/d\tau = 0$ and $d\varphi/d\tau = 0$, which results in the following equations for the steady state amplitude $\bar{p}$ and phase $\bar{\Phi}$,

$$(D\bar{p})^2 + (4\chi\bar{p}^3 - 2\bar{p})^2 = 1, \tag{3.9}$$

$$\tan\left(\bar{\Phi}\right) = \frac{-D}{4\chi\bar{p}^2 - 2}. \tag{3.10}$$

It is seen that this scaling has reduced the system parameter dependence of the steady state response from four (ξ, F, σ, μ) to two (χ, D). In general, one can solve equation (3.9) analytically to obtain six roots governing the steady state amplitude $\bar{p}$ as a function of D and χ. However, for plotting the steady state response we use only the three positive roots, since the other three are symmetric with respect to $\bar{p} = 0$ and don't provide any additional information about the steady state amplitude. These roots are given explicitly in Appendix D. More specifically, the three ignored roots are negative, which for $\sigma < 0$ lead to a positive $\bar{r}$ (see equation (3.5)) that match the positive roots for $\bar{p}$ when $\sigma > 0$ case. It is also important to note that there is a symmetry in the steady state frequency responses of two Duffing oscillators wherein one is hardening (ξ_1) and the other is softening (ξ_2), such that $\xi_1 = -\xi_2$, with all other parameters fixed. As seen by the definition of χ, the frequency response of these two systems are symmetric about $\sigma = 0$, provided the other parameters are the same. When considering the steady state phase response, this symmetry does not exist, that is, $\bar{\Phi}_1 \neq \bar{\Phi}_2$ for $\sigma_1 = -\sigma_2$, as can be seen from equation (3.10), where the steady state phase depends on the sign of σ through the damping coefficient D. Therefore, in the scaled system, for a given value of the damping coefficient D, one distinct steady state amplitude exists as

χ is swept, an example of which is shown in Fig. 3.1 (a). However, the steady state phase can take one of two forms, depending on the sign of D, which is governed by σ; these are shown in Fig. 3.1 (b) and (c). As expected, Fig. 3.1 (a), (b), & (c) exhibit the familiar bistable region over which three steady state responses exist for a single value of χ, two of which are stable. We refer to these in terms of "the lower branch" (labeled as **A**), "the middle branch" (labeled as **B**), and "the upper branch" (labeled as **C**), designated by their relative amplitudes. The bistable region is given by $\chi_1^\star < \chi < \chi_2^\star$, which depends on the damping coefficient D. Explicit formulas for $\chi_1^\star$ and $\chi_2^\star$ are given in Appendix D. For the case of zero damping ($D = 0$), the results simplify to $\chi_1^\star = 0$ and $\chi_2^\star = 8/27$.

3.2.2 The Averaged Equation Phase Portraits

The (p, Φ) phase portraits of the averaged equations are very useful for analyzing the transient trajectories of the Duffing equation, and the remainder of the chapter will make use of this information. In fact, for many of the results we will focus on the undamped case, $D = 0$, since this case yields analytical solutions that provide a good approximation, and a useful bound, for lightly damped systems.

Figure 3.2 (a)-(c) show phase portraits of a lightly damped system ($D = 0.30$) for three values of χ, displaying the three topologically distinct cases.[1] Attendant sample transient time responses are shown in Fig. 3.2 (d)-(f) for the initial conditions (p_0, Φ_0) labeled as IC#1, IC#2, and IC#3. Figure 3.2 (a) shows a sample phase portrait for $\chi < \chi_1^\star$. For this

[1]Note that we have not shown the case when $D \neq 0$ and $\chi \in (0, \chi_1^\star)$, which is the case of the lower branch **A** existing alone. However, as seen from Fig. 3.1 (a)-(c), this case will be qualitatively similar to the case of $\chi < 0$, which is shown in Fig. 3.2 (a), except that the equilibrium point **C** is replaced with equilibrium **A**. Also note that this case will not exist for $D = 0$.

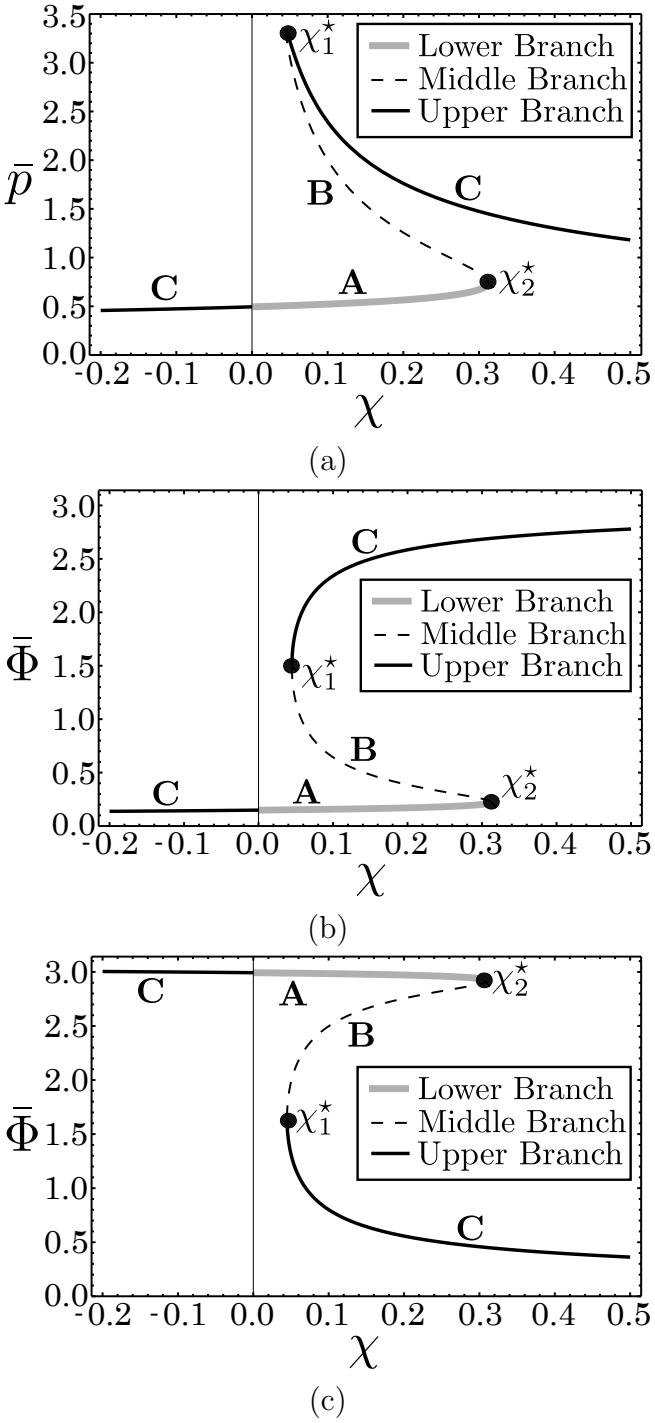

Figure 3.1: Steady-state response of the scaled averaged system as a function of χ. (a) Steady-state amplitude; (b) Steady-state phase for $D = 0.30$, relevant for $\sigma > 0$; (c) Steady-state phase for $D = -0.30$, relevant for $\sigma < 0$.

range of χ only the upper branch (**C**) exists. Figure 3.2 (d) depicts a sample transient time response for this case with initial condition IC#1, specifically, with zero amplitude, $p_0 = 0$. Since $p(\tau)$ describes the amplitude envelope of the oscillatory response with frequency near ω, the oscillation in p demonstrates the beating nature of the x response. Note that p and x both have a peak amplitude of p_{peak}, and that p decays to the steady state amplitude $\bar{p}_C$ of branch (**C**). The more interesting phase portrait for the bistable case is shown in Fig. 3.2 (b), for a value of $\chi \in (\chi_1^\star, \chi_2^\star)$. As depicted in the time responses shown in Fig. 3.2 (e) & (f), depending on the initial conditions (p_0, Φ_0), generic transient trajectories approach either (**A**) or (**C**). The sample initial conditions shown have equal initial amplitudes and different initial phases, as indicated by IC#2 and IC#3 in Fig. 3.2. As usual, the basins of attraction for these two stable outcomes are separated by the stable manifold of the saddle point (**B**). Lastly, Fig. 3.2 (c) shows a sample phase portrait for $\chi > \chi_2^\star$, for which **C** is the only possible steady state.

We now turn to an analysis that offers predictive results for the peak of the transient response.

3.3 Percent Overshoot for the Undamped System

In this section an analytical result for the percent overshoot for the undamped Duffing oscillator is derived. In general, the percent overshoot of a system is defined as

$$\%\ Overshoot = \left(\frac{pmax - pss}{pss}\right) \times 100, \tag{3.11}$$

where p_{max} is the peak amplitude during a transient response and p_{ss} is the resulting steady state amplitude (given by one of the roots $\bar{p}$). We begin by deriving an energy-like constant of motion for the undamped ($D = 0$) scaled averaged equations. This is a fourth order polynomial in p whose roots dictate the important features of the transient response. These roots are a function of the initial conditions (p_0, Φ_0), the parameter χ, and the relative phase of the response Φ. It will be shown that the peak amplitude of the response occurs at a relative phase of either $\Phi = 0$ or $\Phi = \pi$, so that the roots can be expressed in terms of the initial conditions and χ. One feature of interest will be the case where the transient response approaches the saddle point **B** for $\chi \in (\chi_1^\star, \chi_2^\star)$, since this will represent the basin boundary in the bistable case.

3.3.1 Transient Response Amplitudes

The averaged equations (3.6) and (3.7) with $D = 0$ is conservative and has a constant of motion that can be determined by combining equations (3.6) and (3.7) into a differential equation for $p(\Phi)$. Integrating this exact equation leads to the following integral of motion,

$$-\chi p^4 + p^2 + p\cos(\Phi) = c_1, \tag{3.12}$$

where c_1 is an arbitrary constant determined by the initial conditions (p_0, Φ_0) and χ. Equation (3.12) allows one to construct the phase portrait for the conservative averaged system in the usual manner: Given initial conditions (p_0, Φ_0) one can obtain c_1 and then solve equation (3.12) for phase plane trajectories in the form $p(\Phi)$ (or, simpler in this case $\Phi(p)$, since it has only two branches). An example phase portrait is shown in Fig. 3.3 for $\chi = 0.066 \in (\chi_1^\star, \chi_2^\star)$, which is an undamped version of the phase portrait shown in Fig. 3.2 (b).

In general, equation (3.12) will have four roots for p that can be obtained exactly and will generate the level curves shown in Fig. 3.3; these roots are presented in Appendix D. In order to generate the level curves shown in Fig. 3.3, as well as the level curves when χ is outside of the bistable region, one needs only three of the four roots. Furthermore, it turns out that only two of these roots involve trajectories that include the peak amplitude about the steady state equilibria, and therefore the other two roots are ignored for the present study. The two roots governing the transient trajectories of interest are given in equations (F.1) and (F.2) in Appendix F. Given a value of χ in the bistable region, and initial conditions (p_0, Φ_0), the root p_1 (given in equation (F.1)) will generate a transient trajectory as a function of Φ about the lower branch steady state equilibria **A**. On the other hand, for any value of χ and initial conditions (p_0, Φ_0), the root p_2 (given in equation (F.2)) will generate a transient trajectory as a function of Φ about the upper branch steady state equilibria **C**.

These results provide an analytical expression for the percent overshoot of the undamped Duffing oscillator. For χ in the bistable region, the peak amplitude of transient trajectories approaching branch **A** (branch **C**, respectively) can be determined by evaluating the root p_1 (p_2, respectively) at $\Phi = \pi$ ($\Phi = 0$, respectively). Outside the bistable region, the transient peak amplitude about the upper branch **C** can be determined by evaluating root p_2 at $\Phi = \pi$ when $\chi < \chi_1^\star = 0$, and at $\Phi = 0$ for $\chi > \chi_2^\star = 8/27$.[2] Note that for a negative initial amplitude condition $p_0 < 0$, corresponding to $\sigma < 0$ according to equation (3.5), the determination of the peak amplitude p_{max} is slightly modified, the details for which are given in Appendix E. To determine the percent overshoot, the steady state amplitudes for

[2]Although we have not shown the undamped portraits when χ is outside the bistable region, the interested reader can refer to the damped phase portraits shown in Fig. 3.2 (a) & (c) to clarify where Φ is evaluated.

A and **C** are also required. These can be determined as a function of χ by solving equation (3.9) for $\bar{p}$, using the analytical expressions given in Appendix D (equations (D.1)-(D.2)) evaluated at $D = 0$. From the peak and steady state amplitudes, the percent overshoot can be computed in an explicit form. This result is rather cumbersome, due to the roots involved, and is therefore not given explicitly, but it is straightforward to compute.

3.3.2 Basin Separation Trajectory

It is also of use to determine the location of the saddle point **B** (see equation (D.3)), since this, along with the attendant transient trajectories, determines basin boundaries for steady-state fixed points **A** and **C**. This information is useful if it is desired to have a system reach a particular steady state when operating in the bistable region.

To begin, we first derive the initial conditions that will result in a transient trajectory on the stable or unstable manifolds of **B** when $D = 0$. This is done by evaluating the initial conditions for equation (3.12) at the steady state amplitude $p_0 = p_B$ and phase $\Phi_0 = \pi$, resulting in the following condition on equation (F.3),

$$\begin{aligned} c_1^\star(\chi) &= c_1(\chi, p_B, \pi) \\ &= \frac{1}{288\chi^3}\Big(4\chi(3\nu)^{2/3} + 192^{1/6}\delta\nu^{1/3}\Big(\frac{9}{2}\nu^{1/3} - 3^{2/3}\Big) + \\ &\quad + 3\chi^2\Big(16 - 18(3\nu)^{1/3} + 9(3\nu)^{2/3}\Big)\Big), \end{aligned} \tag{3.13}$$

where

$$\nu = \delta\sqrt{3} - 9\chi^2, \tag{3.14}$$
$$\delta = \chi^{3/2}\sqrt{27\chi - 8},$$

for $\chi \in (0, 8/27)$. One can now use $c_1^\star$ in the expressions for p_1 and p_2 to generate stable and unstable manifolds, as shown in Fig. 3.4 (a)-(c). The trajectory of particular interest is the stable manifold, which is obtained from $c_1^\star$ in the expression for p_1 (equation (F.1)).

In general, these undamped basin boundaries provide a good approximation for the basin boundaries of the lightly damped system near the saddle. These results can be used as follows: Suppose that the steady state at **A** is desired for all initial phases, then the maximum initial amplitude allowed is given by $p_{cr} = p_1(\chi, 0, c_1^\star)$, as indicated by the horizontal lines in Fig. 3.4 (a) & (b) for two different values of χ. Note that for $\chi \in (4/27, 8/27)$, no such p_{cr} exists, since at $\chi = 4/27$ the homoclinic orbit to **B** changes character such that all small amplitude initial conditions lie in the basin of **C**, an example of which is shown in Fig. 3.4 (c).

3.3.3 Numerical Examples

In this section two examples are shown to illustrate the main overshoot results, and the benefits of introducing the parameter χ. Although these examples consider only the case of zero initial amplitude ($p_0 = 0$, $\Phi_0 \in [0, 2\pi)$), corresponding to $c_1 = 0$, results for any initial conditions can be obtained by varying c_1. The first example compares the percent overshoot for systems with three different sets of original system parameters (F, ξ, σ) that all yield the same value of χ, and thus the same percent overshoot. The second example shows how the

percent overshoot varies as a function of χ in the bistable region. Both examples show the percent overshoot relative to the lower branch **A**, since this is the resulting steady state for $p_0 = 0$ when $\chi < 4/27$. However, in the second example, for $\chi > 4/27$ and $\chi < 0$, the zero amplitude initial conditions result in a percent overshoot relative to **C**.

For the case of zero initial conditions ($c_1 = 0$) and zero damping ($D = 0$), the percent overshoot is a function of χ only. Figure 3.5 (a)-(c) show simulations of the original equation (3.1) for three different sets of system parameter values that each give $\chi = 0.094$. The overshoot is calculated using the explicit expressions for the peak and steady state amplitudes for response **A** in equation (3.11); these expressions are equation (D.1), from Appendix D for the steady state amplitude, and equation (F.1) evaluated at $\Phi = \pi$ for the peak amplitude, from Appendix F. The result for $\chi = 0.094$ is a predicted percent overshoot of 115.8%. This prediction is compared with the results from direct simulations of equation (3.1), which are indicated in the figure caption, showing the accuracy of the results. Note that the differences in system parameters result in differences in the amplitude scales and the transient beat frequencies, but the percent overshoot is essentially identical in all three cases.

We now consider how the percent overshoot resulting from zero amplitude initial conditions depends on χ. The analytical results are shown in Fig. 3.6 (a), where the overshoot relative to branch **C** is shown by the gray curves and those relative to branch **A** are shown by the black curve. Note that the percent overshoot for a linear undamped system is 100%, and there is transition at $\chi = 0$ from percent overshoot values less than 100% to those larger than 100%. Due to the nature of χ, this can be interpreted in various ways. For example, the overshoot for a hardening system ($\xi > 0$) driven below resonance ($\sigma < 0$) will be less than 100% and it can go only to **A**, while that for a softening system ($\xi < 0$) driven below

resonance ($\sigma < 0$) will be greater than 100% in its transition to **A**. Note that the maximum possible overshoot is 173%, for systems, obtained just below $\chi = 4/27$. The transition at $\chi = 4/27$ corresponds to the case when the zero amplitude initial trajectory is on the stable manifold of **B**. For $\chi > 4/27$, zero amplitude initial conditions result in transient trajectories headed towards **C**, and in this case the percent overshoot is less than 100%, since the difference between the peak and steady state amplitude is smaller for upper branch trajectories. Lastly, note that as $\chi \to \pm\infty$ the percent overshoot is asymptotic to the limiting value of 58.74%, which corresponds to the percent overshoot at resonance, $\sigma = 0$, for branch (**C**).

Figure 3.6 (b) shows a comparison of the analytical results (those shown in Fig. 3.6 (a)) and simulations of both the original Duffing equation (3.1) and the averaged equations (3.6) and (3.7), for the case of zero amplitude initial conditions. These results demonstrate the accuracy of the analytical method, and how it degrades as one increases the value of ϵ.

3.4 Conclusions

We have derived an approximate analytical method for predicting the overshoot for the transient response of a weakly nonlinear Duffing oscillator that is harmonically forced near resonance. The method makes use of the system's averaged equations, which yield an integral of motion in the undamped case, by which the system parameters and initial conditions can be related to the amplitude and phase of the system response. The resulting equation for the amplitude is a fourth order polynomial, which can be solved as function of the response phase, system parameters, and initial conditions. This gives analytical expressions with parameter dependence for the amplitude response, with useful information about the peak amplitude and, for bistable systems, the ultimate steady state response achieved. A unique

scaling reduces the problem to two parameters, χ, that combines the force magnitude F, the frequency detuning σ, and the nonlinearity ξ, and D, which involves damping. Thus, the undamped results, which provide a useful bound for the overshoot in lightly damped systems, depend on a single parameter. Of course, the presence of damping will alter these results. A correction for small D has been computed and is given in Appendices G & H. However, the payoff is small in comparison with the extensive nature of these calculations and therefore it seems to be more efficient to simply obtain the damped overshoot by simulating the damped average equations.

The results presented here are being used to predict overshoot for centrifugal pendulum vibration absorbers, which, in some applications, are activated when suddenly subjected to near resonant excitation [45–47,69]. These absorbers must be designed to not exceed specified amplitudes, even during startup, and so transient predictions such as those derived here are of great practical value. For the case of tautochronic absorbers [11, 14, 68, 70], the system nonlinearities are much more complicated than the cubic term in the Duffing equation, yet we have shown that their averaged equations are integrable in the undamped case, so that similar predictive results can be achieved for that system [45–47]. Furthermore, this percent overshoot approach has also been applied to the case of parametric resonance and it has been found to produce simpler formulas for the overshoot than those given here. In fact, for the case of near zero initial conditions (i.e. $p_0 \approx 0$) it is remarkably found that the percent overshoot is simply $100(\sqrt{2}-1)$, and is therefore independent of the system parameters contained. These results include experimental evidence of the constant overshoot for near zero initial conditions, as well as an outline for computing the overshoot for non-zero initial conditions [44]. These extensions suggest that the approach may be quite general for weakly

nonlinear systems of a more general form, and quite possibly for classes of conservative strongly nonlinear systems with periodic excitation.

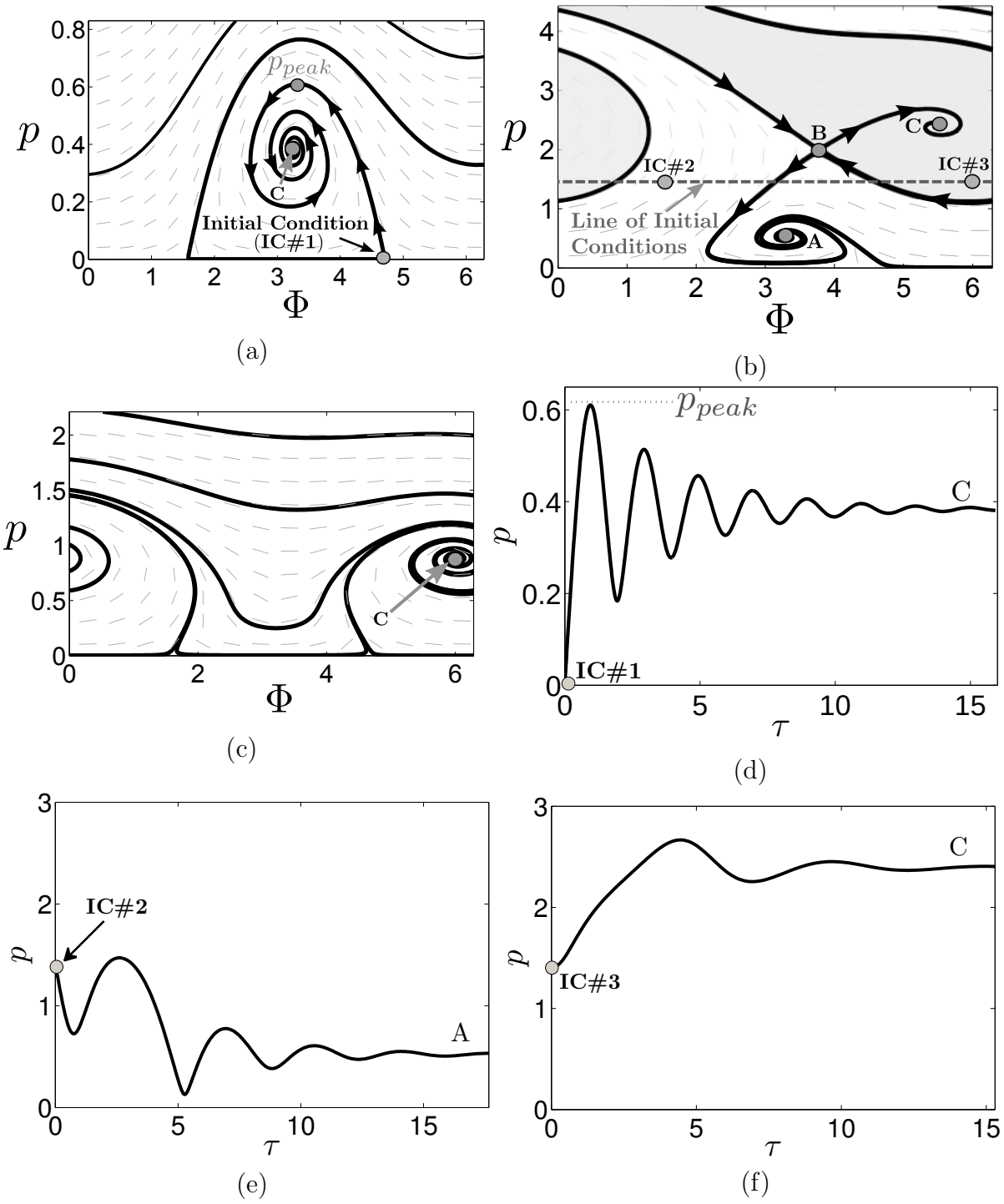

Figure 3.2: Sample phase portraits and transient time traces for three values of χ, with $D = 0.30$. (a) Phase portrait for $\chi = -1 < \chi_1^\star$; (b) Phase portrait for $\chi = 0.10 \in (\chi_1^\star, \chi_2^\star)$; (c) Phase portrait for $\chi = 1 > \chi_2^\star$; (d) Transient time response for zero initial conditions IC#1 for $\chi = -1$; (e) Transient time response for $\chi = 0.10$ and initial conditions IC#2; (f) Transient time response for $\chi = 0.10$ and initial conditions IC#3. Note that the initial amplitudes p_0 are the same for IC#2 and IC#3, but the different initial phases Φ_0 result in different steady state outcomes.

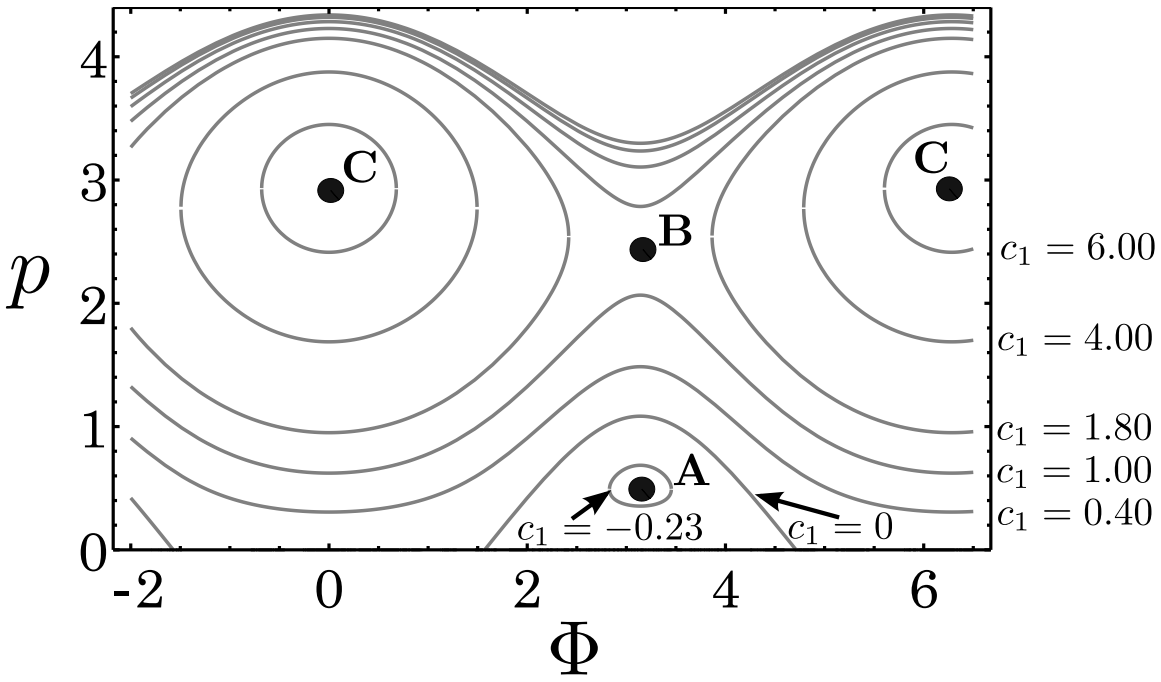

Figure 3.3: Phase plane plotted using level curves of equation (3.12) by varying c_1, for $\chi = 0.066$ and $D = 0$.

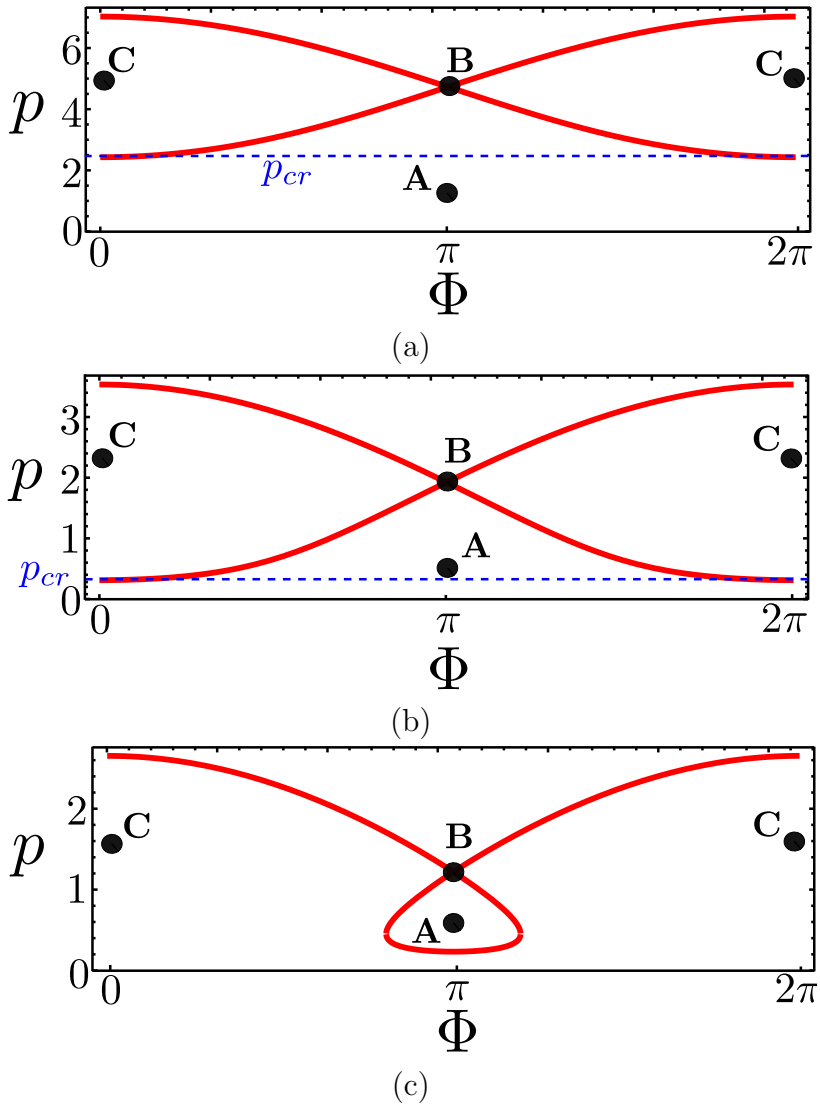

Figure 3.4: Stable and unstable manifolds of **B** for three values of χ. (a) $\chi = 0.02$; (b) $\chi = 0.10$; (c) $\chi = 0.20$. Figure 3.4 (a) and (b) show lines of constant amplitude p_{cr}, which indicate the maximum amplitude of initial conditions p_0 such that the response will approach the lower branch for all values of the initial phase Φ_0. The topology of the homoclinic orbit about **A** changes from Fig. 3.4 (a),(b) to that of Fig. 3.4 (c) for $\chi > 4/27$. It is seen that for $\chi \in (4/27, 8/27)$, small amplitude initial conditions will result in a large amplitude steady state **C**, for all initial phases.

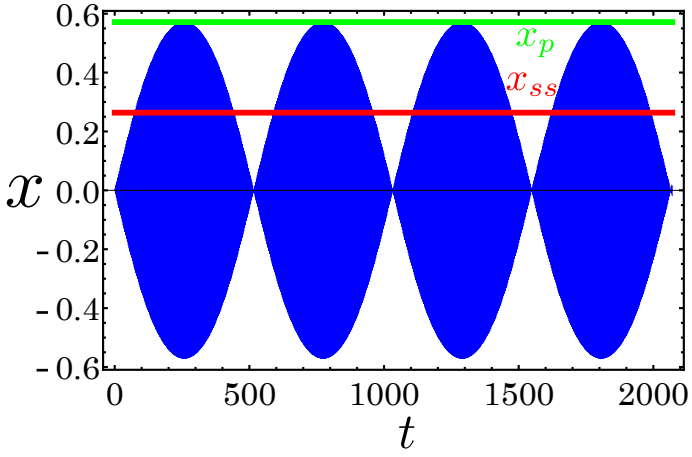

(a)

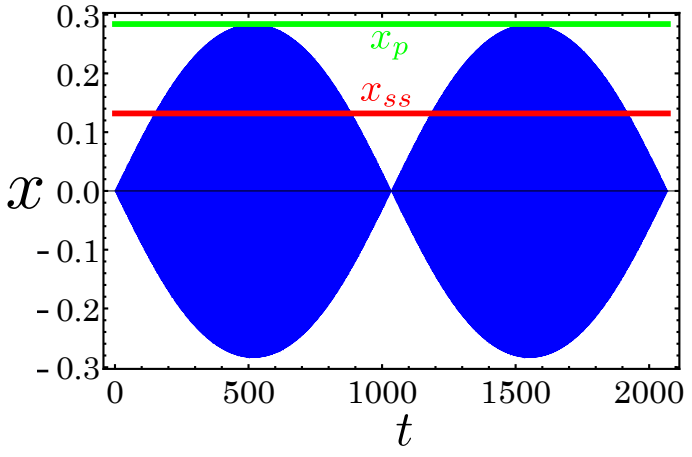

(b)

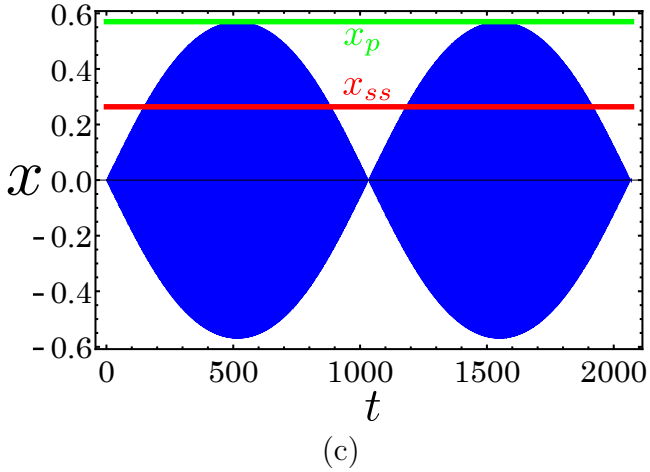

(c)

Figure 3.5: Numerical simulations of equation (3.1) for $\epsilon = 0.03$ and $\omega = 2$, and three sets of system parameter values that yield $\chi = 0.094$, with a predicted overshoot of 115.8%. (a) $F = 1/2$, $\sigma = 2$, $\xi = 2$, simulated percent overshoot = 116.6%; (b) $F = 0.125$, $\sigma = -1$, $\xi = -4$, simulated percent overshoot = 115.3%; (c) $F = 0.177$, $\sigma = 1$, $\xi = 1$, simulated percent overshoot = 116.1%.

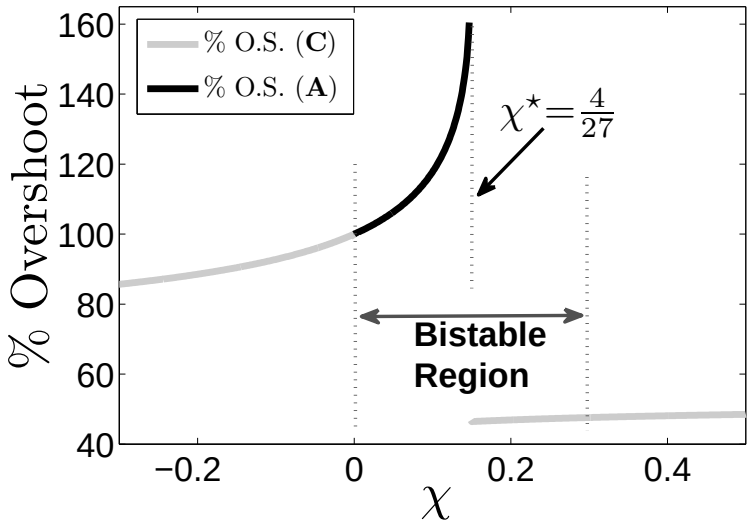

(a)

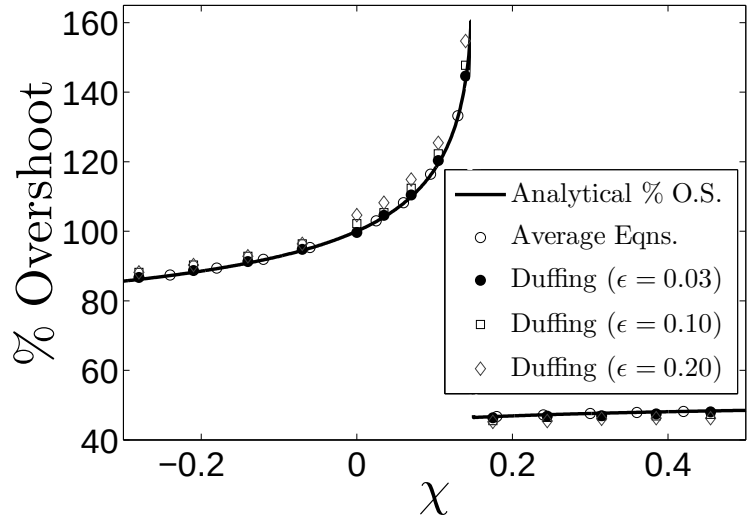

(b)

Figure 3.6: (a) The analytical results for percent overshoot versus χ for zero initial conditions. The percent overshoot is computed relative to either the upper branch **C**, shown by the solid gray curves, or the lower branch equilibria **A**, shown by the solid black curve, depending on χ, as indicated in the inset. At $\chi = 4/27$, zero initial conditions results in a trajectory on the stable manifold of **B**. When $\chi < 0$ or $\chi > 4/27$, zero initial conditions results in transient trajectories about equilibria **C**, as shown in Fig. 3.4 (c). Note that the phase at which equation (F.2) is evaluated to obtain p_{max} for the percent overshoot is different for $\chi < 0$ and $\chi > 4/27$, as described in Section 3.3.1. (b) Comparison of the analytical solution and simulations of both the Duffing oscillator (equation (3.1)) and the averaged equations (equations (3.6) and (3.7)) for the case of zero initial conditions and different values of ϵ. The parameter values used in the simulations include: $F = 1/2$, $\sigma = 1.75$, $\omega = 2$. The nonlinearity ξ is varied from -4 to 7 to sweep the χ domain shown, and it is noted that the percent overshoot is asymptotic to 58.74% as $\chi \to \pm\infty$ (i.e., as one approaches resonance, $\sigma \to 0$).

Chapter 4

Transient Dynamics of a Single CPVA System, Theory

4.1 Introduction

In the present chapter we focus on the transient response characteristics of a single absorber fitted to a rotor that is subjected to engine-order torsional excitation. Absorbers with a wide range of paths, including both circular and tautochronic (neither hardening nor softening out to large amplitudes [11,68,70]), the most common types used in practice, are considered. The results obtained are also applicable to the synchronous response of systems with multiple identical absorbers. We derive an approximate analytical method for predicting the percent overshoot of an absorber during startup, such as occurs during cylinder deactivation, which leads to a nonlinear beating type of absorber response in the transition to steady-state. The model is quite general and provides a relatively simple method for predicting the overshoot when the absorber has zero damping and starts with zero initial conditions. The results

are found to accurately predict the transient overshoot observed in simulations of the full nonlinear equations of motion (EOM) when damping is small (as is the case in practice). Furthermore, we show in Chapter 5 that these overshoot results provide a useful upper bound for transient absorber response, which is useful for design purposes.

The results are obtained by first deriving the full nonlinear EOM for a single absorber system and then scaling the equations in two ways that allow for the application of perturbation methods. The method of averaging yields equations that govern the slowly varying amplitude and phase of the absorber response envelope. These equations have been used in previous studies of steady-state response, and are used here to predict the transient absorber amplitude response for a range of practical absorber paths. The prediction is based on properties of the conservative slow-flow equations for zero absorber damping. Using the scaling introduced in Chapter 3, these equations are rescaled to combine the excitation amplitude, the difference in absorber and excitation frequencies, and the absorber path nonlinearity, into a single system parameter that dictates the response. For absorber paths not near-tautochronic, e.g., circles and cycloids, the problem reduces to the transient response of a simple Duffing oscillator, which was the subject of Chapter 3. The approximate results obtained are shown to provide accurate predictions for the full EOM for a wide range of system parameters and operating conditions. The results for undamped absorbers are expressed in terms of either one or two nondimensional parameters, depending on the path type, while the results for systems with damping require the simulation of the averaged equations, and involve one more parameter.

4.2 System Modeling

The dynamic model for the CPVA system is based on the schematic shown in Fig. 4.1, which is sufficiently general to describe the two experimental absorber systems described in Chapter 5. The pendulum absorber is modeled as a point-mass m located at the pendulum center of mass (COM), which moves along a prescribed path on a rotor of inertia J that is subjected to a harmonic, engine-order torque excitation. This system has two degrees of freedom, described by the absorber arc-length S and the rotor/crank angle θ. Note that absorber arc-length is used, as opposed to angular position, since it is more accommodating to non-circular paths; see Fig. 4.1. A small scaling parameter, defined to be the ratio of absorber to rotor rotational inertia, $\epsilon = mc^2/J$, is used throughout this work in order to scale small nondimensional parameters, which include damping, applied torques, and absorber inertia; these assumptions are entirely consistent with parameters encountered in practical applications.

We begin by deriving the non-dimensional EOM for the CPVA system model shown in Fig. 4.1. Using a two-parameter formulation for the path along which the absorber rides relative to the rotor [17], the EOM can accommodate a family of paths such as those shown in Fig. 4.1. The equations are scaled using ϵ in order to capture the leading order effects of nonlinearity, damping, applied torque, and absorber-to-rotor coupling. Two different parameter scalings are used, depending on the absorber path type, since for near-tautochronic absorbers the path nonlinearity is essentially zero. The averaged equations for these two types of systems, with zero damping, are then used to determine a constant of motion governing the transient response, from which one can predict the percent overshoot. The physical assumptions used in obtaining both the full non-linear EOM, as well as the subsequent reduced

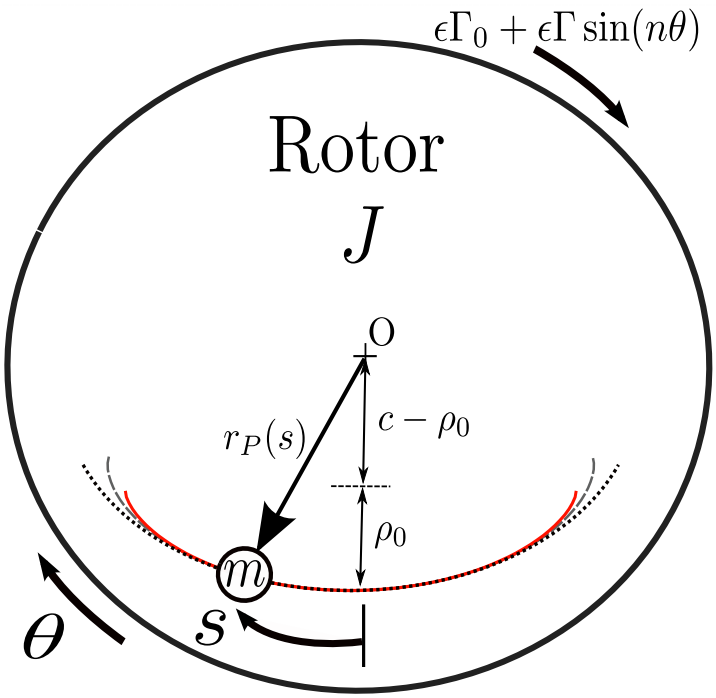

Figure 4.1: Depiction of the CPVA system model showing three possible paths for the absorber COM. The outermost (circular) and innermost (cycloidal) paths bound the two-parameter family under consideration; the middle path corresponds to the tautochrone. The paths are shown enlarged, and not to scale relative to the rotor, to exaggerate the differences in the paths.

set of approximate equations include: (1) a rigid rotor; (2) small viscous damping in the absorber, $\epsilon\mu << 1$ and rotor $\epsilon\mu_0 << 1$; (3) single order harmonic torque, $\epsilon\Gamma\sin(n\theta)$; (4) the rotor spins at a nearly constant speed, $\dot{\theta} \approx \Omega$; (5) small inertia ratio, $\epsilon = \frac{mc^2}{J} << 1$; (6) applied torque is small (compared to the system kinetic energy), $\epsilon\Gamma << 1$, $\epsilon\Gamma_0 << 1$; and (7) the independent variable employed is the rotor angle θ rather than time t. For convenience, these assumptions will be referred to by their respective numbers in the model development.

4.2.1 Equations of Motion

Only a brief summary of the derivation of the EOM for the system is presented here, since this has been previously described in the literature, and these equations are similar to those derived in Chapter 2[1]. The absorber coordinate S and rotor speed $\dot{\theta}$ are non-dimensionalized using, respectively, the distance c from rotor center to absorber path vertex, $s = S/c$, and the mean rotor speed Ω, $\nu = \dot{\theta}/\Omega$. Also, the independent variable is switched from time t to θ, in order convert the fluctuating torque $T_n \sin(n\theta)$ from a nonlinear term into a type of non-autonomous term, which facilitates the perturbation analysis. The resulting non-dimensional EOM for the absorber (s) and the rotor (ν) are,

$$\beta\nu s'' + \Big(g(s) + \alpha + \beta s'\Big)\nu' - \frac{1}{2}\frac{dr_P^2(s)}{ds}\nu = -\epsilon\beta\mu s', \tag{4.1}$$

$$\begin{aligned}\nu\nu' + \epsilon\Bigg(\Big(g(s) + \alpha\Big)(\nu\nu' s' + \nu^2 s'') + \frac{dg(s)}{ds}\nu^2 s'^2 + \\ + \frac{dr_P^2(s)}{ds}\nu^2 s' + \nu\nu' r_P^2(s) + \mu_0\nu - \Gamma_0 - \Gamma\sin(n\theta)\Bigg) = 0,\end{aligned} \tag{4.2}$$

where $r_P(s)$ is the radial distance from the center of the rotor to the absorber's COM, $\epsilon\mu$ is the coefficient of absorber viscous damping, $\epsilon\mu_0$ is the viscous damping coefficient in the rotor bearing, $\epsilon\Gamma_0$ is the magnitude of the mean torque applied to the rotor, $\epsilon\Gamma$ is the magnitude of the fluctuating torque applied to the rotor, n is the excitation order, and the function $g(s) = \sqrt{r_P^2(s) - (dr_P^2/ds)^2/4}$ is a path dependent function, specifically, it is the cosine of the angle between the local tangent to the path and a line normal to a radial line passing

[1]The rollers are neglected in this derivation and pendulum-type absorbers are accommodated in addition to the bifilar configuration.

through the rotor center and the path vertex. Coefficients β and α are additional rotational inertia terms related to the absorber geometry; these arise because the circular path absorbers can be implemented as compound pendulums with a single point pivot suspension, in which case their rotational inertia contributes to the absorber inertia. More common absorber implementations use a bifilar (two point) suspension which constrains the absorber body such that it only translates relative to the rotor. In the bifilar case, the point mass model suffices, with the absorber rotational inertia bundled in with that of the rotor, J. The bifilar suspension is able to easily accommodate both circular or non-circular absorber paths. For example, a circular path absorber with a bifilar suspension has $\alpha = 0$ and $\beta = 1$, whereas a circular path absorber with a single point suspension has $\alpha = r^2/(c\rho_0)$ and $\beta = 1 + (r/\rho_0)^2$, where r is the radius of gyration of the pendulum about its center of mass [53], c is the distance from the absorber path vertex to the center of rotation of the rotor (see Fig. 4.1) , and ρ_0 is the initial radius of curvature of the absorber path at its vertex (see Fig. 4.1).

Clearly, the absorber and rotor responses are coupled. A perturbation study of the system response is made convenient by uncoupling these EOM to leading order in ϵ using some approximations. The uncoupling is accomplished by using assumptions (4)-(6), as follows. Briefly, the applied fluctuating torque Γ induces small speed fluctuations about the constant non-dimensional rotor speed, described by $\nu = 1 + \epsilon w(\theta)$. After substituting this into equations (4.1) and (4.2) and expanding in ϵ, the rotor acceleration w', expressed in expanded form, can be substituted into the absorber equation, which results in an oscillator-type equation governing the response of the absorber [49, 50]. This equation, which includes the nonlinear effects arising from the specified absorber path $r_P(s)$, as well as the effects of

the rotor acceleration, is given by,

$$s'' - \frac{1}{2\beta}\frac{dr_P^2(s)}{ds} = \epsilon F(s, s', s'', \theta) + \mathcal{O}(\epsilon^2). \tag{4.3}$$

where

$$F(s, s', s'', \theta) = -\mu s' - \Big((g(s) + \alpha)/\beta + s'\Big)\Bigg(\Gamma \sin(n\theta) - \Big(\Big(g(s) + \alpha\Big)s'' + \frac{dg(s)}{ds}s'^2 + \frac{dr_P^2(s)}{ds}s'\Big)\Bigg).$$

Note that the mean torque Γ_0 and the rotor bearing resistance $\mu_0\nu$ fall to higher order when one assumes that they balance to order ϵ, i.e., $\mu_0\nu - \Gamma_0 = \mathcal{O}(\epsilon)$. The next section describes the absorber COM path formulation and how it affects the absorber response.

4.2.2 The Absorber Path

The path followed by the absorber COM determines the form of its effective restoring force, specifically, by the component of the centrifugal load that is tangent to the absorber path. In the absorber oscillator equation (4.3), this is described by the term $dr_P^2(s)/ds$. Here we employ a two parameter family of paths, introduced by Denman [17], ranging from circles to cycloids, that are described by the linear tuning order $\tilde{n}$ and a nonlinear tuning parameter λ. Specifically, the local radius of curvature on the absorber path, normalized by c, is given by $\rho = \sqrt{\rho_0^2 - \lambda^2 s^2}$ where $\rho_0 = 1/(1 + \tilde{n}^2)$ is the value at the vertex, which sets the linear tuning. This family of paths consists of epicycloids for $\lambda \in (0, 1)$, with limiting cases of a circle for $\lambda = 0$ and a cycloid for $\lambda = 1$ [17]. In this formulation the absorber restoring force

can be written, in an expanded form, as

$$\frac{dr_P^2(s)}{ds} = -2\beta\tilde{n}^2 s + (\lambda_e^2 - \lambda^2)\left(\frac{1}{3}(1+\beta\tilde{n}^2)^3 s^3 + \mathcal{O}(s^5)\right). \tag{4.4}$$

As seen in equation (4.4), $\tilde{n}$ (with β) sets the small amplitude, linear, free vibration natural frequency of the absorber. This linear tuning is a function of the absorber geometry, as described above and shown in Fig. 4.1. The parameter λ sets the large amplitude, nonlinear, free vibration response, which can be softening ($\lambda < \lambda_e$), hardening ($\lambda > \lambda_e$), or neutral ($\lambda = \lambda_e$), where $\lambda_e = \beta\tilde{n}/\sqrt{\beta\tilde{n}^2+1}$ is a special value that results in a purely linear restoring force, even at large amplitudes, thus realizing the *tautochronic* path [49, 50].

The middle absorber path shown in Fig. 4.1 is tautochronic, while the outermost and innermost paths shown in Fig. 4.1 are circular ($\lambda = 0$) and cycloidal ($\lambda = 1$), respectively. It is important to note that a CPVA system with a tautochronic path is nonlinear, due to the inertial coupling to the rotor, described by terms of order ϵ in equation (4.3). As described below, for analysis by perturbations, the absorber amplitudes for paths that are nearly tautochronic must be scaled differently than those for other paths in this family, in order to introduce the dominant nonlinearity at leading order. Therefore, these scalings aren't specific for perturbation studies of an exact circular or an exact tautochronic path absorber, but rather, they provide a good approximation of the response for all paths in the prescribed family, specifically, for all epicycloids with $\lambda \in (0, 1)$. The tautochronic path perturbation results are valid for all feasible absorber amplitudes and capture the essential dynamics for paths that are nearly tautochronic, that is, with $\lambda \approx \lambda_e$; here the dominant nonlinear effects arise from kinematic coupling with the rotor. The general path perturbation results capture the essential dynamics for all paths that are not nearly tautochronic, although their scaling

limits the results to moderate amplitudes; for these paths the dominant nonlinear effects arise from the absorber path. These scalings are referred to herein, respectively, as *near-tautochronic path* scaling and *general path* scaling. The approximate equations obtained for these cases have a similar structure, as described below. For zero absorber damping, the general path problem formulation can be expressed in terms of a single parameter, χ. The near-tautochronic path problem can be expressed in terms of χ and an additional parameter, γ, where the near-tautochronic results approach the general path results in the limit $\gamma \to 0$.

4.2.3 Scaling and Asymptotic Analysis

Here we describe the scalings used for general path and near-tautochronic path absorbers. The equations are scaled in such a way to extract to leading order the effects of damping, forcing, detuning from resonance, and nonlinearities. The method of averaging is employed to obtain a set of first-order differential equations governing the slowly varying amplitude and phase of the absorber response. The derivations are only summarized here, since these averaged equations and their steady-state responses have been investigated elsewhere for both general paths [5, 26, 52, 53] and near-tautochronic paths [11, 14, 68, 70]. Here we focus on an additional scaling of the previously studied averaged equations which further reduces the number of system parameters, thus simplifying the transient analysis, and providing a framework that describes the averaged equations for all paths in a unified manner.

To extract the desired effects at order ϵ, one substitutes equation (4.4) into equation (4.3) and employs the scalings shown in Tab. 4.1 for the two types of paths, where the subscript c is used for terms in the general path scaling (c stands for circular, since that is the most common of these paths) and the subscript t is used for terms in the near-tautochronic path scaling.

The essential difference in these scalings is that the absorber amplitude must be scaled for the general path in order to capture the cubic path nonlinearity to order ϵ. In contrast, for near-tautochronic paths the absorber response is nearly linear out to large amplitudes, and thus the amplitude does not need to be scaled. Here we introduce a parameter κ to allow the path to deviate slightly from exact tautochronicity. In all cases the absorber is tuned such that it addresses the order n excitation, and thus we introduce the (small) detuning parameters σ_i $(i = c, t)$, which describe the difference between n and $\tilde{n}$, as employed in the averaging process. Explicit expressions for the σ_i are found below in equations (4.13) and (4.15). As shown in Tab. 4.1, the general path case requires an adjustment to the scaling of the torque so it will be retained at order ϵ. Finally, for the case of a compound pendulum circular path absorber, the torque scaling also involves absorber geometry and inertia terms β and α.

Table 4.1: Parameter scalings for general and near-tautochronic paths.

Type of Path	**General Path**	**Near Tautochronic**
Amplitude	$s = \sqrt{\epsilon} r_C$	$s = r_t$
Path	λ	$\lambda = \lambda_e + \epsilon\kappa$
Torque	$\Gamma = \sqrt{\epsilon}\Gamma_C \beta/(1+\alpha)$	$\Gamma = \Gamma_t$
Damping	μ	μ

Expanding the absorber equations in ϵ and retaining order ϵ terms yields an absorber oscillator equation with weak damping, forcing, and nonlinearity, in the following universal form

$$r_i'' + \tilde{n}^2 r_i = \epsilon f_i(r_i, r_i', \theta) + \mathcal{O}(\epsilon^2), \tag{4.5}$$

where subscript $i = c, t$ indicates the path type, and the expressions for $f_i(r_i, r_i', \theta)$ are given by

$$f_C(r_C, r_C', \theta) = -\xi_C r_C^3 - \Gamma_C \sin(n\theta) - \mu r_C' + \frac{(1+\alpha)^2}{\beta} r_C'', \tag{4.6}$$

for the general path, where ξ_C is the effective path nonlinearity coefficient given explicitly below in equation (4.14). For the near-tautochronic path scaling,

$$\begin{aligned} f_t(r_t, r_t', \theta) \quad &= -\mu r_t' - \frac{\kappa}{3}\tilde{n}(1+\tilde{n}^2)^{5/2} r_t^3 + \\ &-[r_t' + g_0(r_t)]\bigg(\Gamma_t \sin(n\theta) + 2\tilde{n}^2 r_t' r_t - \frac{\partial g_0(r_t)}{\partial r_t} r_t'^2 - g_0(r_t) r_t''\bigg), \end{aligned} \tag{4.7}$$

where $g_0(r_t) = \sqrt{1-\tilde{n}^2(1+\tilde{n}^2)r_t^2}$ is the leading order part of $g(s)$, that is, its $\epsilon = 0$ version[2]. The perturbation function $f_i(r_i, r_i', \theta)$ and its subsequent averaged form are well known for both the general path and the near-tautochronic path systems [5, 11, 14, 26, 52, 53, 68, 70]. Here we make a small adjustment to the previous approach, before averaging, which involves extracting the linear detuning term $\epsilon r_i''$ from the right hand side of equations (4.6) and (4.7) and rewriting equation (4.8) as

$$r_i'' + \hat{n}^2 r_i = \hat{\epsilon} f_i(r_i, r_i', \theta) + \mathcal{O}(\hat{\epsilon}^2), \tag{4.8}$$

where $\hat{n} = \tilde{n}/\sqrt{1-\Lambda\epsilon}$, $\hat{\epsilon} = \epsilon/(1-\Lambda\epsilon)$, $\Lambda = (1+\alpha)^2/\beta$, and we employ averaging on this form of the oscillator. For averaging, one makes the assumption of a nearly harmonic response at the forcing frequency via the coordinate transformation $[r_i, r_i'] = [z_i(\theta_i)\sin(n\theta_i + \psi_i(\theta_i)), z_i(\theta_i) n \cos(n\theta_i + \psi_i(\theta_i))]$, and averages over one period of the forcing, $2\pi/n$. This results in two first order differential equations governing the slowly varying amplitude a_i and phase ϕ_i, where (a_i, ϕ_i) are the averages of (z_i, ψ_i) over one period. For brevity, these

[2]The near tautochronic perturbation function $f_t(r_t, r_t', \theta)$ is the same as that obtained in equation (2.17) of Chapter 2, except, the rollers are neglected here and the path derivative $\partial y_P/\partial s$ is expanded in amplitude to extract up to the cubic Duffing nonlinearity term $(1/3)\kappa\tilde{n}(1+\tilde{n}^2)^{5/2} r_t^3$.

averaged equations are not presented explicitly here, but a scaled version of them is shown next, and the interested reader can find intermediate results in the papers cited above.

One can significantly simplify the analysis of the averaged equations by scaling the absorber amplitude a_i and independent variable (the rotor angle) θ_i by the system parameters in the following way [48],

$$\theta_i = \left(\frac{4n}{\hat{\epsilon}\sigma_i}\right)\Theta_i, \quad a_i = -2\left(\frac{\Gamma_i}{\sigma_i}\right)p_i, \tag{4.9}$$

for $\sigma_i \neq 0$. This scaling results in the following averaged equations that are valid for both classes of paths,

$$\frac{dp_i}{d\Theta_i} = -\sin(\phi_i)F_1^i(p_i) - D_i p_i \tag{4.10}$$

$$p_i\frac{d\phi_i}{d\Theta_i} = 4\chi_i p_i^3 - \cos(\phi_i)F_2^i(p_i) - 2p_i, \tag{4.11}$$

where

$$\chi_i = \frac{3}{2}\xi_i\left(\frac{\Gamma_i^2}{\sigma_i^3}\right), \quad D_i = 2\left(\frac{n\mu}{\sigma_i}\right), \tag{4.12}$$

and σ_i and ξ_i are the detuning and the effective path nonlinearity of the respective oscillators, respectively, which are given by

$$\sigma_C = \frac{n^2 - \tilde{n}^2}{\epsilon} - \frac{(1+\alpha)^2}{\beta}\tilde{n}^2, \tag{4.13}$$

$$\xi_C = \frac{1}{6\beta}\big(1+\beta\tilde{n}^2\big)^2\big(\lambda^2 + (\lambda^2-1)\beta\tilde{n}^2\big), \tag{4.14}$$

for the general path, and

$$\sigma_t = \frac{n^2 - \tilde{n}^2}{\epsilon} - \tilde{n}^2, \tag{4.15}$$

$$\xi_t = \tilde{n}^2\big(n^2(1+\tilde{n}^2/3) - \tilde{n}^2(1+\tilde{n}^2)\big) + \\ + \frac{\kappa}{3}\tilde{n}\sqrt{1+\tilde{n}^2}\big(1+\tilde{n}^2(2+\tilde{n}^2)\big), \tag{4.16}$$

for the near-tautochronic path. The functions F_1^i and F_2^i are a primary difference in the equations for the two types of paths. For general paths, $F_1^c = F_2^c = 1$ and one recovers a scaled version of the well-known averaged Duffing equation for the case of weak nonlinearity, damping, and forcing near resonance which is investigated in Chapter 3. For near-tautochronic paths $F_1^t(p_t)$ and $F_2^t(p_t)$ are based on elliptic functions and are given by

$$F_1^t = \frac{4}{3\pi}\left(\left(\frac{1}{\gamma p_t^2} + 1\right)E_E(\gamma p_t^2) + \left(1 - \frac{1}{\gamma p_t^2}\right)E_K(\gamma p_t^2)\right), \tag{4.17}$$

$$F_2^t = \frac{4}{3\pi}\left(\left(2 - \frac{1}{\gamma p_t^2}\right)E_E(\gamma p_t^2) + \left(\frac{1}{\gamma p_t^2} - 1\right)E_K(\gamma p_t^2)\right), \tag{4.18}$$

where

$$\gamma = \frac{4\tilde{n}^2(1+\tilde{n}^2)\Gamma_t^2}{\sigma_t^2} \tag{4.19}$$

is the additional parameter introduced by the near-tautochronic scaling, and in the limit $\gamma \to 0$, $F_1^t, F_2^t \to 1$. The functions $E_K(\gamma p_t^2)$ and $E_E(\gamma p_t^2)$ are the complete elliptic integrals of the first and second kind, which depend on the absorber amplitude p_t and the parameter γ. These terms arise since the rotor acceleration has a diminished effect on how it drives the absorber at large amplitudes along the path, thus providing an amplitude-dependent effective

forcing. In fact, parameter γ describes an effective hardening of the system response, in the sense that the excitation has a reduced effect at large amplitudes, as described in more detail below. For the general path case, the path nonlinearity dominates these effects, which are scaled out by the amplitude expansion.

The scaling given in equation (4.9) reduces the parameter dependence of the averaged equations from four parameters (ξ_i, Γ_i, σ_i, μ) to two parameters (χ_c, D_c) for the general path and to three parameters (χ_t, D_t, γ) for the near-tautochronic path. For the undamped system $D_i = 0$, the general path averaged equations depend on a single parameter χ_c, making it particularly attractive for analysis.

In order to compute the percent overshoot of the absorber transient response, the steady-state response is needed. The steady-state response amplitude $\bar{p}_i$ can be computed from equations (4.10) and (4.11) by setting $dp_i/d\tau_i = d\phi_i/d\tau_i = 0$ and using $\sin^2(\phi_i)+\cos^2(\phi_i) = 1$, which results in the following implicit expression for $\bar{p}_i$,

$$\left(\frac{D_i\bar{p}_i}{F_1^i(p_i)}\right)^2+\left(\frac{4\chi_i\bar{p}_i^3-2\bar{p}_i}{F_2^i(p_i)}\right)^2=1. \tag{4.20}$$

For the general path, equation (4.20) is a cubic in $\bar{p}_c^2$ and can be solved explicitly [48]. For the near-tautochronic paths, $\bar{p}_t$ is numerically obtained, due to the elliptic functions F_1^t and F_2^t.

4.3 Analytical Predictions of Transient Amplitudes

The percent overshoot of a system is defined as

$$P.O. = \left(\frac{p_{max} - \bar{p}}{\bar{p}} \right) \times 100, \tag{4.21}$$

where p_{max} is the peak amplitude achieved during the transient response and $\bar{p}$ is the steady-state amplitude. For this system the transient is a beating type of motion, composed roughly of harmonic components at orders n and $\tilde{n}$, with the latter shifted by amplitude-dependent nonlinear effects. For a linear system this overshoot can be computed exactly [28, 69]. For the undamped nonlinear system the overshoot can be computed by using a constant of motion for the averaged equations, providing a useful bound for systems with weak damping. With this constant of motion, and the previous steady-state amplitude results, the percent overshoot approximation can be constructed for both path types. This approach will be referred to as the pseudo-energy method. In the present study we focus on the case of zero initial conditions, since it is a close approximation to the absorber response in variable displacement automotive engines when cylinders deactivate. However, the results easily generalize to arbitrary initial conditions. In this section, we show results for the zero initial condition overshoot problem using the pseudo-energy method. In the following section we investigate the accuracy of the method by comparing it with simulations of the full EOM. We also provide a comment on how the form of the input torque during cylinder deactivation transition can effect absorber overshoot.

4.3.1 The Pseudo Energy Method

For zero absorber damping ($D_i = 0$), one combines equations (4.10) and (4.11) to obtain an exact first order differential equation,

$$\frac{dp_i}{d\phi_i} = \frac{-p_i \sin(\phi_i) F_1^i(p_i) - D_i p_i^2}{4\chi_i p_i^3 - \cos(\phi_i) F_2^i(p_i) - 2p_i}. \tag{4.22}$$

which is integrated, resulting in the following constant of motion,

$$-\chi_i p_i^4 + p_i^2 + G_i(p_i)\cos(\phi_i) = c_1, \tag{4.23}$$

where $G_c(p_c) = p_c$, $G_t(p_t) = p_t F_1^t(p_t)$, and c_1 is the constant of integration. Note that for the general path this is a quartic (cubic) equation for $c_1 \neq 0$ ($c_1 = 0$), and for nearly tautochronic paths the equation involves elliptic functions. Equation (4.23) allows one to simply construct the phase portrait for the undamped averaged system in the usual way. A thorough study of transient responses and overshoot using equation (4.23) for the general path case, that is, for Duffing's equation, is given in Chapter 3. Here we describe only those results needed to compute the percent overshoot subject to zero initial conditions, that is, for $c_1 = 0$.

Only those absorber responses that reduce torsional vibrations are of interest, and for the undamped system these satisfy $\phi_i = \pi$, such that the absorber response is exactly out of phase with the excitation. To obtain this response, and also avoid undesirable non-synchronous responses [68], one over-tunes the absorbers by making $\tilde{n} > n$ ($\sigma_i < 0$) with $|\tilde{n} - n| << 1$, which results in torsional vibration reduction. For hardening absorber systems, $\xi_i > 0$ ($\chi_i < 0$), the over-tuned system will have only a single order n steady-state response,

which is described by a stable equilibrium of the averaged equations [48]. On the other hand, for softening absorber systems ($\xi_i < 0$), for $0 < \chi_i < \chi_i^\star$ the over-tuned system is bi-stable and the lower amplitude steady-state equilibrium is the one that results in the desired response with $\phi_i = \pi$. At $\chi_i^\star$, the initial conditions (p_{i0}, ϕ_{i0}) result in a trajectory that lies on the stable manifold of the saddle point, and for $\chi_i > \chi_i^\star$ the system transitions to the upper branch steady-state response which is in phase with the excitation, $\phi_i = 0$, resulting in vibration amplification. The jump parameter value, $\chi_i^\star$, is further described below.

A sample response with zero initial conditions that leads to the desired response using the general path scaling is shown in the phase space (p_C, ϕ_C) in Fig. 4.2 (a), and its equivalent $s(\theta)$ response is shown in Fig. 4.2 (b); this is for a damped system with parameters $\chi_C = 0.10$, $\xi_C < 0$, and $D_C = 0.30$. Note that $p(\Theta)$, obtained from simulating the averaged equations, accurately captures the envelope of the beating behavior of $s(\theta)$. The transient response of a system with a hardening path is identical to that in Fig. 4.2 (a) & (b), except that the trajectory labeled as coming from the saddle point would come in from infinity, since the saddle doesn't exist for $\chi_i < 0$. For undamped systems, the beating response continues indefinitely (it is motion on a torus), and the averaged equation response will follow a closed curve around the target steady-state equilibrium. For small damping, the peak amplitude should be well approximated by the undamped value, unless the beat period is long compared to the envelope settling time. Using the pseudo-energy method, a closed form result for the percent overshoot of general path absorbers is possible because both the steady-state amplitude (equation (4.20)) and the peak transient amplitude (equation (4.23)) can be solved exactly. In fact, because of the parameter scaling employed, this result depends on the single parameter χ_C [48]. For near-tautochronic paths, a closed form expression is not available,

due to the presence of elliptic functions, but the percent overshoot can be computed in a straightforward manner using numerical root-finding techniques.

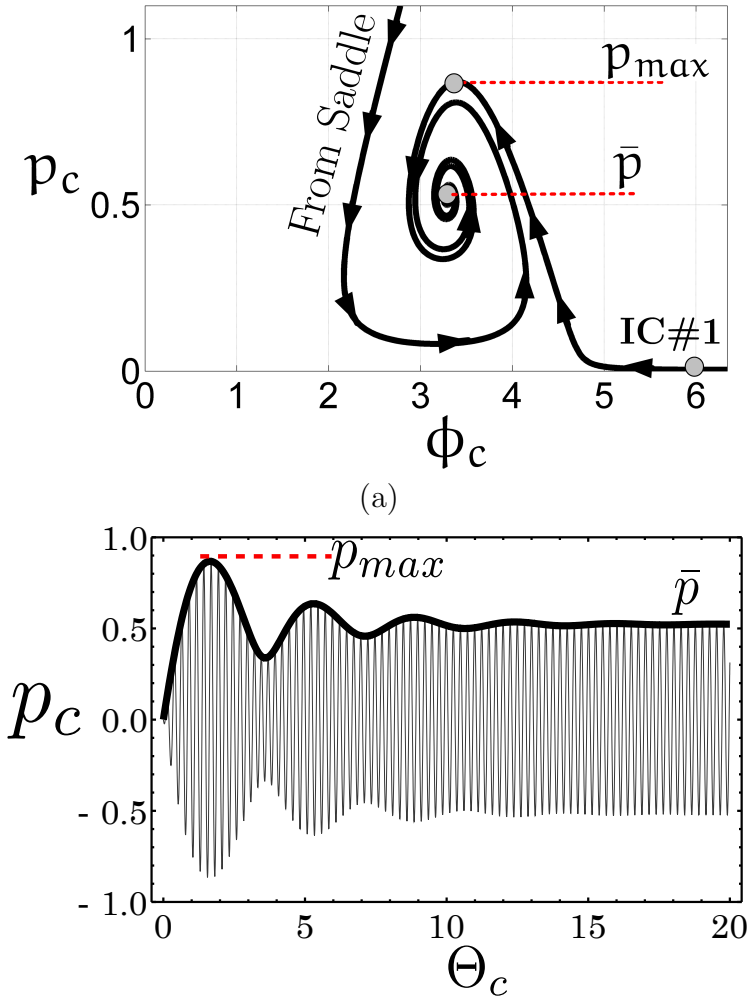

Figure 4.2: A damped zero initial condition transient trajectory, IC #1, obtained from simulations of the general path averaged equations, indicating the peak and steady-state amplitudes; (a) shown in the phase space, and (b) as the absorber response versus θ. System parameter values: $D_C = 0.30$ and $\chi_C = 0.10$. Also shown in (a) is the trajectory from the unstable manifold of the saddle that tends toward the desired steady state.

To demonstrate the utility of the general path scaling, shown in Fig. 4.3 (a)-(c) is the transient absorber response obtained from simulations of the full EOM for three undamped ($\mu = 0$) systems using an inertia ratio of $\epsilon = 0.03$, excitation order $n = 1.5$ and three

different sets of system parameters $\tilde{n}$, λ, and Γ, as indicated in the caption. These five system parameters specify the averaged system parameters σ_C, ξ_C, and Γ_C. For all three systems $\chi_C = 0.112$, for which the pseudo-energy method gives an overshoot prediction of 122%, and all three simulated system overshoots are very near the predicted value. Note that the differences in system parameters result in differences in the amplitude scales and the transient beat frequencies, but the percent overshoot is essentially identical in all three cases. Lastly, we note that the two noncircular path cases ($\lambda = 0.1$ and 0.2) are not typical for applications, but serve the purpose of demonstrating the accuracy of the prediction in its most sensitive regime, which is the softening range of $\chi_C > 0$, as shown in Fig. 4.4 (a).

The percent overshoot for zero initial conditions computed using the pseudo-energy method for $D = 0$ and the averaged equations for $D \neq 0$ for both general path and near-tautochronic path absorbers are shown in Fig. 4.4 (a) & (b), respectively. These figures depict how the parameters χ_i, γ, and D_i affect the overshoot for the two types of paths. For an over-tuned absorber ($\sigma_i < 0$), the overshoot for absorbers with hardening paths occurs for $\chi_i < 0$ and with softening paths it occurs for $\chi_i > 0$. Note that the general path scaling captures the zero initial condition overshoot of an undamped linear system ($\xi_C = 0$ and $\chi_C = 0$), which is 100%, and the absorber path in this case is the tautochrone, $\lambda = \lambda_e$. On the other hand, due to the different parameter definitions, for the near-tautochronic scaling, $\lambda = \lambda_e$ corresponds to $\kappa = 0$ and makes ξ_t small and negative, that is, nonzero, in a manner that depends on n and $\tilde{n}$ (see equation (4.16)). And, although ξ_t is softening for the tautochronic path, the parameter γ results in a hardening effect, as shown in Fig. 4.4 (b), and thus these effects compete in a manner that depends on the system parameters Γ_t and σ_t (see equation (4.19)). One interpretation of Fig. 4.4 (a) & (b) is, that for a fixed tuning

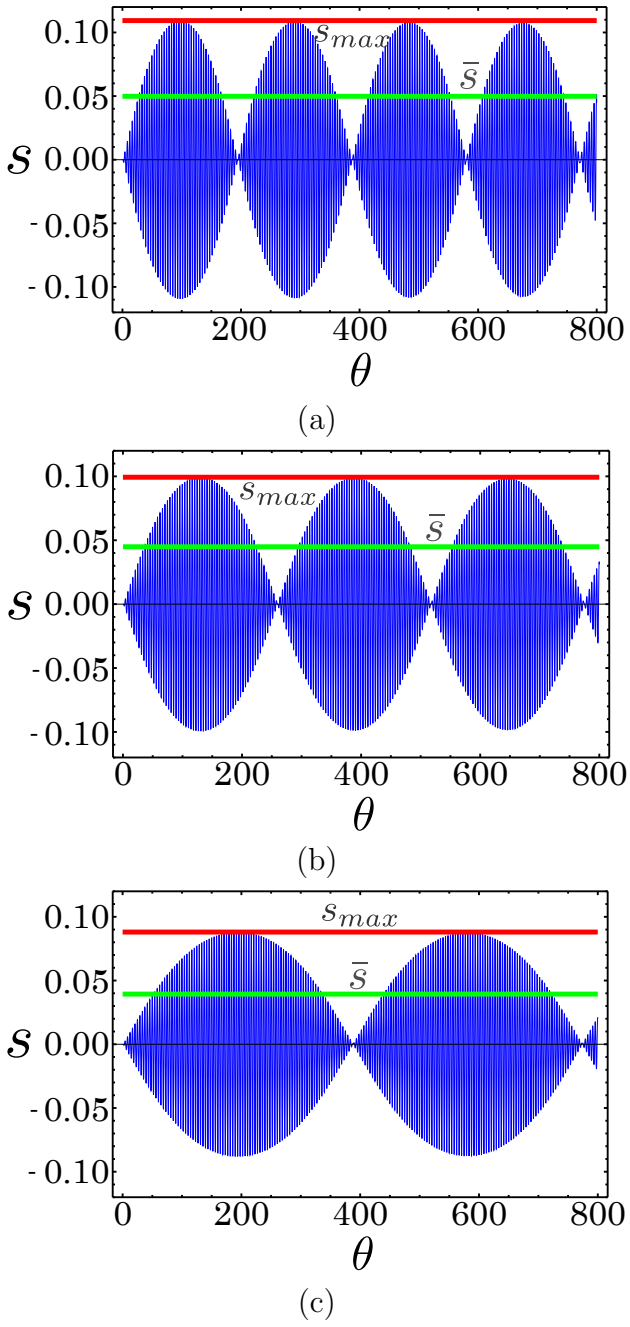

Figure 4.3: Simulations of the full EOM (equations (4.1) and (4.2)) for $\epsilon = 0.03$ and $n = 1.5$, and three sets of system parameter values that yield $\chi_C = 0.112$, with a predicted overshoot of 122%. (a) $\Gamma_C = 1.171$, $\tilde{n} = 1.52$ ($\sigma_C = -4.263$), $\lambda = 0$ ($\xi_C = -4.22$), simulated percent overshoot = 119%; (b) $\Gamma_C = 0.799$, $\tilde{n} = 1.51$ ($\sigma_C = -3.253$), $\lambda = 0.1$ ($\xi_C = -4.03$), simulated percent overshoot = 121%; (c) $\Gamma_C = 0.477$, $\tilde{n} = 1.5$ ($\sigma_C = -2.25$), $\lambda = 0.2$ ($\xi_C = -3.732$), simulated percent overshoot = 124%. Additional parameters used to simulate the full EOM include: $\Gamma_0 = \Gamma/2$, $\alpha = 0$, and $\beta = 1$.

σ_i, and a fixed excitation amplitude Γ_i, increasing (decreasing) the nonlinearity from the linear system ($\xi_i = 0$) will result in a decrease (increase) in the overshoot. The softening paths will eventually reach the jump point at $\chi = \chi^\star$, which is the last overshoot point shown on all seven curves for $\chi_i > 0$ in Fig. 4.4. Therefore, for zero initial conditions, one can see how the damping and the scaling will affect the location of the jump point. The presence of damping reduces the absorber overshoot and extends the parameter range over which the transient response from zero initial conditions results in the desired response. In addition, for the near-tautochronic scaling, the parameter γ has a similar effect of reducing the system overshoot as the jump point is approached. However, this effect diminishes as the system moves in the opposite (hardening) direction, and eventually the $\gamma \neq 0$ overshoot will converge to the $\gamma = 0$ overshoot curve as $\chi_t \to -\infty$[3].

4.3.2 Ramping the Excitation Torque

At this point an important issue regarding the form of the excitation torque will be addressed. It is observed in simulations of the full EOM that the sign of the torque immediately after it is switched on (i.e., $+\Gamma \sin(n\theta)$ or $-\Gamma \sin(n\theta)$) has a significant effect on the level of absorber overshoot. While the steady-state amplitude of the absorber does not depend on this sign, the peak amplitude of the first transient pulse in the beat response does depend on the manner in which the torque is initially applied. This is because a torque input that is initially positive (negative) will cause a rapid, but temporary, increase (decrease) in the rotor speed, and this will temporarily increase (decrease) the centrifugal restoring

[3]We note that the near-tautochronic averaged equations can be evaluated in the limit $\gamma \to 0$, resulting in the same averaged equations obtained for the general path scaling, except for the differences in definitions of the system parameters χ_t and χ_c.

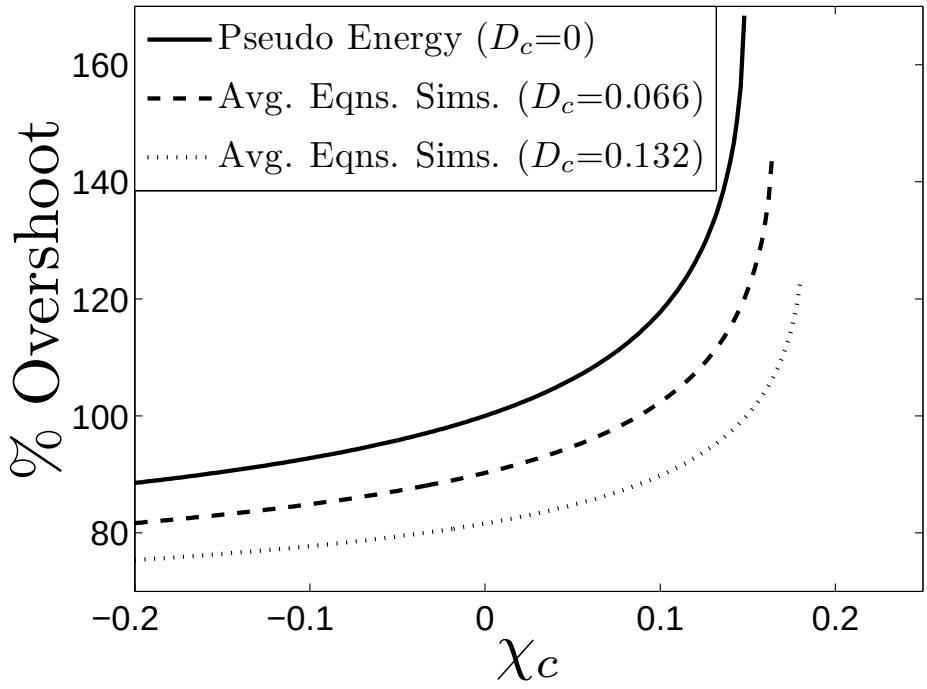

(a)

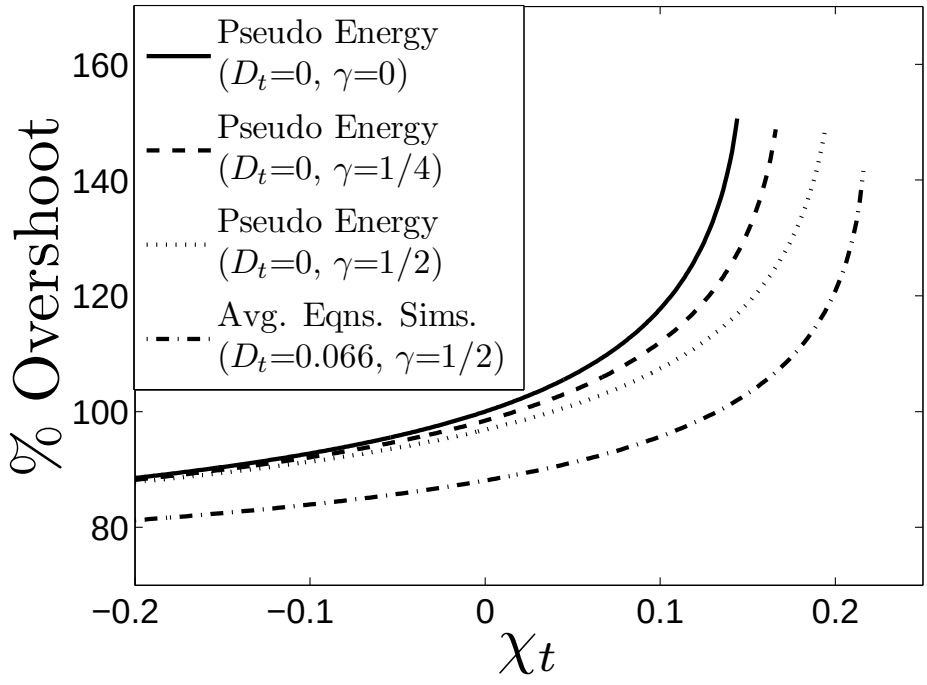

(b)

Figure 4.4: The percent overshoot of an absorber system subject to zero initial conditions, computed using the pseudo-energy method for $D_i = 0$, and using the averaged equations for $D_i \neq 0$; for (a) general path and (b) near-tautochronic absorbers.

force acting on the absorber mass, which results in a decrease (increase) in the absorber overshoot. This situation is depicted in Fig. 4.5 (a)-(d), which shows the simulated rotor and absorber response for sinusoidal inputs started with opposite signs, and the resulting difference in rotor transient and absorber overshoot. This effect is not captured by our

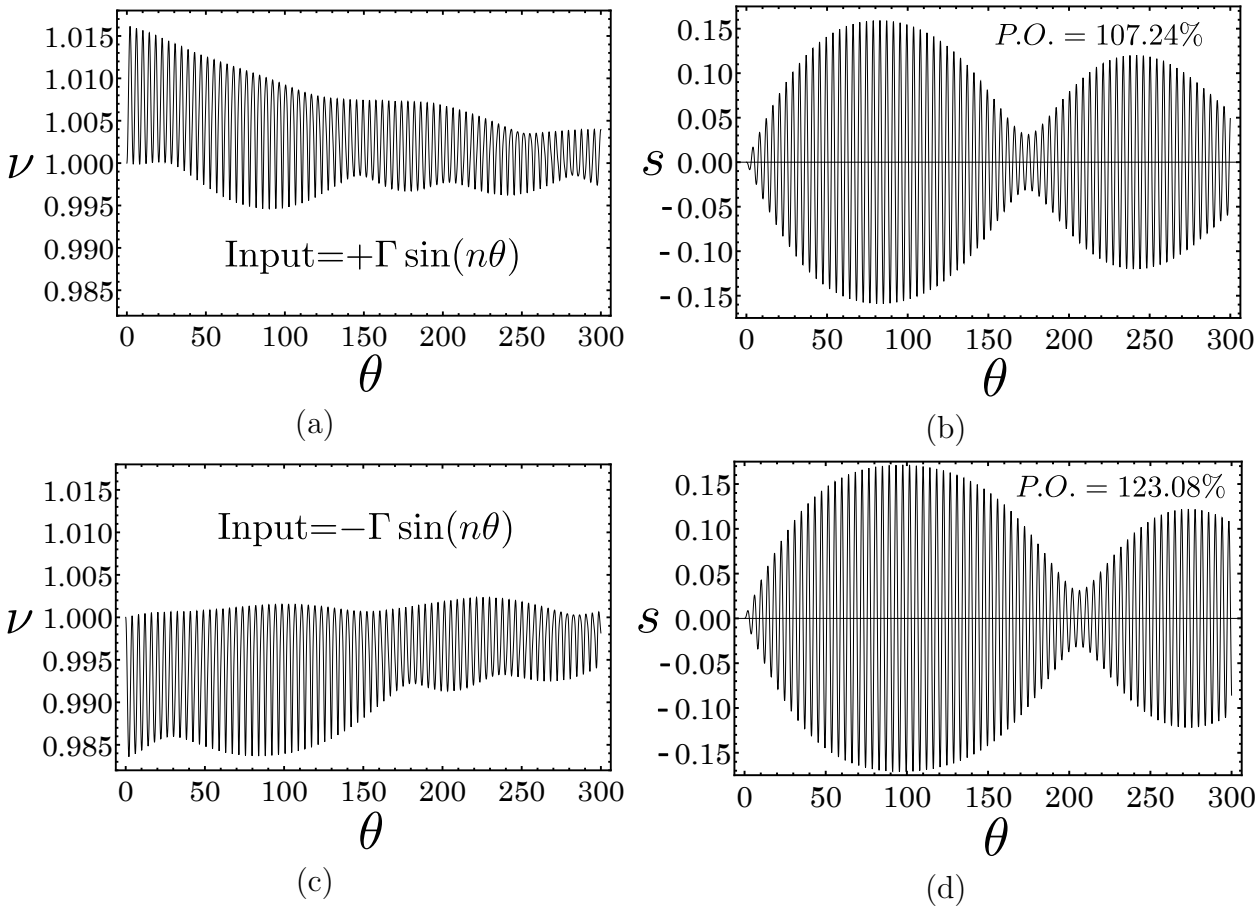

Figure 4.5: The rotor and absorber response to a step input of sinusoidal torque. (a) Rotor and (b) absorber response to input $+\Gamma \sin(n\theta)$; (c) rotor and (d) absorber response to input $-\Gamma \sin(n\theta)$.

model, since the scaling employed assumes a constant mean rotor speed ($\nu = 1$) in equation (4.3), an assumption used to uncouple the absorber and rotor responses to leading order in ϵ. Therefore, the perturbation analysis cannot capture this transient change in the mean rotor speed. This difference in the overshoot is not observed in experiments [47], due to the fact

that the torque input is not an exact step input of a sinusoid, but, due to the electronics, has a short transition period. Furthermore, this short transition in the torque input is even more likely in automotive applications, since cylinder deactivation is not instantaneous. Therefore, we minimize this dependence on the torque sign by quickly ramping up the sinusoidal torque from zero to its full value. The duration of the ramp θ_r used in simulations is the minimum crank angle duration that removes the torque sign dependence, and this is found to be one-half a forcing cycle, $\theta_r = \pi/n$. This ramp time is small compared to the time at which the absorber peak amplitude is reached. Using this ramp, the difference in the absorber overshoot is essentially eliminated; for example, for the case shown in Fig. 4.5 (b) & (d), the ramped input results in overshoot values of 118.30% and 118.56% for negative and positive torque, respectively.

4.4 Results and Discussion

We now compare results from the analytically predicted overshoot with those obtained from simulations of the full EOM, equations (4.1) and (4.2). The analytical predictions for zero absorber damping ($\mu = 0,\ D_i = 0$) are obtained using the pseudo-energy method and those with non-zero absorber damping are obtained by simulating the averaged equations (equations (4.10) and (4.11)). It is shown that the general path scaling provides an accurate estimate of the overshoot for absorber systems throughout the entire two-parameter family of paths when peak amplitudes are kept at moderate levels. In fact, it is noted that as the nonlinear absorber path parameter λ increases from a circle towards a cycloid, the absorber cusp amplitude s_{max} decreases [17]. Therefore, for paths near tautochronic, the general path pseudo-energy is found to provide the same accuracy as the near-tautochronic path pseudo-

energy when considering moderate absorber amplitudes riding on paths with $\lambda_e \leq \lambda \leq 1$. However, the accuracy of the general path breaks down as the excitation and tuning order increase, so that the absorber is pushed out near the cusp of the epicycloid, and the near-tautochronic scaling is able to predict the overshoot for these cases. In all comparisons we fix the excitation order $n = 1.5$, which corresponds to the transient response from cylinder deactivation to 3 cylinders, from, say 6 cylinders, assuming a four-stroke engine. Lastly, in all simulations of the full EOM we set the mean torque $\Gamma_0 = \Gamma/2$.[4]

Shown in Fig. 4.6 is a comparison for the general path pseudo-energy theory and simulations of the full EOM for the case of zero damping and a system inertia ratio of $\epsilon = 0.03$. The three sets of simulations shown in Fig. 4.6 are obtained by individually sweeping the three system parameters contained in χ_C, namely ξ_C, Γ_C, and σ_C. In the full EOM, the sweep of ξ_C is performed by sweeping the nonlinear tuning parameter λ, the sweep of Γ_C is done by sweeping the non-dimensional torque $\epsilon\Gamma$, and the sweep of σ_C is performed by sweeping the linear tuning order $\tilde{n}$. The exact values used in the three sweeps can be extracted from the information given in the caption of Fig. 4.6. The results show that the pseudo-energy method gives a very accurate prediction of the system response, except for the sweep of σ_C, which shows some deviation in the simulation points closest to $\chi = 0$ and $\chi = \chi^\star = 4/27$. For the simulations near $\chi = 0$, the deviation is due to the fact the absorber is far from resonance (as far as $\tilde{n} = 1.58$ which results in $\sigma_C = -10.463$), where it is not surprising that the averaging method breaks down. Furthermore, recall that χ_C scales like σ_C^{-3}, making it relatively sensitive to changes in the detuning. For simulations near $\chi^\star$, the deviation is due to the large absorber amplitudes that occur when the system is excited very close to

[4]We note that the results shown here break down when the mean torque is $\Gamma_0 > 2\Gamma$, which is expected since both torques are scaled in the same manner.

resonance, as close as $\tilde{n} = 1.501$ at the simulation point closest to $\chi^\star$.[5] This is in contrast to the $\epsilon\Gamma$ and λ sweeps, which were performed at a linear tuning of $\tilde{n} = 1.51$, resulting in moderate peak absorber amplitudes in all cases.

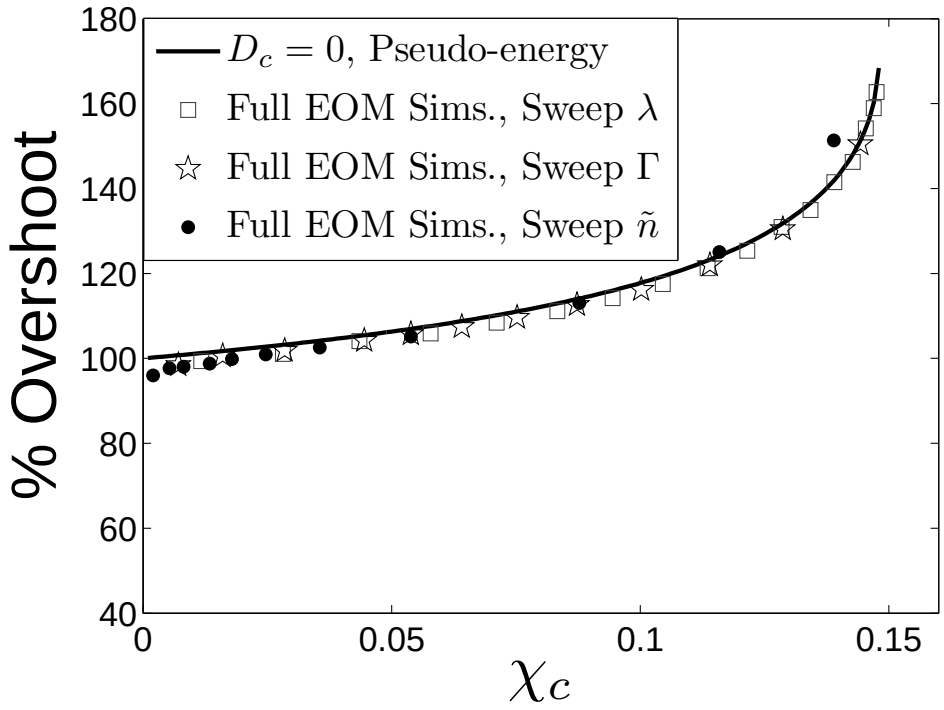

Figure 4.6: Comparison of the general path pseudo-energy method with simulations of the full EOM for $\mu = 0$, $n = 1.5$, $\epsilon = 0.03$, $\Gamma_0 = \Gamma/2$, $\alpha = 0$, and $\beta = 1$. Solid line is the pseudo-energy prediction. Simulation data: **Sweep of** χ_C by varying λ from 0.80 to 0 with $\epsilon\Gamma = 0.005$, and $\sigma_C = -3.25$ ($\tilde{n} = 1.51$). **Sweep of** χ_C by varying $\epsilon\Gamma$ from 0.001 to 0.006 with $\xi_C = -4.09$ ($\lambda = 0$), and $\sigma_C = -3.25$ ($\tilde{n} = 1.51$). **Sweep of** χ_C by varying $\tilde{n}$ from 1.58 to 1.501 with $\epsilon\Gamma = 0.003$ (note that in this case varying $\tilde{n}$ results in sweeping ξ_C from -5 to -4 for a fixed $\lambda = 0$).

Shown in Fig. 4.7 (a)-(b) is a comparison between the general path pseudo energy method and simulations of the full EOM for the case of increasing the system inertia ratio ϵ. Note that increasing ϵ has the same effect as increasing the absolute magnitudes of the three main system parameters, as seen from the caption of Fig. 4.7. The results of Fig. 4.7 indicate that

[5]Recall that for general path absorbers, the absorber amplitude is scaled by $\epsilon^{1/2}$, and the resulting perturbation equations break down for large amplitudes.

the full EOM overshoot results begin to deviate from the theory in a manner similar to that seen for the detuning sweep shown in Fig. 4.6. As is standard in perturbation equations, as one increases the small scaling parameter, the accuracy of the approximation diminishes. In addition, increasing ϵ will increase the torque magnitude $\epsilon\Gamma$, and the magnitude of the softening nonlinearity ξ_C which results in larger transient amplitudes, which violates the moderate amplitude assumption used for these paths. This effect becomes more prominent near $\chi^\star$. Near $\chi_C = 0$, only the detuning sweep deviates significantly; this is expected, since the absorber is tuned far from resonance ($\tilde{n} = 1.58$). On the other hand, there is less deviation for the overshoot near $\chi_C = 0$ for the full EOM sweeps of λ and $\epsilon\Gamma$, because the nonlinearity ξ_C and torque amplitude Γ_C tend to zero as $\chi_C \to 0$. Overall, the theory provides a valuable prediction for the absorber overshoot up to $\epsilon \approx 0.10$, and the predictions are generally conservative, except near the jump point.

Shown in Fig. 4.8 are results for lightly damped systems, using the general path averaged equations for the theory and comparing with simulations of the full EOM. Two sets of data are shown, for which the value of the damping ratio ζ is doubled from $\zeta = 0.001$ to $\zeta = 0.002$[6]. Note that only system parameters λ and $\epsilon\Gamma$ are swept, since the scaled damping coefficient D_i, which is held constant for these parameter sweeps, depends on n and $\tilde{n}$ (see equation (4.12)). The damping dependence on the excitation and tuning parameters is an interesting consequence of the scaling, and for a linear system $\chi_C = 0$, the damped overshoot is remarkably only a function of the damping coefficient D_C. Additionally, as one approaches resonance, $\sigma_C \to 0$, $D_C \to \infty$, which recovers the zero overshoot result for a damped linear system excited exactly at resonance. As seen in Fig. 4.8, the averaged equations provide an

[6]The viscous damping coefficient μ is related to the damping ratio ζ by $\mu = 2\zeta\tilde{n}$.

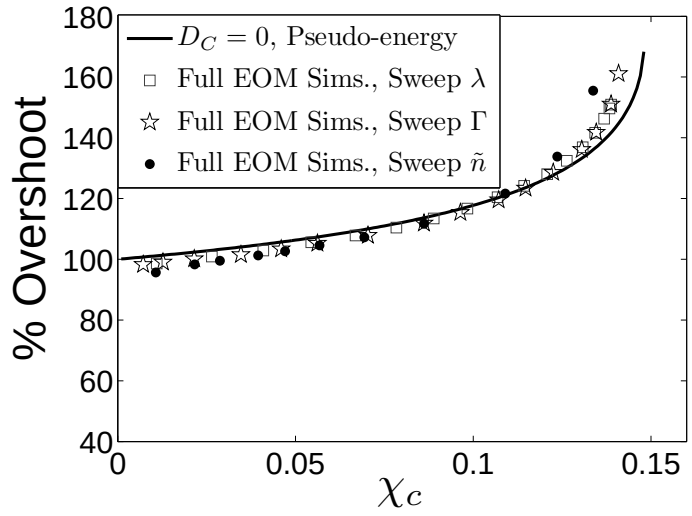

(a)

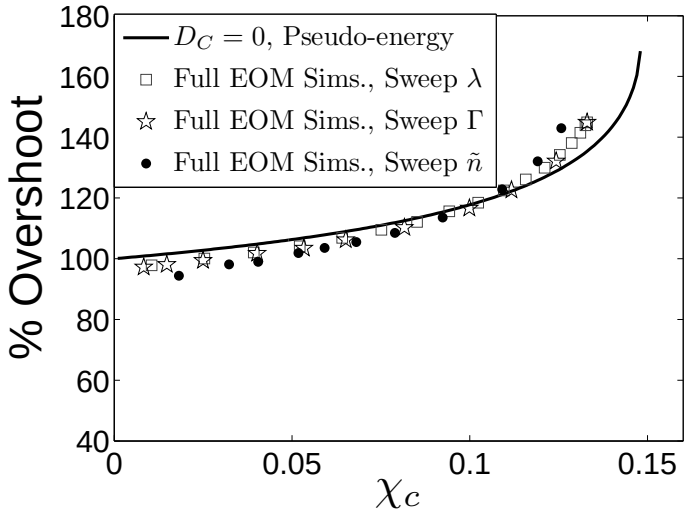

(b)

Figure 4.7: Comparison of the general path pseudo-energy method with simulations of the full EOM for $\mu = 0$, $n = 1.5$, $\Gamma_0 = \Gamma/2$, $\alpha = 0$, and $\beta = 1$. Solid line is the pseudo-energy prediction. **(a)** $\epsilon = 0.07$ with simulation data: **Sweep of** χ_C by varying λ from 0.80 to 0 with $\epsilon\Gamma = 0.012$, and $\sigma_C = -2.68$ ($\tilde{n} = 1.51$). **Sweep of** χ_C by varying $\epsilon\Gamma$ from 0.003 to 0.013 with $\xi_C = -4.09$ ($\lambda = 0$), and $\sigma_C = -2.68$ ($\tilde{n} = 1.51$). **Sweep of** χ_C by varying $\tilde{n}$ from 1.58 to 1.501 with $\epsilon\Gamma = 0.01$ (note that in this case varying $\tilde{n}$ results in varying ξ_C from -5 to -4 for a fixed $\lambda = 0$) **(b)** $\epsilon = 0.10$ with simulation data: **Sweep of** χ_C by varying λ from 0.80 to 0 with $\epsilon\Gamma = 0.019$, and $\sigma_C = -2.55$ ($\tilde{n} = 1.51$). **Sweep of** χ_C by varying $\epsilon\Gamma$ from 0.005 to 0.021 with $\xi_C = -4.09$ ($\lambda = 0$), and $\sigma_C = -2.55$ ($\tilde{n} = 1.51$). **Sweep of** χ_C by varying $\tilde{n}$ from 1.58 to 1.501 with $\epsilon\Gamma = 0.016$ (note that in this case varying $\tilde{n}$ results in sweeping ξ_C from -5 to -4 for a fixed $\lambda = 0$)

accurate prediction of the damped system overshoot, with the same limitations discussed previously, plus the additional requirement of small damping, required since the damping coefficient μ is scaled by ϵ for all paths.

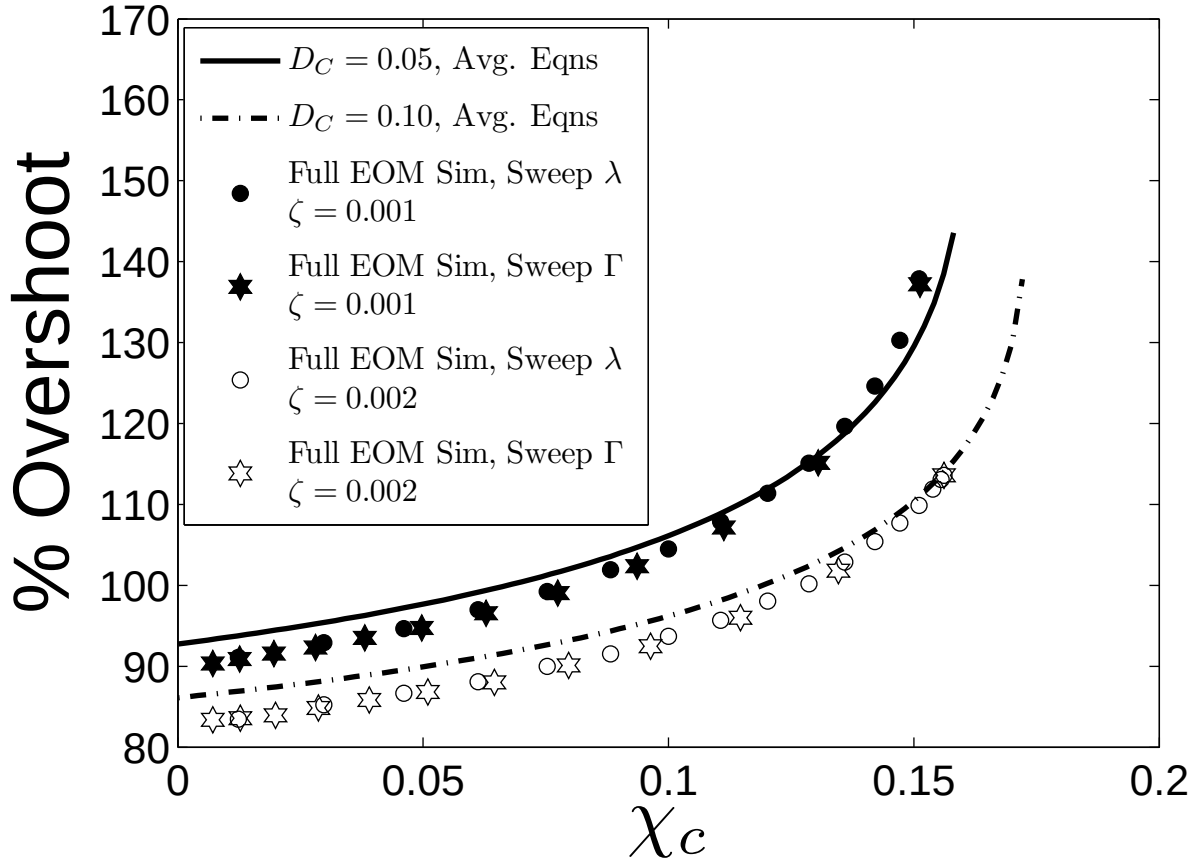

Figure 4.8: Comparison of the general path pseudo-energy method with simulations of the full EOM for $D_C = 0.05$ ($\zeta = 0.001$) and $D_C = 0.10$ ($\zeta = 0.002$). Simulation data: **Sweep of** χ_C by varying λ from 0 to 0.80 with $\epsilon\Gamma = 0.013$. **Sweep of** χ_C by varying $\epsilon\Gamma$ from 0.003 to 0.013 with $\xi_C = -4.09$ ($\lambda = 0$). Other parameter values used in simulations are: $\tilde{n} = 1.51$, $n = 1.5$, $\epsilon = 0.07$, $\Gamma_0 = \Gamma/2$, $\alpha = 0$, and $\beta = 1$.

Shown in Fig. 4.9 (a) & (b) is a comparison of the near-tautochronic pseudo-energy results and simulations of the full EOM for $\lambda = \lambda_e$ and $\epsilon = 0.07$. Two pseudo-energy curves are generated, obtained by sweeping $\tilde{n}$ and $\epsilon\Gamma$, since both χ_t and γ depend on these two system parameters. As seen in Fig. 4.9 (a) & (b), the near-tautochronic pseudo-energy method

provides a conservative estimate of the absorber overshoot. The results show the tautochronic absorber to be almost linear, that is, with 100% overshoot nearly all the way up to the cusp amplitudes. This near-linear behavior is a result of the fact that the path nonlinearity is zero (by definition of the tautochrone), and the competition between the small softening value of ξ_t for $\lambda = \lambda_e$ and the mild hardening effect of γ (which diminishes the effect of the torque on the absorber), resulting in an almost net neutral effect. Therefore, the general path pseudo-energy method, which predicts 100% overshoot for the tautochronic path absorber, is as good as the near-tautochronic pseudo-energy for a range of $\tilde{n}$ values, in this case near 1.5. As the tuning order $\tilde{n}$ and excitation order n increase, the magnitude of the softening nonlinearity ξ_t increases, with negligible change in the hardening parameter γ (for a slightly over-tuned absorber, $\tilde{n} > n$) which eventually results in the general path failing to capture the amount of softening observed in the overshoot. In fact, this is observed at $\tilde{n} = 1.51$ when λ is very close but just below tautochronic λ_e, in this case the softening observed in simulations of the full EOM overshoot is only accurately captured using the near-tautochronic scaling. However, it seems that for practical non-circular paths (i.e. $\lambda_e \leq \lambda \leq 1$), the general path scaling provides a good approximation of overshoot for slightly over-tuned systems up to an excitation order of $n = 3$.

4.5 Conclusions

The results of this chapter provide a simple way to estimate the overshoot of centrifugal vibration absorbers when the rotor is suddenly subjected to near-resonant torsional excitation. A simple, compact formulation for the percent overshoot of the absorber amplitude is derived from the full equations of motion by a series of rescalings and approximations,

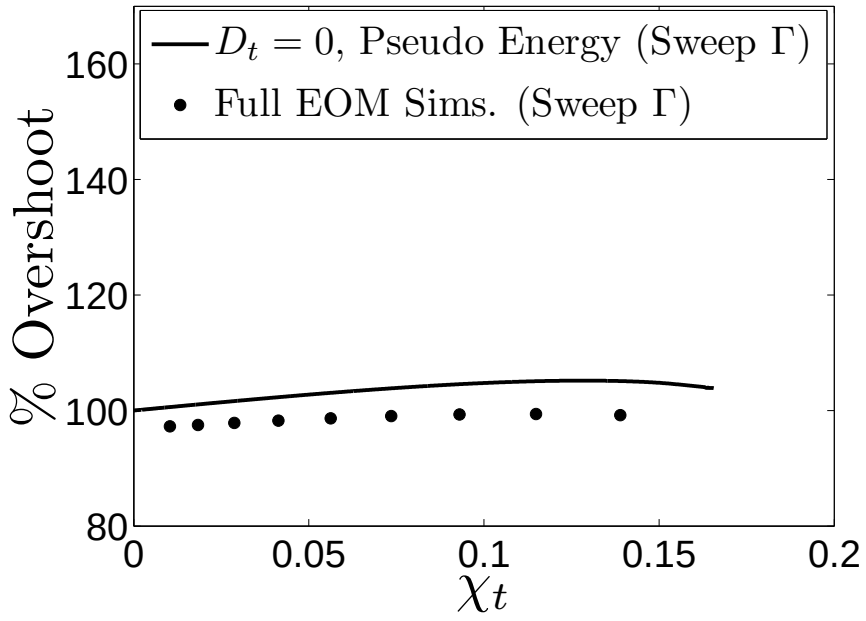

(a)

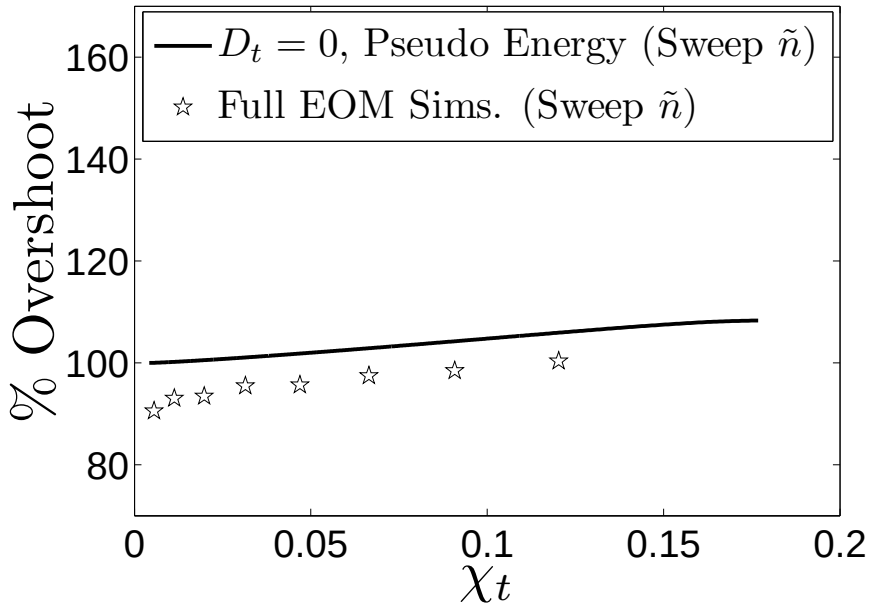

(b)

Figure 4.9: Comparison of the near-tautochronic path pseudo-energy method with simulations of the full EOM for $\lambda = \lambda_e$, $\mu = 0$, $n = 1.5$, $\epsilon = 0.07$, $\Gamma_0 = \Gamma/2$, $\alpha = 0$, and $\beta = 1$. **(a)** Simulation data: **Sweep of** χ_t by varying $\epsilon\Gamma$ from 0.009 to 0.033 and $\sigma_t = -2.68$ ($\tilde{n} = 1.51$). **(b)** Simulation data: **Sweep of** χ_t by varying $\tilde{n}$ from 1.67 to 1.50 with $\epsilon\Gamma = 0.028$.

including the method of averaging. For the case when the dominant nonlinearity arises from the absorber path, and damping is negligible, the formulation boils down to a convenient

closed form expression (specifically, roots of a cubic or quartic equation, depending on initial conditions) that depends on a single parameter. In fact, this case reduces to the transient response of a simple Duffing oscillator, considered in Chapter 3. For absorber systems where the dominant nonlinearity arises from kinematic coupling to the rotor, the overshoot estimate for undamped systems depends on two parameters, and requires finding the root of an equation that involves elliptic functions. For all path types, more accurate estimates that account for damping are available via simulation of the averaged equations. Simulations of the full nonlinear equations of motion demonstrate the accuracy and utility of the approximate results over a wide range of system parameters. From a design point of view, the undamped system results are particularly convenient, since they are easy to compute and provide a conservative estimate of the overshoot. These results will be of use for a variety of applications, including use in automotive engines that utilize cylinder deactivation. Experimental verification of these results are provided in Chapter 5.

Chapter 5

Transient Dynamics of a Single CPVA System, Experiment

5.1 Introduction

The results of an experimental investigation of the transient dynamics of centrifugal pendulum vibration absorbers (CPVAs) are presented, and compared with the theoretical and simulation results described in Chapter 4. Here we describe the experimental apparatus, the methods used for determining system parameters, and the results of systematic experiments performed using the apparatus. The experiments conducted consist of responses due to the instantaneous activation of near-resonant torsional excitation of the rotor, so that the absorber response transitions from an essentially quiescent state to a periodic steady-state. This mimics the conditions encountered during cylinder deactivation in variable displacement automotive engines fitted with pendulum absorbers that are tuned for the torsional excitation encountered in the reduced cylinder mode of operation. This input leads to a

beating-type transient motion, resulting in an overshoot of the absorber amplitude response before it reaches steady state. The purpose of this chapter is to experimentally measure this overshoot in order to verify the analytical predictions in Chapter 4.

We consider the response of a system consisting of a rotor and a single absorber. The fully instrumented apparatus can provide prescribed torque inputs and measure the resulting responses of the absorber and rotor. The overshoot experiments are performed using absorbers with two different path types, circular and near-tautochronic. Both paths have a softening nonlinearity when coupled to the rotor, one quite strong (circular path) and one close to neutral (near-tautochronic). These differences will be useful for validating the model equations of motion (EOM) and verifying the analytical overshoot predictions.

The apparatus absorbers used in this study have been used previously for studies of steady state responses, which considered single and multi-absorber systems, and were used to validate perturbation analytical results for general path absorbers [26, 53, 76] and near-tautochronic path absorbers [70]. Previous studies considering the transient dynamics of pendulum vibration absorbers include simulations for circular path absorbers [59] and analytical closed form results for damped linear absorbers [69], which closely approximate the results for near-tautochronic absorbers. In this chapter we describe the first known systematic experimental investigation of transient absorber response, and compare it with analytical predictions.

The chapter begins with a description of the experimental test apparatus, whose main components are explained in detail, along with a description of how the rig is used to perform cylinder deactivation experiments. The processes for identifying the required experimental system parameters, specifically, the absorber tuning order $\tilde{n}$, the absorber damping μ, the

nonlinearity in the absorber path λ, and the system inertia ratio ϵ, are explained. With these parameters in hand, comparisons between analysis, simulations, and experiments can be carried out for a range of loading conditions. It is shown that the EOM provide a very accurate prediction of the experimentally observed overshoot, that the damped averaged equations also provide accurate, and mostly conservative, predictions, and that the pseudo-energy predictions provide an upper bound for the overshoot. The benefits of the pseudo-energy results are that they are simple to obtain, are expressed in terms of minimal system parameters, notably, χ_C, and are conservative, making them very convenient for accounting for transient responses in absorber designs. One conclusion of this study is that the general path model is suitable for most absorber paths, and the near-tautochronic results are required only in special situations. In fact, for the experiments described here, the general path results suffice for both absorbers.

5.2 The Experimental Apparatus

We begin by providing a description of the components of the experimental spin rig shown in Fig. 5.1, and explain how the rig is used to perform the transient experiments. This basic rig was described and characterized previously in works considering steady state absorber responses [26, 52, 53, 70]. For the present studies the rig was upgraded with a new servo motor (C) and controller (B) and has undergone significant software updates for motor control, response readouts, and data processing. In addition, flywheel weights were fabricated to allow the inertia ratio of the system ϵ to be adjusted [76]. Lastly, to study the gravitational influence on the absorber dynamics, the rig has been modified so that it can be run horizontally, i.e., rotated by 90^{o} from the orientation shown in Fig. 5.1. Gravity will have very little

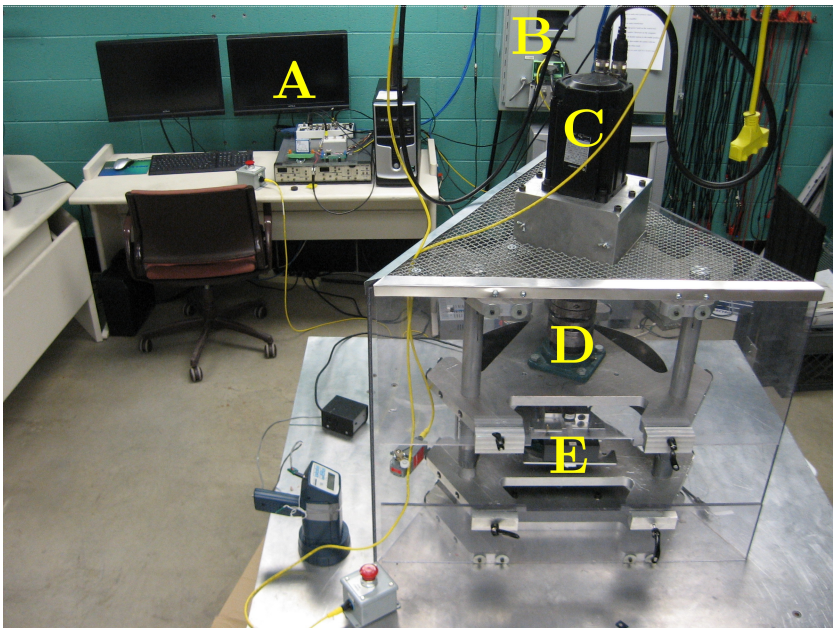

Figure 5.1: The experimental apparatus, with components: (A) computer for system control and data processing, (B) motor controller, (C) servo motor, (D) rotor encoder, (E) absorber with encoder.

influence on the absorbers response at speeds when cylinder deactivation is likely to occur. Therefore, all experiments described here are carried out with the test rig in the orientation shown in Fig. 5.1. This eliminates the effects of gravity and allows the experiments to be run at low speeds, specifically, $\Omega \approx 350$ RPM.

5.2.1 System Components and Parameters

The experimental apparatus uses an electric motor and control system capable of applying a user-specified torque to the rotor, including transient inputs, while maintaining a near-constant rotation speed of the rotor. The rotor and absorbers are fitted with encoders for measuring their responses, and a current feedback measurement from the motor is utilized to determine the instantaneous torque acting on the rotor. A primary advantage of this apparatus is that it allows one to systematically vary the torque order n, and thus the

detuning between the input order and the absorber order, a parameter not easily changed in engines and other rotors, since these orders are typically integers and fixed by hardware.

The apparatus consists of five main components, labeled (A)-(E) in Fig. 5.1. Component (A) is a computer running a LabVIEW program that generates the user specified harmonic torque signal and sends it to the control box (B), which then sends the signal to the motor (C), commanding it to perform the desired torque. The computer is also used for data collection and processing. Note that the applied torque in an automotive engine depends on the rotor angle θ (e.g., $T_n \sin(n\theta)$), rather than time, and therefore the harmonic torque signal generated in LabVIEW uses feedback from encoder (D), which instantaneously measures the rotor orientation. This encoder produces 1000 pulses per revolution and informs LabVIEW how to increment the torque during rotor revolution. The torque signal contains a mean component T_0, used to maintain a desired rotor speed Ω, plus a user-specified varying part, which can be harmonic ($T_n \sin(n\theta)$), step, etc. The mean rotor speed is held close to constant by making slight incremental adjustments to T_0, determined by an onboard slow-time PID controller in LabVIEW. The mean torque T_0 and fluctuating torque T_f are related to their non-dimensional counterparts $\Gamma_{0,f}$ by $T_{0,f}/(J\Omega^2) = \epsilon\Gamma_{0,f}$, where J is the rotor inertia and $\epsilon = mc^2/J$ is the (small) ratio of absorber rotational inertia to rotor inertia, expressed in terms of the absorber mass m and the distance from the rotor center to the absorber zero position c, as shown in Fig. 4.1.

The vibration absorbers are placed at position (E) in Fig. 5.1. Here we consider two different absorber types, one with a circular path and the other with a nearly tautochronic path. This allows us to experimentally investigate the effects of the path nonlinearity on the absorber overshoot, and make comparisons with model predictions [46]. The absorber shown

in Fig. 5.2 (a) is a near-tautochronic path absorber with a bifilar suspension, as considered in [70]. The tautochronic path is accomplished by suspending the absorber mass (the dark gray block in Fig. 5.2 (a)) from two tempered blue spring steel bands that wrap around aluminum cheeks that are machined with the required evolutes, so that the center of mass follows the desired involute. In addition, to achieve the bifilar type suspension, there are bearings at each point where the steel bands connect to the absorber, and these constrain the absorber such that it only translates relative to the rotor, and does not induce any bending in the bands. The absorber shown in Fig. 5.2 (b) is a circular path pendulum type absorber suspended at a single pivot point, as considered in [53]. In contrast to the near-tautochronic absorber, the circular path absorber is a compound pendulum absorber suspended by a pin and needle bearing. Note that this absorber will translate and rotate relative to the rotor, which affects its effective inertia, and thus its linear tuning order $\tilde{n}$, as explained below. A rotary encoder is attached to the absorbers (E) (only shown on the tautochronic absorber in Fig. 5.2 (a)), which provides an angular measurement of the absorber position. Note that although the path followed by the near-tautochronic absorber is not circular, the angular measurement taken by the encoder using a pin on the absorber and an arm with a slot on the encoder, varies almost linearly with the arc-length [43]. Therefore, the encoder angular measurement is used to determine the position for both types of absorbers, with a measurement resolution of about 0.25^{o}.

5.2.2 Transient Testing Capabilities

The rig is capable of performing experiments which emulate cylinder deactivation events in variable displacement automotive engines. Typically, half of the cylinders are shut down

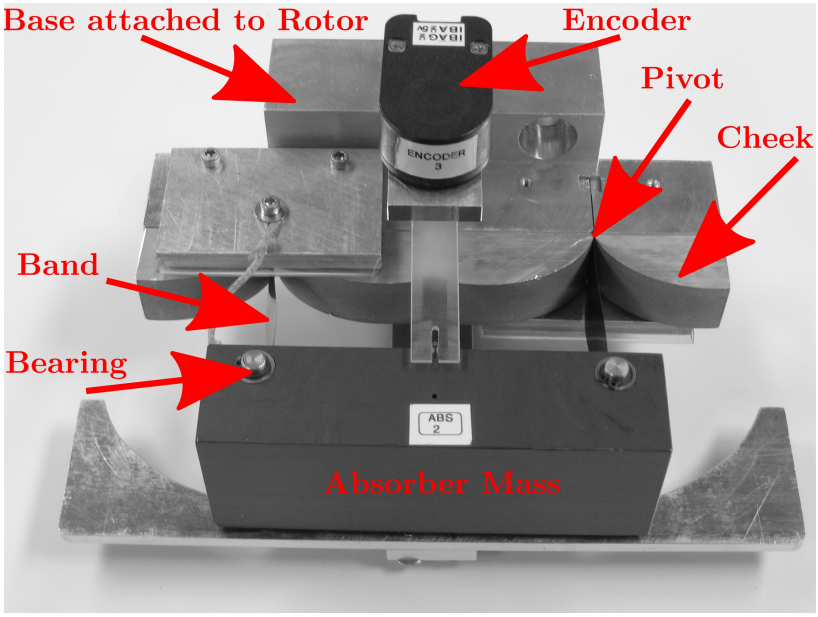

(a)

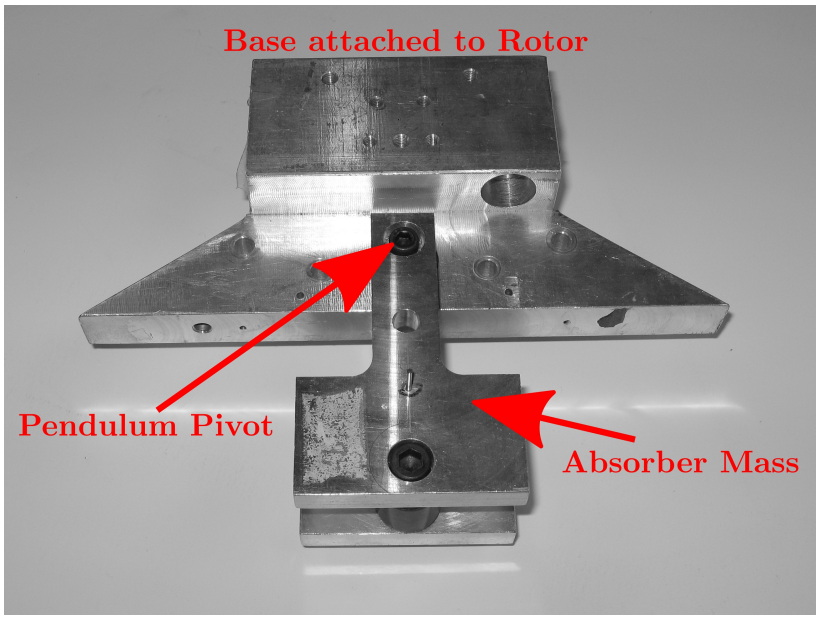

(b)

Figure 5.2: Absorber pendulums: (a) near-tautochronic absorber (dark gray), suspended by two steel bands that wrap around cheeks, generating the desired path, shown with an encoder attached; (b) circular path absorber (inverted "T"), suspended by a pin and needle bearing, as indicated.

during deactivation, which results in a torque order transition from $2n$ to n where, for a four stroke N cylinder engine, $n = N/4$. This is accompanied by an increase in the amplitude

of the dominant harmonic torque T_n by a factor of about 2-3 over that experienced in full cylinder operation. This increase in amplitude results from the fact that the remaining active cylinders must generate more torque per cylinder in order to maintain the mean torque through the transition [66]. The experimental rig can perform these transitions by specifying step changes in torque amplitude and order, according to the scenario described. The rig is very flexible and can be programmed to investigate a wide variety of transient torque inputs. Since the absorber response in full cylinder mode is nonresonant, and thus nearly zero, zero initial conditions are used for all experimental runs. The step input is achieved by suddenly applying and maintaining a fluctuating torque $T_n \sin(n\theta)$, superimposed on the mean torque T_0. A sample of such an experiment using the circular path absorber is displayed in Fig. 5.3 (a)-(d), where the torque input measured by the motor feedback is shown in Fig. 5.3 (a), and the absorber response is shown in Fig. 5.3 (b). To see the rapid oscillations and initial transitions in these signals, close ups of Fig. 5.3 (a) & (b) are shown in Fig. 5.3 (c) & (d), respectively. In this simulated cylinder deactivation event (depicted in Fig. 5.3 (a)), the absorbers abruptly experience a near-resonant excitation, resulting in the beating-type transient response shown in Fig. 5.3 (b), composed of dominant harmonic components at order n and approximately order $\tilde{n}$, the latter shifted by nonlinear effects. The absorbers eventually settle down into the order n steady-state, on a time scale set by the frequency $n\Omega$ and damping.

5.3 Parameter Identification

In order to compare the experimental and analytical results, the experimental system parameter values need to be determined for both types of absorbers. The torque order n and

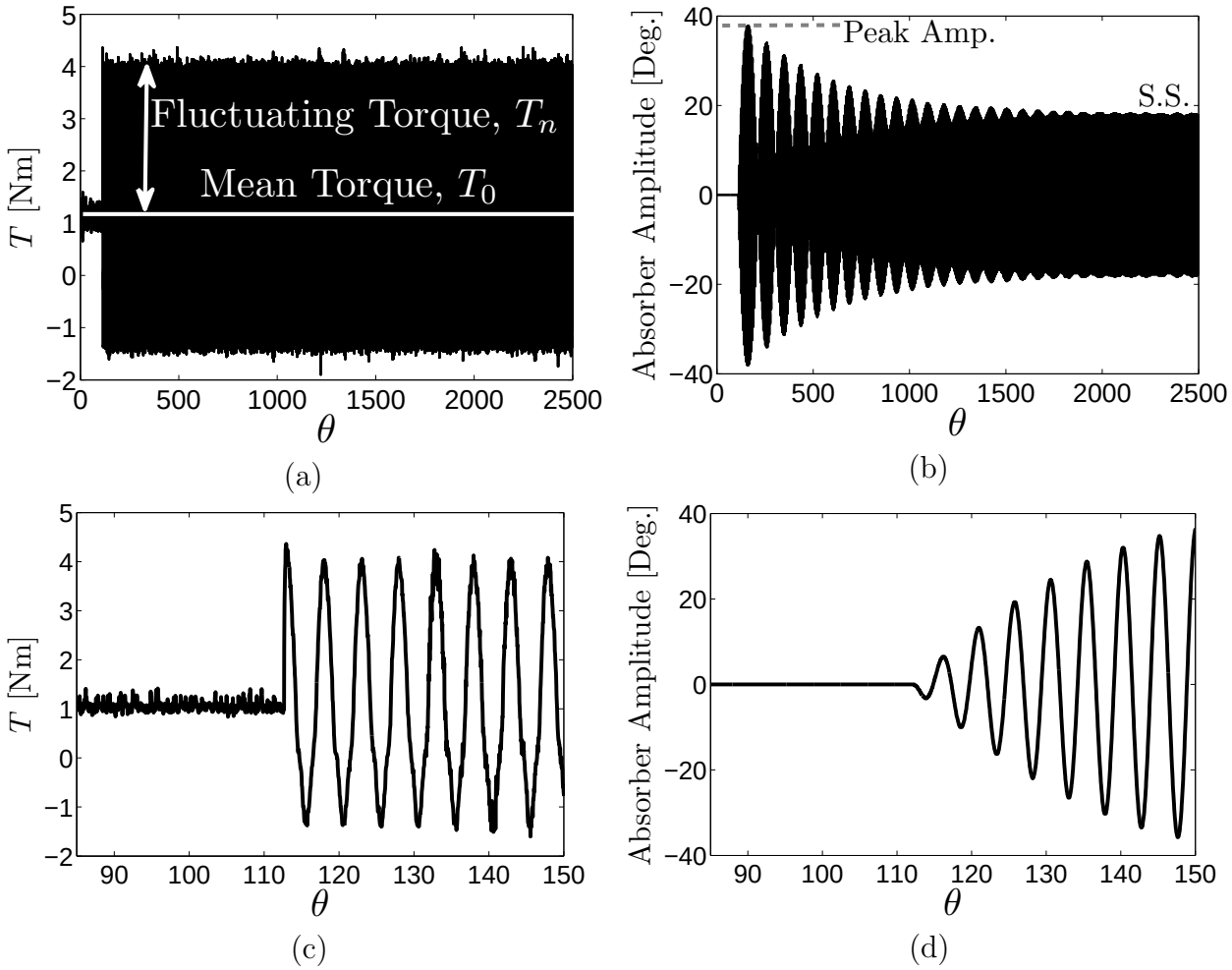

Figure 5.3: An experimentally simulated cylinder deactivation event showing the torque input and the resulting transient absorber response. (a) Input torque $T = T_0 + T_n \sin(n\theta)$ applied to rotor by the servo motor; (b) absorber transient amplitude response to the input torque; (c) zoom-in of the input torque at the transition point; (d) zoom-in of the absorber response at the transition point.

amplitude T_n, as well as the mean rotor speed Ω, can be varied by the user. The parameters taken to be fixed for each absorber type include the absorber equivalent viscous damping coefficient μ, the absorber tuning order $\tilde{n}$, and the absorber/rotor inertia ratio ϵ. Only a brief summary of how each system parameter is estimated is given, since these methods are abstracted from previous works [26,52,53,70]. An error analysis in regards to the uncertainty in the estimated system parameters is performed following the NIST Type A method [72].

Within the computed uncertainty bounds, the system parameters are chosen based on best agreement with transient simulations of the full EOM. The system parameters used to make analytical predictions are given in Tab. 5.1, and all of the estimated system parameters with their respective uncertainties for the circular path and the tautochronic path absorbers are given in Tabs. 5.2 & 5.3, respectively. In the following section, absorber overshoot results from transient experiments that mimic cylinder deactivation will be shown, along with comparisons with analytical predictions.

Table 5.1: The main system parameters for the spin rig needed for comparison with analytical predictions.

Type of Path	**General Path**	**Near Tautochronic**
Damping	$\mu = 0.0395$	$\mu = 0.0675$
Tuning Order	$\tilde{n} = 1.312$	$\tilde{n} = 1.449$
Inertia Ratio	$\epsilon = 0.0864$	$\epsilon = 0.1074$
Path Curvature	$\lambda = 0$	$\kappa = -1.518$ $(\lambda = 0.66)$

The absorber linear tuning order $\tilde{n}$ is obtained through a combination of physical length measurements and experimental tests. For the near-tautochronic path absorber, the linear tuning order is defined as

$$\tilde{n} = \sqrt{\frac{c - \rho_0}{\rho_0}}, \tag{5.1}$$

and for the circular path pendulum, the linear tuning order is defined as

$$\tilde{n} = \sqrt{\frac{c - \rho_0}{\rho_0 \beta}}, \tag{5.2}$$

where c is the distance from the center of rotation O of the spin rig to that of the absorbers' COM and ρ_0 is the radius of curvature of the absorber path at its vertex, as depicted in Fig. 4.1. The circular path absorber tuning order $\tilde{n}$ contains the additional term β that accounts for the inertial effects associated with a compound pendulum; specifically, the

rotational inertia scales the effective pendulum length ρ_0, as described in equation (5.2). Recall that parameters β and α were introduced in Chapter 4 to account for the compound pendulum absorber implementation, and these are related to the absorber geometry and inertia as follows

$$\beta = 1 + \left(\frac{r}{\rho_0}\right)^2, \qquad \alpha = \frac{r^2}{c\rho_0}, \tag{5.3}$$

where r is the radius of gyration of the circular path absorber about its COM; see Nester [53] for details. Note that these arise from the single point suspension of the absorber, and $\beta = 1$ and $\alpha = 0$ for all absorbers with bifilar suspensions, regardless of the path.

Following the method given in [53,70], the tuning order $\tilde{n}$ was determined experimentally by performing a sweep in the excitation order n, i.e., a frequency sweep. According to linear theory, when the rotor is excited at $n = \tilde{n}$, the rotor vibration amplitude $|\ddot{\theta}|$ is zero for zero damping, or a minimum for small damping. Therefore, the order n is experimentally swept and the corresponding rotor vibrations at each order are measured from the encoder on the rotor shaft. Specifically, the rotor encoder gives an instantaneous speed signal $\dot{\theta}(t)$ whose harmonic magnitudes in steady-state $|\dot{\theta}|_j$ ($j = n, 2n, \ldots$) are computed using an FFT, which are multiplied by $j\Omega$ to get the desired acceleration harmonic magnitudes, $|\ddot{\theta}|_j$. Using this method, with $j = n$, the circular path and near-tautochronic absorber tuning orders are found to be $\tilde{n} = 1.312$ and $\tilde{n} = 1.449$, respectively. The radius of gyration for the circular path absorber is found to be $r = 0.0347$m, as computed using the physically measured parameters ρ_0, c (see Tab. 5.2), along with the measured value for $\tilde{n}$. This results in $\alpha = 0.181$ and $\beta = 1.714$. Due to the bifilar suspension of the near-tautochronic path absorber, one can can simply use the measured geometry, specifically, c and ρ_0, given in Tab. 5.3, which yields values that precisely match the tuning obtained by order sweep measurements.

The experimental order sweep must be performed at a low level of fluctuating torque level T_n in order to keep the absorber amplitudes in the linear response range. On the other hand, the tautochronic path nonlinearity is only very lightly softening, from the kinematic coupling to the rotor, and the low torque amplitude requirement is not required for this absorber. However, the near-tautochronic path absorber used here exhibited some nonlinear frequency-amplitude dependence that was observed from an experimental order sweep performed over a range of torque levels, T_n. From the measured results, the nonlinear path curvature for the near-tautochronic absorber is found to be slightly softening ($\lambda = 0.66$), which results in a value of $\kappa = -1.518$ that describes the nonlinear detuning for near-tautochronic path absorbers [46, 68][1].

The absorber dissipation is modeled as an equivalent viscous damping and the attendant coefficient is measured experimentally. Although some Coulomb damping has been observed and quantified for the circular path absorber [76], for amplitudes greater than 10^{o} the absorber decay is captured very accurately with a viscous model. To obtain the damping coefficients, the log decrement method is applied to 13 consecutive peaks of a ringdown in amplitude, which is obtained by switching off the oscillating torque during a steady-state oscillation, resulting in a free decay of the absorber/rotor system. Note that in fact the rotor and absorber are coupled, and the rotor and absorber have independent damping characteristics; however, the experimentally measured values provide an effective damping that captures the combined effect that these dissipation sources have on the absorber, and therefore best reflects the damping coefficient needed for the absorber oscillator model considered in Chapter 4. The log decrement restricts the amplitudes used in calculating the damping

[1]The experimental results presented in [70] were limited in amplitude such that they match very closely those for an exact tautochronic path.

ratio to the linear range, that is, below 25^{O}. The damping ratio ζ calculated from the log decrement is related to the absorber damping coefficient by,

$$\mu = 2\zeta\tilde{n}, \tag{5.4}$$

where μ is the non-dimensional damping coefficient used in Chapter 4. As shown in Tabs. 5.1 & 5.2, the circular path absorber damping ratio is found to be 0.13% of critical, which yields a damping coefficient of $\mu = 0.0395$. As shown in Tabs. 5.1 & 5.3, the tautochronic path absorber damping ratio is found to be 0.25% of critical, which yields a damping coefficient of $\mu = 0.0675$.

The system inertia ratio is defined as

$$\epsilon = \frac{mc^2}{J}, \tag{5.5}$$

where m is the absorber mass, and J is the inertia of the rotor. The mass m and the distance c are obtained from direct measurements and the rotor inertia J is obtained through experiment. The rotor inertia is experimentally obtained by locking down the absorbers and applying increasing levels of fluctuating torque $T_n \sin(n\theta)$, measuring the resulting steady-state rotor vibrations, $\ddot{\theta}$, at each torque level, and then computing the magnitudes of harmonics $|\ddot{\theta}|_n$ as previously described. Using a linear input-output relationship, the locked rotor inertia J_{locked} can be obtained from a line of best fit through the data points $(T_n,|\ddot{\theta}|_n)$. The locked rotor inertia J_{locked} is related to the rotor inertia via $J = J_{locked} - mc^2$, where J contains the inertia of the rotor system with no absorbers plus the inertia of the absorbers about their respective COM; see Shaw et al. [70] for more details.

Table 5.2: System parameters for the spin rig and circular path absorber; final values chosen that give the best match between experiments and theory.

Parameter	**Range**	**Value Chosen**
c (m)	0.160 ± 0.002	0.162
ρ_0 (m)	0.040 ± 0.001	0.041
ζ	0.002 ± 0.0007	0.0013
m (kg)	0.241 ± 0.001	0.241
J (kg·m^2)	0.0735 ± 0.0003	0.0732

Table 5.3: System parameters for the spin rig and tautochronic path absorber; final values chosen that give the best match between experiments and theory.

Parameter	**Range**	**Value Chosen**
c (m)	0.1783 ± 0.001	0.1785
ρ_0 (m)	0.0576 ± 0.0001	0.0576
ζ	0.003 ± 0.0006	0.0025
m (kg)	0.173 ± 0.001	0.173
J (kg·m^2)	0.0514 ± 0.0002	0.0512

5.4 Results & Discussion

The full predictive capabilities of the modeling and analysis are demonstrated by comparing simulations of the full EOM, simulations of the averaged equations, the zero damping pseudo-energy predictions, and the experimental results for both types of absorbers. The full EOM simulations use a short ramp input of the fluctuating torque, with a build-up duration of one half of a torque cycle $\theta_r = \pi/n$, as described in Chapter 4. All of the experimental results shown here are performed at a mean rotor speed of $\Omega = 350$ RPM. Percent overshoot results obtained by sweeping the individual system parameters n and Γ_i are first shown, followed by a summary of all results in which the parameters n, Γ and ξ are collapsed into χ, demonstrating the utility of the scaling.

Shown in Figs. 5.4 & 5.5 (a)-(f) are the percent overshoot results obtained from experiments using the circular path (Fig. 5.4) and near-tautochronic path (Fig. 5.5) absorbers, compared with simulations of the averaged equations and the full EOM. Figures 5.4 & 5.5

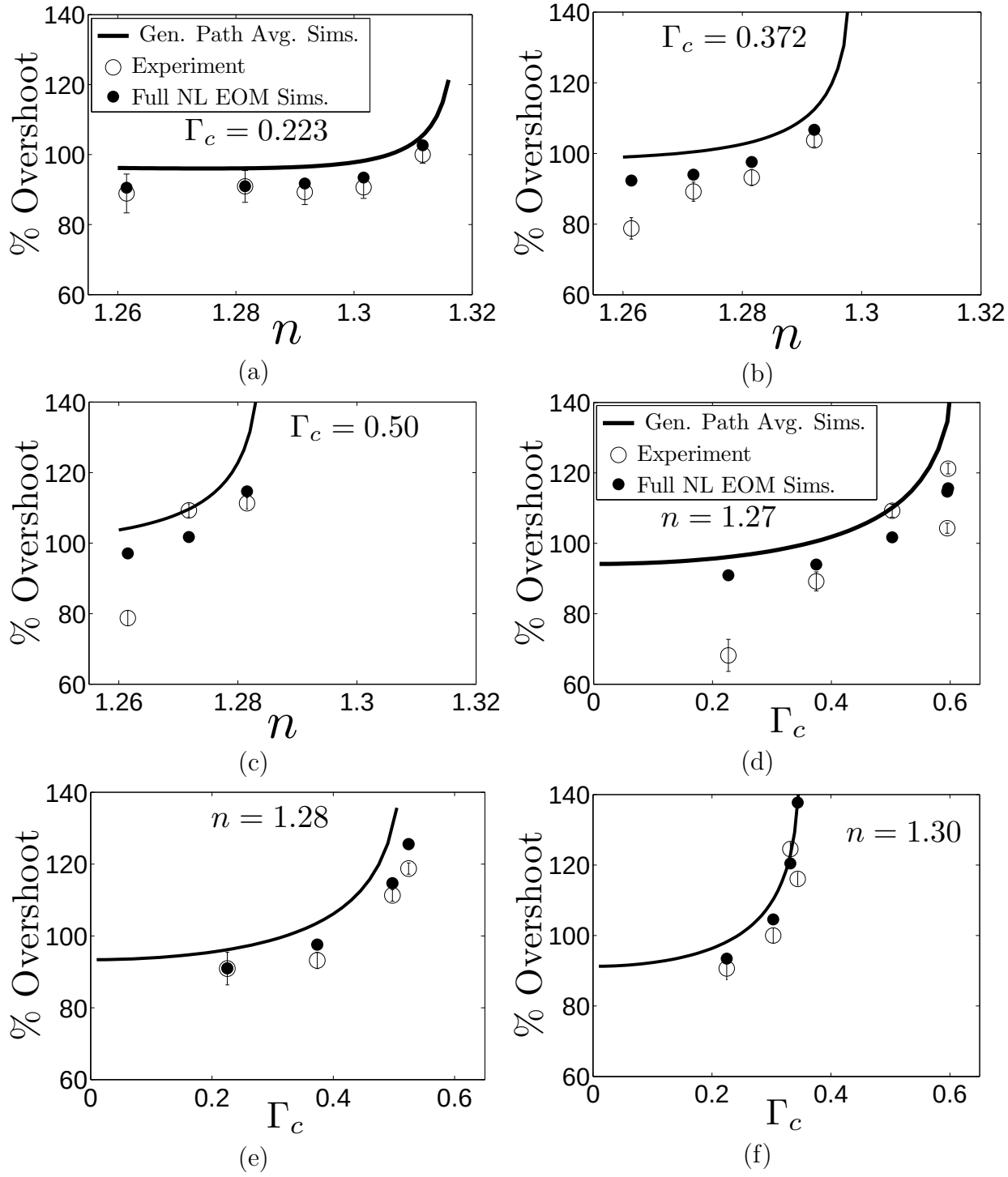

Figure 5.4: Comparison of theory and experiments for the circular path absorber. Percent overshoot vs. n for (a) $\Gamma_C = 0.223$, (b) $\Gamma_C = 0.372$, and (c) $\Gamma_C = 0.50$. Percent overshoot vs. Γ_C for (d) $n = 1.27$, (e) $n = 1.28$, and (f) $n = 1.30$.

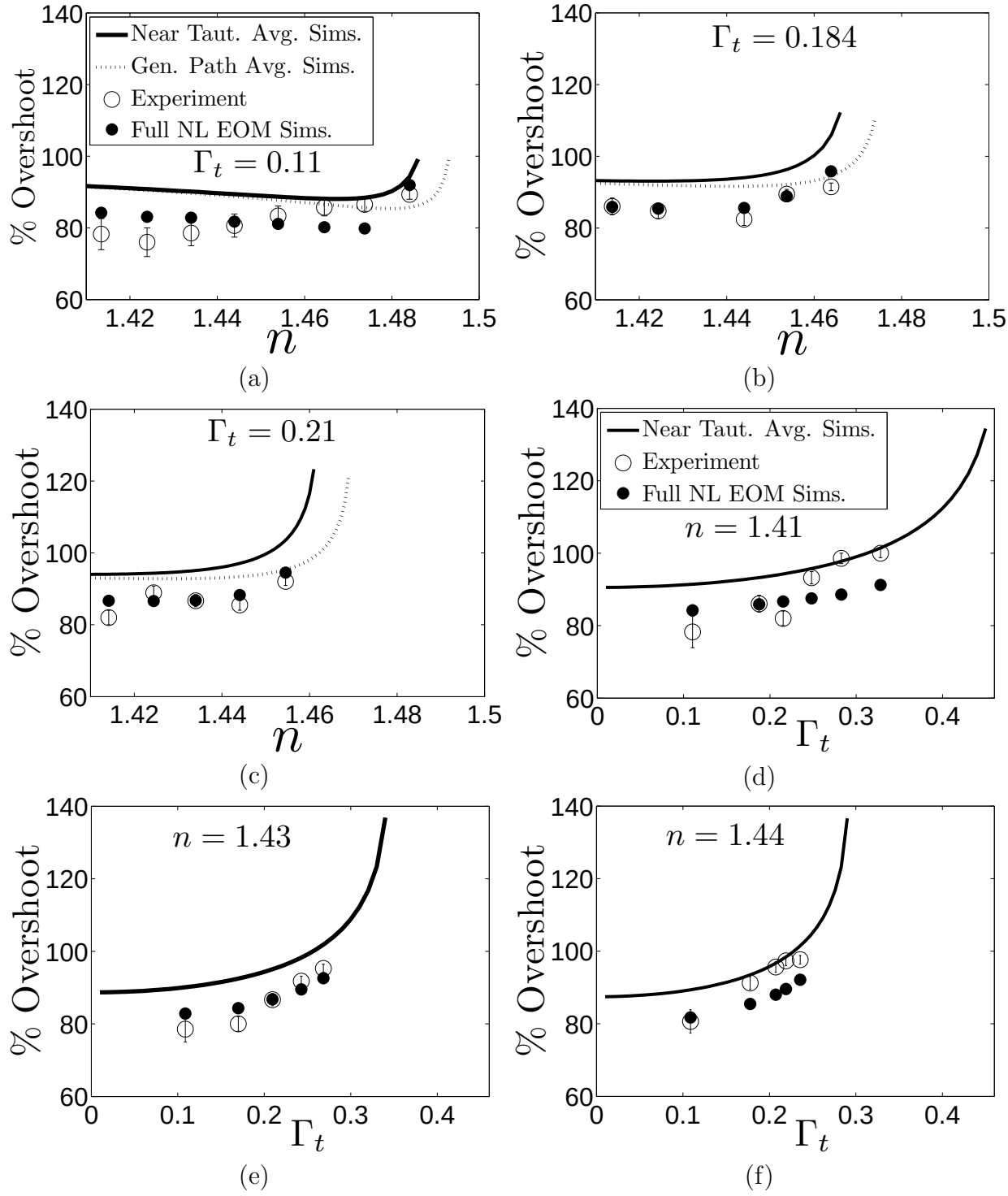

Figure 5.5: Comparison of theory and experiments for the near-tautochronic path absorber. Percent overshoot vs. n for (a) $\Gamma_t = 0.11$, (b) $\Gamma_t = 0.184$, and (c) $\Gamma_t = 0.21$. Percent overshoot vs. Γ_t for (d) $n = 1.41$, (e) $n = 1.43$, and (f) $n = 1.44$.

(a)-(c) show the effect that sweeping the torque order n has on the system overshoot for a fixed torque amplitude Γ_i. As the torque order n approaches the resonant tuning orders $\tilde{n} = 1.312$ (circular path) and $\tilde{n} = 1.449$ (tautochronic path), the overshoot increases, as expected for lightly damped systems. Figures 5.4 & 5.5 (d)-(f) show the effect that sweeping the torque amplitude Γ_i has on the system overshoot for a fixed torque order n. This shows that increasing the torque amplitude increases the percent overshoot for a fixed amount of detuning, as expected for a softening system. In comparing Figs. 5.4 & 5.5, it is seen that the observed overshoot levels are significantly less for the near-tautochronic absorber as compared to the circular path absorber, specifically, a maximum of 100% compared to 124%. This is primarily a result of the relative levels of softening between the two paths. A smaller secondary effect in the reduction of the overshoot for the near-tautochronic paths is due to the effective hardening parameter, γ, that limits the effect of the torque at moderate and large amplitudes. For paths that are near-tautochronic, and for hardening paths, the combination of the kinematic softening and the hardening parameter γ, result in a system that does not experience a jump in the system response (unless the absorbers are undertuned, which is undesirable and never used in practice) [68].

Order n sweeps are shown in Fig. 5.5 (a)-(c) for the near-tautochronic absorber, along with the pseudo-energy results for both the general path and the near-tautochronic path models, showing that the near-tautochronic path theory is more conservative than the general path theory. Due to the fact that the torques Γ_c and Γ_t are scaled differently, three additional plots would be needed to compare both pseudo-energy methods for the torque sweep of the near-tautochronic absorber; these are not shown because they demonstrate the same trend as that shown in Fig. 5.5 (a)-(c). Therefore, the near-tautochronic absorber with nonlinear

tuning $\lambda = 0.66$ is in the region where either model can provide accurate estimates of the overshoot. However, as one moves closer to a circular path, by reducing λ, the near-tautochronic theory fails to capture the amount of softening in the path and will under-predict the amount of overshoot. Similarly, moving the path towards the tautochrone, that is, increasing λ towards λ_e, the near-tautochronic theory performs the best because the general path theory is unable to capture the amount of system softening, and therefore under-predicts the overshoot[2]. As discussed in Chapter 4, for nonlinear tuning between a tautochrone and a cycloid, $\lambda_e \leq \lambda \leq 1$, both theories provide similar accuracy in the overshoot estimate for excitation orders up to $n = 3$, beyond which the softening is not accurately captured with the general path theory.

As a whole, the simulations of the full EOM in Figs. 5.4 & 5.5 perform the best at predicting the experimental system overshoot. However, the averaged equations offer the convenience of having fewer parameters and being much faster to obtain, and they are generally conservative at estimating the experimentally observed overshoot, which is useful for design. Lastly, the small amount of scatter in the experimental overshoot seen in Figs. 5.4 & 5.5, which is not observed in the simulations of the full EOM, is due to a combination of the torque sign ($+\Gamma_i$ or $-\Gamma_i$) at transition, as well as the transition time (ramp duration), both of which vary among the experimental results, but are not accounted for in the model. The scatter is not observed in the simulations of the full EOM, due to the consistency in the torque sign ($+\Gamma_i$ for all simulations) and the fixed ramp duration of $\theta_r = \pi/n$. This shows the sensitivity of the absorber overshoot to the torque profile at transition, making

[2]Recall that a tautochronic path system with λ_e is slightly softening ($\xi_t < 0$) in the near-tautochronic theory and is linear ($\xi_c = 0$) in the general path theory. For the near-tautochronic theory, the level of softening increases as the excitation order n and tuning order $\tilde{n}$ increase.

it an important design consideration that is most easily treated through simulation. The worst case torque profile is an abrupt transition with a torque acting in the direction that instantaneously slows down the rotor speed, thereby reducing the absorber restoring force and resulting in more overshoot. For non-zero initial conditions, this scenario can be made even worse, depending on the dynamic state of the absorber at the time of the transition.

Shown in Fig. 5.6 (a) & (b) is the percent overshoot obtained from the general path pseudo-energy solution, simulations of the averaged equations (with damping), simulations of the full EOM, and experimental results, for the circular path absorber (Fig. 5.6 (a)) and the near-tautochronic path absorber (Fig. 5.6 (b)), which are collapsed onto the single system parameter χ_C. As expected, the circular path absorbers jump shortly beyond the point $\chi^\star$, where the jump offset is due to damping. In fact, the circular path absorber jumps at very small torque levels when the excitation order reaches the pendulum tuning order $n \approx \tilde{n} = 1.312$. In contrast, the near-tautochronic absorbers do not jump, but instead reach their physical limits. In fact, they run well beyond their tuning order $\tilde{n} = 1.449$, before they began to limit out at $n = 1.48$. As noted previously, it is observed that the full EOM perform the best at predicting the experimentally measured overshoot, while the averaged equations provide a mostly conservative estimate. In addition, not a single experimentally measured overshoot value was observed to be above the (undamped) pseudo-energy curve, making this curve a useful upper bound for the overshoot that one would expect during a cylinder deactivation event. An attractive feature of this upper bound is that it is the solution of a cubic equation, which has a closed form, and it depends on the single parameter χ_C.

Lastly, the introduction of the damping parameter D_i offers a more accurate bound on the overshoot. However, recall that the scaled damping coefficients D_i depend on the absorber

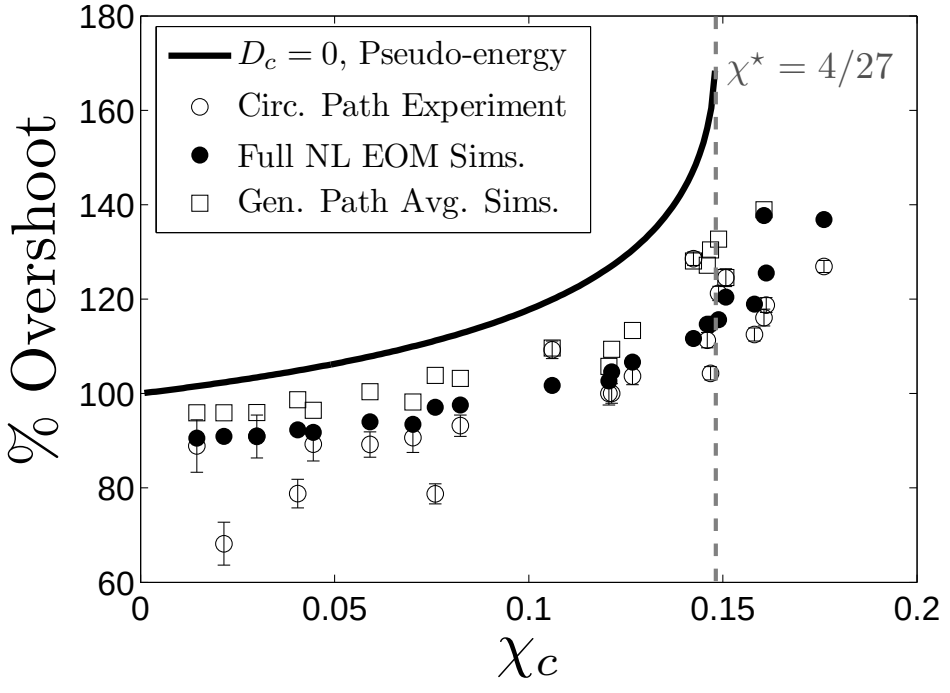

(a)

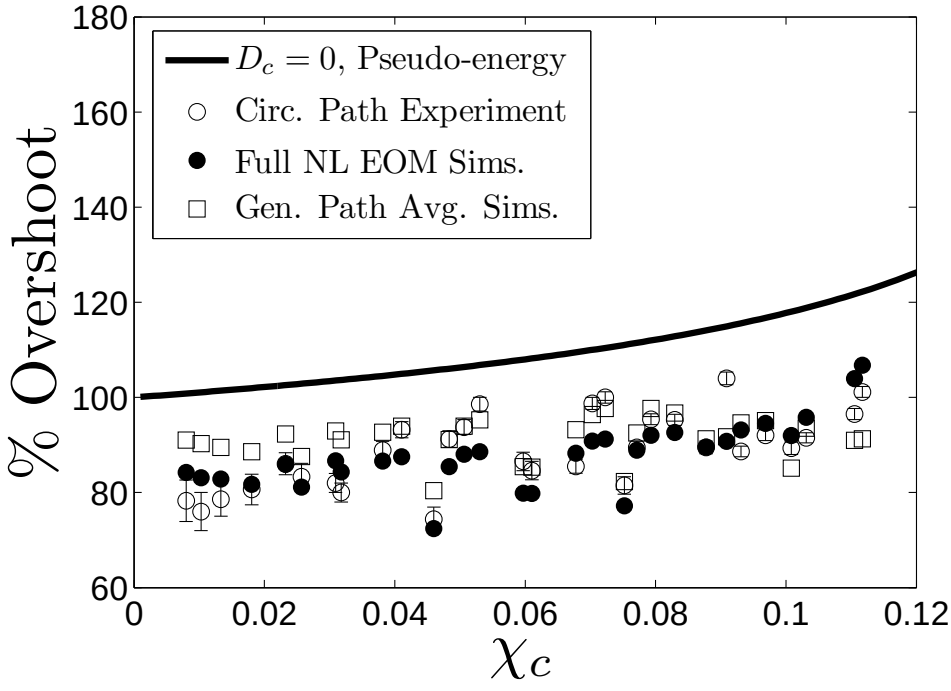

(b)

Figure 5.6: Comparisons of theory and experiments for the (a) circular path absorber and the (b) near-tautochronic path absorber; percent overshoot vs. χ_c.

damping coefficients μ, the excitation order n, the tuning order $\tilde{n}$, and the inertia ratio ϵ, so that one cannot show a single overshoot curve versus χ that represents a fixed level of damping. Fig. 5.7 shows three curves for various levels of damping, along with the same experimental data presented in Fig. 5.6. The three curves are the zero damping general path pseudo-energy result, $D_C = 0$, along with the curves generated by simulating the damped general path averaged equations. The damping coefficient D_i in the damped simulations is computed by using the values of the damping ratio that bound the range of uncertainty (given in Tabs. 5.2 & 5.3) for each absorber, as well as the smallest (largest) excitation order n used in the experiments which will minimize (maximize) D_i. For the circular path absorber, the damping ratios used are $\zeta = 0.0013$ and $\zeta = 0.0025$, with excitation orders of $n = 1.261$ and $n = 1.312$, which yield $D_C = 0.036$ and $D_C = 0.152$, respectively. For the near-tautochronic path absorber, the damping ratios used are $\zeta = 0.0024$ and $\zeta = 0.0036$, with excitation orders of $n = 1.413$ and $n = 1.485$, which yield $D_C = 0.062$ and $D_C = 0.193$, respectively. It is seen that the curves that account for damping bound most of the experimentally observed overshoot data, thus providing a more precise prediction. Such results can be used to develop more aggressive absorber designs, provided estimates of the absorber damping are known.

5.5 Conclusions

The results presented here demonstrate the validity of the analytical predictions in Chapter 4, and provide the tools required for estimating, with confidence, absorber overshoot for a wide range of system parameters. While the experimental results presented focused on zero initial conditions, the analysis is quite general and is able to predict overshoot levels for arbitrary initial conditions. In this experimental study, two types of absorbers were used, one

with a circular path ($\lambda = 0$) and the other with a near-tautochronic path ($\lambda = 0.66$). These two paths span about 2/3 of the parameter range for the Denman family of epicycloidal paths. Both paths are nonlinearly softening, which are the most sensitive to changes in the excitation parameters that lead to transient response; this makes them well suited for testing the theoretical predictions. The experimental results show that numerical solutions of the full equations of motion perform the best at capturing the observed overshoot, while the general path and near-tautochronic path results obtained by simulating the damped averaged equations were mostly conservative, but still quite accurate. In fact, the general path results also worked well at predicting the response of the near-tautochronic absorbers, but the reverse was not true, as expected. The pseudo-energy method provides a quick and convenient method for determining a useful upper bound for absorber overshoot, which for the general path is available in closed form and depends on a single system parameter χ_C. For the near-tautochronic paths, the pseudo-energy method depends on two parameters, and requires numerical solution for the root of a single equation involving elliptic functions. However, the overshoot for most such paths, with small damping, is essentially that of a linear system, that is, about 100%. It is worth noting that it appears that the general path results can be used to estimate absorber overshoot for most practical absorber designs [46]. However, the full near-tautochronic results are required for excitation orders greater than $n = 3$ that will operate at large amplitudes. Lastly, if estimates of the absorber damping are known, an accurate bound on the overshoot can be obtained by simulations of the averaged equations, and this allows for more aggressive absorber designs when compared to using the conservative upper bound obtained from the pseudo-energy method.

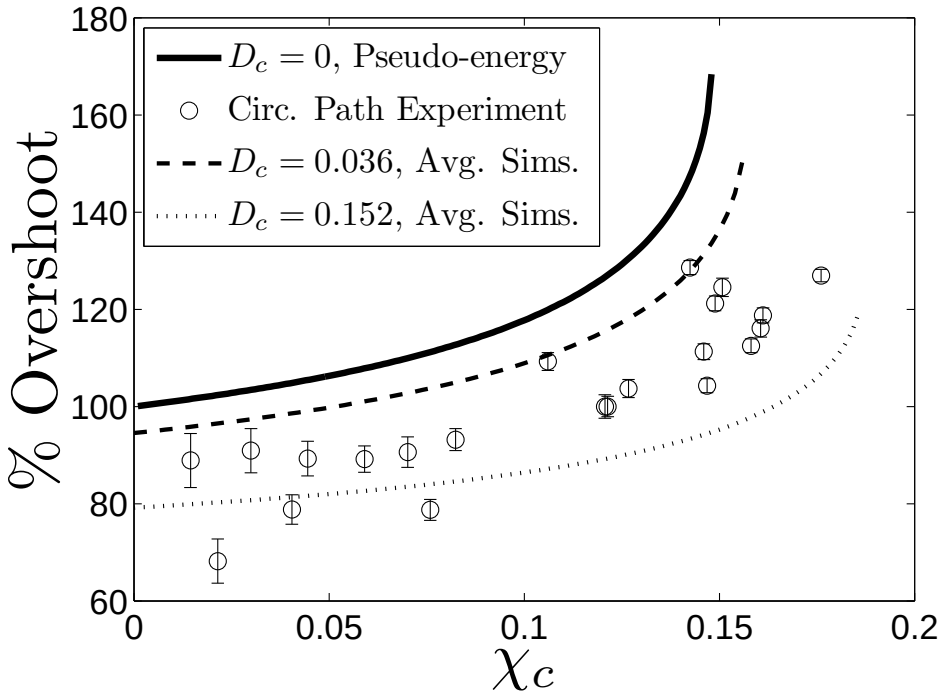

(a)

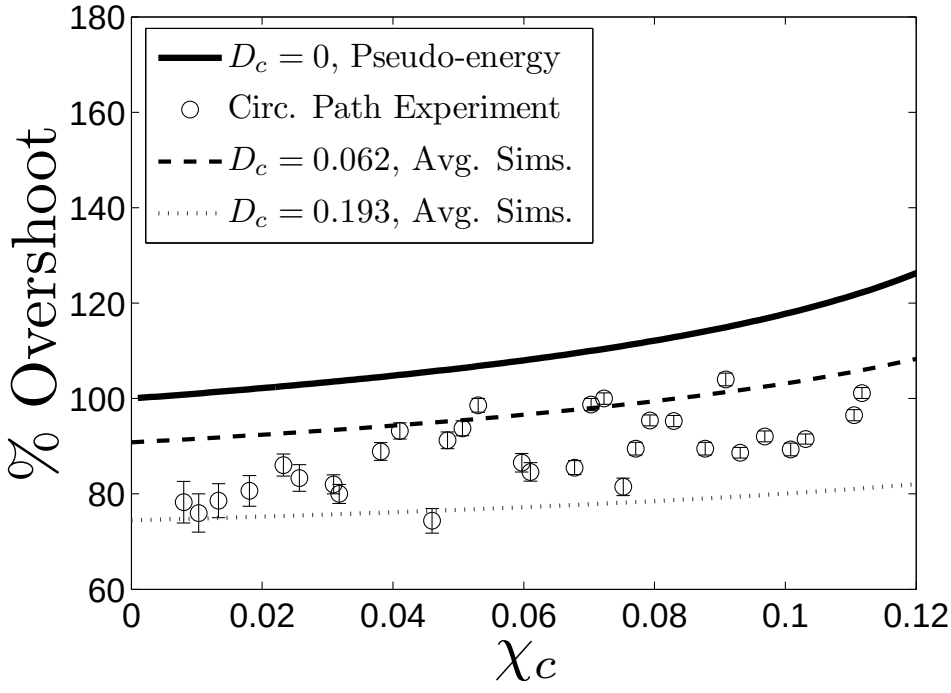

(b)

Figure 5.7: Bounding the experimental data using simulations of the damped general path averaged equations for the (a) circular path absorber and (b) the near-tautochronic path absorber; percent overshoot vs. χ_c.

Chapter 6

Conclusions and Directions for Future Work

The first part of this study considering improving the absorber system model by accounting for the rollers which suspend the pendulum mass in bifilar absorber configurations. This analysis led to the discovery of a tautochronic absorber path that accounts for roller inertia, a previously unknown result. It was shown that when the rollers are accounted for in the linear tuning $\tilde{n}$, the tautochronic path with rollers results in a forced absorber response that is slightly more hardening than the roller-free absorber path. In addition, a perturbation analysis extracted the leading order roller influences on the absorber kinematics, in order to determine the accuracy of the previous roller-free assumptions on the absorber's tuning parameters $\tilde{n}$ and λ. The perturbation results show that for practical roller sizes, the rollers have a very small influence on the nonlinear tuning. Therefore, for the sizes of rollers typically in use, one needs to include their effects only in the linear tuning in order to achieve satisfactory performance.

The roller investigation employed a near tautochronic path scaling [11, 14, 68, 70] on the full equations of motion in order to perform the perturbation analysis, and for these paths the dominant nonlinearity arises from kinematic coupling to the rotor. The other type of scaling employed in this work is the general path scaling [5, 26, 52, 53], which applies in cases where the dominant nonlinearity arises from the absorber path. The resulting approximate models obtained from these two scalings have a very similar form and can be analyzed in a similar manner. The general path results involve polynomial nonlinearities arising from the path, whereas the near tautochronic path results involve elliptic function nonlinearities that arise from the absorber/rotor coupling.

At the heart of the model for the coupled absorber/rotor system is a harmonically forced (near resonance) nonlinear oscillator, and the analysis of the transient response starts with an investigation of the harmonically forced Duffing oscillator with cubic stiffness nonlinearity. The major contributions of this study include an approximate method to compute the nonlinear percent overshoot, based on a unique scaling of the position and independent variable that significantly simplifies the oscillators parameter dependence. Specifically, the excitation amplitude, the system nonlinearity, and the order detuning can be combined into a single parameter, χ. This parameter, and a damping parameter D, completely dictate the response. The overshoot results derived here are quite fundamental and, to the author's knowledge, original. The nonlinear percent overshoot method makes use of the system's averaged equations, which yield an integral of motion in the undamped ($D = 0$) case [71], by which the amplitude and phase of the system response are related to χ and the initial conditions. This integral of motion is quartic in amplitude for non-zero initial conditions and cubic in amplitude for zero initial conditions, and the roots can be found in closed form. The

roots give phase space trajectories that are a function of the response phase, χ, and initial conditions. These transient trajectories contain the peak amplitudes and, for bistable systems, the ultimate steady state response achieved, both of which are important to absorber design.

The scaling employed here reduces the averaged system to two parameters, χ, described above, and D, which involves the damping. Thus, the undamped results, which provide a useful bound for the overshoot in lightly damped systems, depend only on χ. With the presence of damping, the averaged equations can no longer be integrated exactly, however, an approximate integral of motion for small damping is possible, and this computation is summarized in Appendices G & H. The payoff, in terms of analytical approximation and its accuracy, is small in comparison with the extensive nature of these calculations, and thus it appears to be more efficient to simply obtain the damped overshoot by simulating the averaged equations with damping. The undamped results provide quick estimates of the overshoot for CPVAs, which must be designed to not exceed specified amplitudes, even during abrupt startups, making them of great practical value to absorber design. Additionally, for the case of tautochronic absorbers [11, 14, 68, 70], the system nonlinearities are much more complicated than the cubic term in the Duffing equation, yet the averaged equations are integrable in the undamped case, so that similar predictive results can be achieved for that system. Furthermore, this percent overshoot approach has also been applied to the case of parametric resonance and it has been found to produce simpler formulas for the overshoot than those given here. In fact, for the case of near zero initial conditions (i.e. $p_0 \approx 0$) it is remarkably found that the percent overshoot is simply $100(\sqrt{2}-1)$, and is therefore independent of the system parameters contained. Completion of these results, which include

experimental evidence of the constant overshoot for near zero initial conditions, and an outline for computing the overshoot for non-zero initial conditions [46], are still in progress. These extensions suggest that the pseudo-energy approach may be quite general for weakly nonlinear systems of a general form, and also possibly for classes of conservative, strongly nonlinear systems with periodic excitation.

Another contribution of this work is that, for the first time, the general path [5, 26, 52, 53] and near tautochronic path [11, 14, 68, 70] perturbation results are formulated together in a single, compact framework. This is useful for all investigations, and is used here to solve the nonlinear overshoot problem. For the general path case, with negligible damping, the formulation boils down to previously mentioned closed form expression (specifically, roots of a cubic or quartic equation, depending on initial conditions) that depends on a single parameter. For the near tautochronic path case, the overshoot estimate for undamped systems depends on two parameters, and requires finding the root of an equation that involves elliptic functions. For all path types, more accurate estimates that account for damping are available via simulation of the averaged equations.

An experimental study of the transient response of pendulum vibration absorbers during a simulated cylinder deactivation event demonstrated the validity of the analytical approximations. While these results focused on zero initial conditions, the analysis is quite general and is able to predict overshoot levels for absorbers with all paths used in practice. In the experiments, two types of absorbers are used, including a circular path absorber ($\lambda = 0$) and a near tautochronic path absorber ($\lambda = 0.66$); these paths span about 2/3 of the total range in the Denman family. Both paths are in the softening region of the family, which is most sensitive to changes in the excitation parameters and the torque profile at startup, which

makes them well suited for testing the theoretical predictions. The experimental results from both absorbers show that the equations of motion perform best at capturing the observed overshoot, while the averaged equations were mostly conservative, but still quite accurate. In fact, the general path averaged equations worked well at predicting the response of the near tautochronic absorbers, except at large amplitudes, but the reverse was not true, as expected. The pseudo-energy method provides a quick and simple method for determining a useful upper bound for absorber overshoot. This result is available in closed form for the general path and depends on a single system parameter χ_C, and it appears that the general path results can be used to estimate absorber overshoot for most practical absorber designs. Lastly, if estimates of the absorber damping are known, an accurate bound on the overshoot can be obtained by simulation of the averaged equations, and this allows for slightly more aggressive absorber designs, when compared to using the upper bound obtained from the pseudo-energy method.

A major issue yet to be explored is the possibility of non-synchronous transient dynamics in multi-absorber systems. A preliminary experimental investigation of transient dynamics using two circular path absorbers was carried out during the course of the present work. An interesting behavior, observed in both experiments and simulations of absorbers with slightly different levels of damping, is a transient response wherein the two absorbers start at zero, then exchange energy in a non-synchronous manner as they begin to settle down, but ultimately end up in a near-synchronous response, with the difference in steady-states attributed to the different damping values. Such a response, from experiments and simulations, is shown in Fig. 6.1 (a) & (b). This occurred at a torque order $n = 1.292$, where the absorber motion was initially synchronous, until a critical torque amplitude was reached. As

the torque amplitude was incremented further, the non-synchronous transient motion shown in Fig. 6.1 (a) & (b) was observed, until a level beyond which the absorbers eventually jumped to the upper branch steady-state, as expected. The simulation shown in Fig. 6.1 (b), using the experimentally measured system parameters, captures this bifurcation very accurately, which is believed to be a result of the difference in the values of the equivalent viscous damping coefficients μ_i between the two absorbers, since the absorbers have nearly identical tuning orders $\tilde{n} = 1.309$. Also, as the difference in damping values was decreased in simulations, this bifurcation disappeared. In addition, when the torque order was increased to $n = 1.302$, the steady-state behavior observed by Nester was reproduced [52–54]. Specifically, at near resonance excitation $n \approx \tilde{n}$, one absorber was in an inactive state (near zero steady-state amplitude), while the other absorber was active. The transient response leading to this must, of course, be non-synchronous. As shown in Fig. 6.2 (a), after the first beat cycle, the transient amplitude response shows the absorber with larger damping (black) decays to a near zero state, while the other grows to nearly twice the predicted synchronous steady-state amplitude. A simulation using the experimentally measured parameters is shown in Fig. 6.2 (b), where it is seen that differences in viscous damping cannot fully capture this behavior. However, the addition of Coulomb damping may capture this behavior since Vidmar [75] observed that Coulomb damping plays a more prominent role at smaller amplitudes, i.e, less than 10^{O} swing angle, in these circular path absorbers. As the torque amplitude was incremented further at order $n = 1.302$, a non-synchronous motion similar to that observed in Fig. 6.1 (a) & (b) was observed, until the absorbers eventually jumped to the upper branch. To date, this bifurcation has not been captured analytically, but this investigation is underway. This problem is more easily tackled by performing a

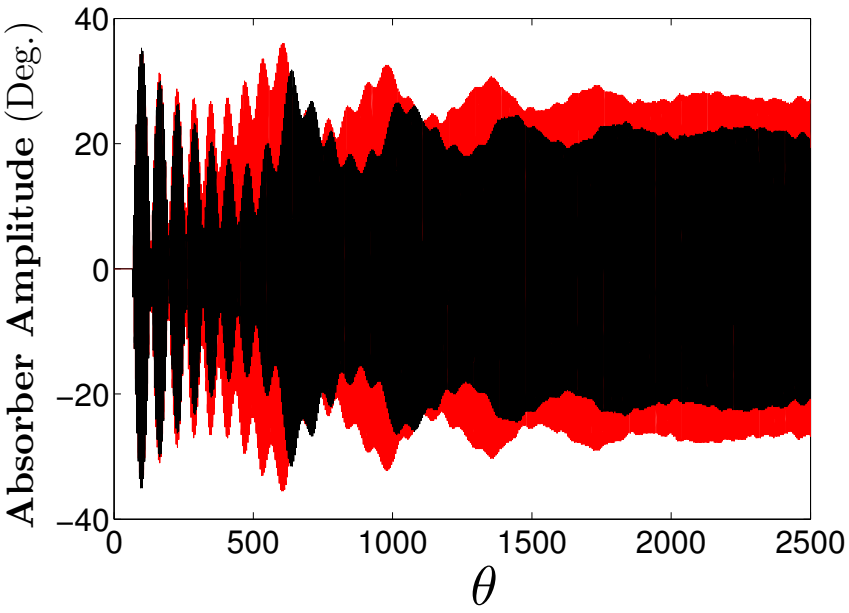

(a)

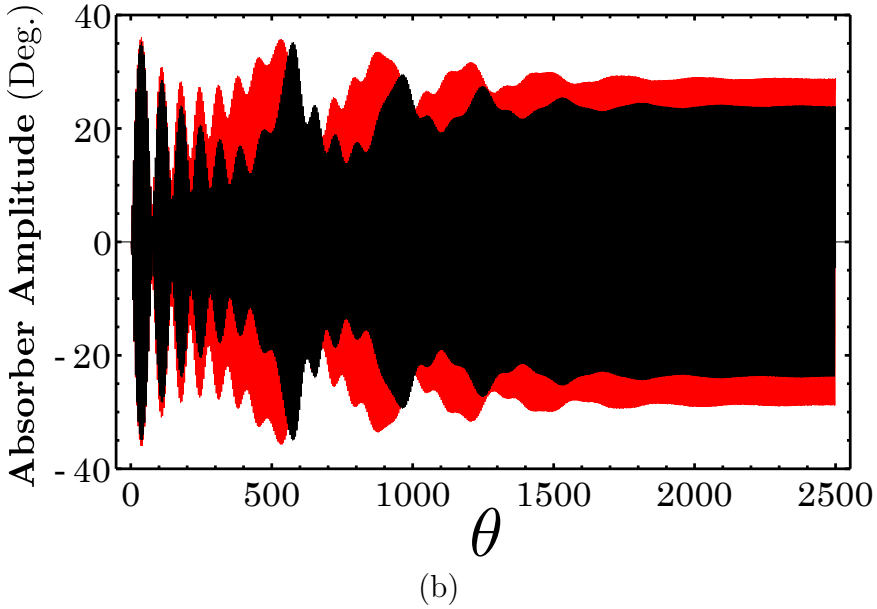

(b)

Figure 6.1: Non-synchronous transient motion to a steady-state near-synchronous response using two circular path absorbers at torque order $n = 1.292$: (a) experiment and (b) simulation. Parameter values used for simulation: $\tilde{n} = 1.309$ (both absorbers), $\zeta_1 = 0.002$ (response shown in red), $\zeta_2 = 0.0035$ (response shown in black), $T_0 = 1.069$ Nm, $T_n = 2.919$ Nm, $\Omega = 36.652$ rad/s, $J = 0.0636$ kg·m^2, $m = 0.241$ kg (both absorbers), $c_c = 0.162$ m (both absorbers, see Tab. 5.2), $\rho_{0c} = 0.041$ m (both absorbers, see Tab. 5.2), and a ramp of half a torque cycle in of the fluctuating torque.

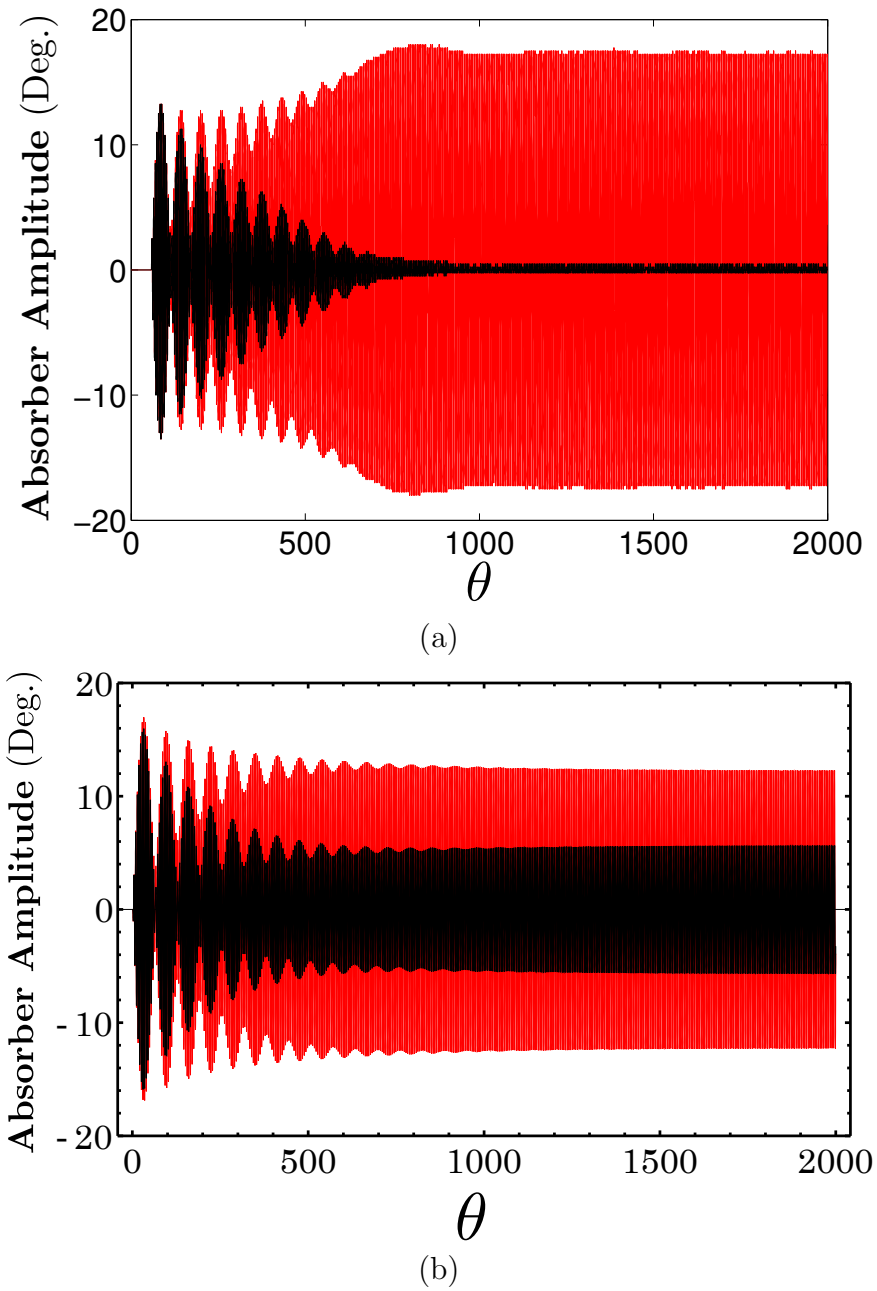

Figure 6.2: Non-synchronous transient motion to a non-synchronous steady-state at torque order $n = 1.302$: (a) experiment and (b) simulation. Parameter values used for simulation: $\tilde{n} = 1.309$ (both absorbers), $\zeta_1 = 0.0013$ (response shown in red), $\zeta_2 = 0.0042$ (response shown in black), $T_0 = 0.937$ Nm, $T_n = 1.40$ Nm, $\Omega = 36.652$ rad/s, $J = 0.0636$ kg·m^2, $m = 0.241$ kg (both absorbers), $c_c = 0.162$ m (both absorbers, see Tab. 5.2), $\rho_{0c} = 0.041$ m (both absorbers, see Tab. 5.2), and a ramp of half a torque cycle in of the fluctuating torque.

steady-state stability analysis along similar lines to that performed in [6, 68], before a transient stability analysis is considered. Following the stability analysis using circulant matrices in [68], one could investigate the transient stability of such a response. Of course, one would have to assume identical absorber systems with zero damping, but such results may provide useful bounds for lightly damped systems.

Other topics for future consideration include: more gradual transitions, transient responses of systems with absorbers tuned to multiple orders, and a more detailed investigation of the transition during cylinder deactivation, using more realistic engine torque data. Along these lines is the design of torque profiles that minimize overshoot, such as the ramp used in Chapter 4. An example of an experimental run demonstrating this idea is shown in Fig. 6.3, which results in significantly less overshoot when compared to the step input. A similar approach that may be easier to physically implement involves discretely jumping the excitation order between off-resonant and resonant during a transition between these two cases, by turning on and off cylinders, thus allowing the absorber amplitude to gradually build up. Analysis of these behaviors will generally require simulations, but the effort involved in a detailed parameter study can be minimized by making use of the rescaling developed in this work, and the averaged equations, which are much faster to simulate.

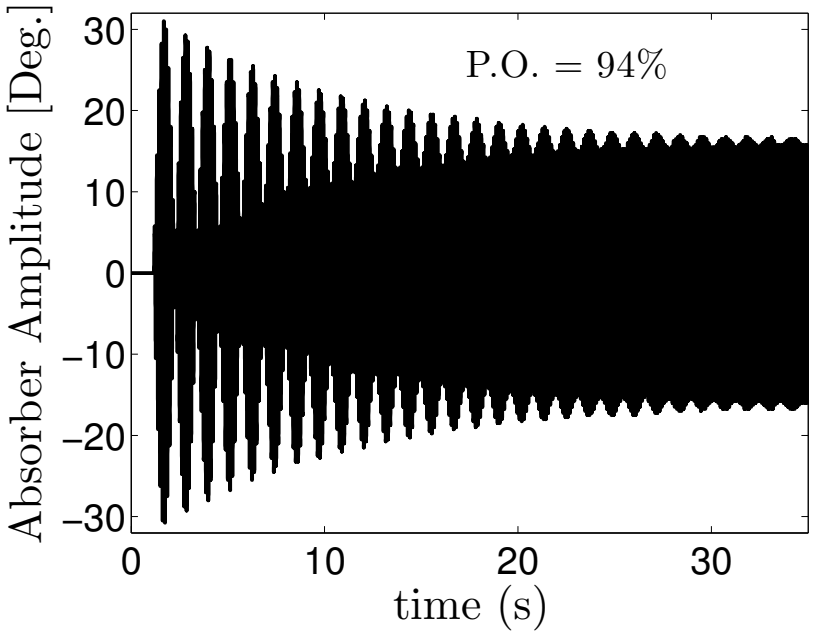

(a)

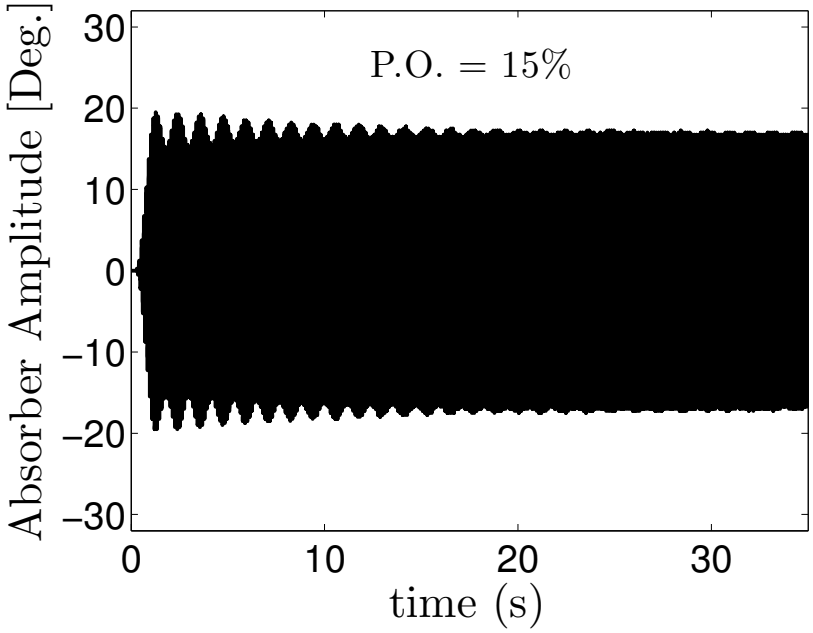

(b)

Figure 6.3: Experimental comparison of the transient overshoot of a circular path absorber when forced at $n = 1.26$ using two types of fluctuating torque inputs that have the same magnitude but a different ramp duration. (a) Response to a near step input of the torque, resulting in an overshoot of 94%. (b) Response to a ramp input of the torque with a duration of 10 torque cycles, resulting in an overshoot of 15%.

APPENDICES

Appendix A

Order ϵ^2 terms

The order ϵ^2 terms for the rotor equation of motion are given by

$$
\begin{aligned}
&-\epsilon^2\Bigg(-\mu\nu g(s)s' + 4\xi a^2\Bigg(\nu\nu' - \frac{1}{2a}\nu\nu' s' - \frac{1}{2a}\nu^2 s''\Bigg)+ \\
&+ 4\delta\Bigg(\nu\nu'\Big(h^2 + \ell^2 + \frac{1}{4}r_P^2(s) + \ell y_p(s) + \frac{1}{4}g(s)s' - \frac{1}{2}\ell s'\frac{\partial x_P(s)}{\partial s}\Big)+ \\
&+ \nu^2\Big(\frac{1}{4}\frac{\partial r_P^2(s)}{\partial s}s' + \frac{1}{4}\frac{\partial g(s)}{\partial s}s'^2 + \ell s'\frac{\partial y_P(s)}{\partial s} + \frac{1}{4}g(s)s'' + \\
&- \frac{1}{2}\ell\frac{\partial x_P(s)}{\partial s}s'' - \frac{1}{2}\ell s'^2\frac{\partial x_P^2(s)}{\partial s^2}\Big)\Bigg)\Bigg),
\end{aligned}
$$

which completes the rotor equation of motion (2.4), since there are no higher order terms.

Appendix B

Pendulum Path Details

Here we follow the path formulation of Denman [17], in which the local radius of path curvature ρ is described by $\rho^2 = \rho_0^2 - \lambda^2 S^2$. Denman derives the position of the pendulum in terms of rotating Cartesian coordinates X_P and Y_P, which can be used to find $R_P^2 = X_P^2 + Y_P^2$. The expressions for X_P and Y_P are

$$X_P = \frac{\rho_0}{1-\lambda^2}\left(\sin\left(\frac{1}{\lambda}\sin^{-1}\left(\frac{\lambda S}{\rho_0}\right)\right)\cos\left(\sin^{-1}\left(\frac{\lambda S}{\rho_0}\right)\right)+ \right. \\ \left. - \frac{\lambda^2 S}{\rho_0}\cos\left(\frac{1}{\lambda}\sin^{-1}\left(\frac{\lambda S}{\rho_0}\right)\right)\right), \tag{B.1}$$

and

$$Y_P = -c - \frac{\rho_0}{1-\lambda^2}\left(\cos\left(\frac{1}{\lambda}\sin^{-1}\left(\frac{\lambda S}{\rho_0}\right)\right)\cos\left(\sin^{-1}\left(\frac{\lambda S}{\rho_0}\right)\right)+ \right. \\ \left. + \frac{\lambda^2 S}{\rho_0}\sin\left(\frac{1}{\lambda}\sin^{-1}\left(\frac{\lambda S}{\rho_0}\right)\right)-1\right). \tag{B.2}$$

Using trigonometric relations one can obtain the following expression,

$$\cos\Big(\sin^{-1}\Big(\frac{\lambda S}{\rho_0}\Big)\Big)=\sqrt{1-\Big(\frac{\lambda S}{\rho_0}\Big)^2}. \tag{B.3}$$

If one substitutes equation (B.3) into equations (B.1) and (B.2), normalizes the path expressions and the arc length S by c, and makes use of equation (2.5) to replace ρ_0 with $\tilde{n}_0$, the following non-dimensional path expressions are obtained,

$$x_P = \frac{1}{1-\lambda^2}\Bigg(\sin\Big(\frac{1}{\lambda}\sin^{-1}\Big(\lambda(1+\tilde{n}_0^2)s\Big)\Big)\sqrt{\Big(\frac{1}{1+\tilde{n}_0^2}\Big)^2-\lambda^2 s^2}+ \\ -s\lambda^2\cos\Big(\frac{1}{\lambda}\sin^{-1}\Big(\lambda(1+\tilde{n}_0^2)s\Big)\Big)\Bigg), \tag{B.4}$$

and

$$y_P = -1+ \\ -\frac{1}{1-\lambda^2}\Bigg(\cos\Big(\frac{1}{\lambda}\sin^{-1}\Big(\lambda(1+\tilde{n}_0^2)s\Big)\Big)\sqrt{\Big(\frac{1}{1+\tilde{n}_0^2}\Big)^2-\lambda^2 s^2}+ \\ +s\lambda^2\sin\Big(\frac{1}{\lambda}\sin^{-1}\Big(\lambda(1+\tilde{n}_0^2)s\Big)\Big)-\frac{1}{1+\tilde{n}_0^2}\Bigg). \tag{B.5}$$

Appendix C

Averaging Integrals

The integrals that result from the averaging process, and are not available in convenient closed form, are defined by

$$F_1(z) = \frac{1}{2\pi}\int_0^{2\pi} \sin^2(x)\sqrt{1-\tilde{n}_0^2(1+\tilde{n}_0^2)z^2\cos^2(x)}\; dx, \tag{C.1}$$

$$F_2(z) = \frac{1}{2\pi}\int_0^{2\pi} \cos^2(x)\sqrt{1-\tilde{n}_0^2(1+\tilde{n}_0^2)z^2\cos^2(x)}\; dx, \tag{C.2}$$

and

$$M(z) = \frac{1}{2\pi}\int_0^{2\pi} \cos(x)\sin\left(\frac{1}{\lambda_{e0}}\sin^{-1}\left(z\tilde{n}_0\sqrt{1+\tilde{n}_0^2}\cos(x)\right)\right)\; dx. \tag{C.3}$$

Appendix D

Steady-State Amplitudes

The steady state amplitudes for branch **A**, branch **C**, and saddle branch **B** are given by three of the six possible roots to equation (3.9) when $\chi \neq 0$. The three roots are as follows,

$$p_A(\chi, D) = \frac{1}{\sqrt{3\chi}}\sqrt{1 + \frac{1}{8}(1 + i\sqrt{3})(3D^2 - 4)\lambda^{-1/3} + \frac{1}{8}(1 - i\sqrt{3})\lambda^{1/3}}, \tag{D.1}$$

$$p_C(\chi, D) = \frac{1}{\sqrt{3\chi}}\sqrt{1 + \frac{1}{4}(4 - 3D^2)\lambda^{-1/3} + \frac{1}{4}\lambda^{1/3}}, \tag{D.2}$$

$$p_B(\chi, D) = \frac{1}{\sqrt{3\chi}}\sqrt{1 - \frac{1}{8}(1 - i\sqrt{3})(3D^2 - 4)\lambda^{-1/3} - \frac{1}{8}(1 + i\sqrt{3})\lambda^{1/3}}, \tag{D.3}$$

where

$$\lambda = 2(27\chi - 4 - 9D^2) + 3\sqrt{3}\sqrt{D^6 + 8D^2(D^2 + 2 - 9\chi) + 4\chi(27\chi - 8)}. \tag{D.4}$$

The root p_C is valid for all values of $\chi \neq 0$. The roots p_A and p_B are valid in the bistable region $\chi \in (\chi_1^\star, \chi_2^\star)$. This range is determined by the conditions on χ for these roots to be

real, specifically,

$$\chi_1^\star = \frac{1}{54}\left(8 + 18D^2 - \sqrt{\left(4 - 3D^2\right)^3}\right), \tag{D.5}$$

$$\chi_2^\star = \frac{1}{54}\left(8 + 18D^2 + \sqrt{\left(4 - 3D^2\right)^3}\right). \tag{D.6}$$

For the undamped system results, roots are simply evaluated at $D = 0$. The linear ($\xi = 0,\ \chi = 0$) steady state forced response steady is recovered from equation (3.9), and is given by $\bar{p} = \frac{1}{\sqrt{4+D^2}}$.

Appendix E

Transient Response Symmetry

Similar to the steady state amplitude response, the transient amplitude response also possesses a symmetry that allows one to use the derived results to capture the case when $p < 0$, which arises when $\sigma < 0$ in the rescaled system. To see this, substitute $p = -k$ into equation (3.12) to obtain

$$-\chi k^4 + k^2 - k\cos(\Phi) = c_1, \tag{E.1}$$

which, upon replacing Φ with $\Phi + \pi$, one obtains

$$-\chi k^4 + k^2 + k\cos(\Phi) = c_1, \tag{E.2}$$

which is the same as equation (3.12). Therefore the transient trajectories for $p < 0$ are the same as those for $p > 0$ with a phase shift of $\Phi + \pi$. The percent overshoot results for $p_0 < 0$ are obtained by computing c_1 using initial conditions ($|p_0|$, $\Phi_0 + \pi$). The resulting c_1 is then used in the roots given in equations (F.1) and (F.2) to find the peak amplitude p_{max} for the overshoot calculation.

Appendix F

Undamped Transient Response Amplitudes

Here we give the full analytical results needed for the percent overshoot calculation given in equation (3.11). The percent overshoot calculation uses the peak transient amplitude and the steady state amplitude for a given χ and initial conditions (p_0, Φ_0). The two roots of the transient equation (equation (3.12)) that contain the peak amplitudes about steady states **A** and **C**, as explained in the text, are given by,

$$p_1(\chi, \Phi, c_1) = \frac{1}{2\sqrt{3\chi}} \left(\sqrt{2+\kappa} - \left(4 - \kappa + \frac{6\sqrt{3\chi}\cos(\Phi)}{\sqrt{2+\kappa}} \right)^{1/2} \right), \tag{F.1}$$

$$p_2(\chi, \Phi, c_1) = \frac{1}{2\sqrt{3\chi}} \left(\sqrt{2+\kappa} + \left(4 - \kappa + \frac{6\sqrt{3\chi}\cos(\Phi)}{\sqrt{2+\kappa}} \right)^{1/2} \right), \tag{F.2}$$

where κ is

$$\kappa = \beta \left(\frac{2}{\alpha} \right)^{1/3} + \left(\frac{\alpha}{2} \right)^{1/3},$$

and β and α are defined as follows,

$$\begin{aligned}\beta =& 1 + 12c_1\chi,\\ \alpha =& \gamma + \sqrt{\gamma^2 - 4\beta^3},\\ \gamma =& 9\chi\Big(3\cos^2(\Phi) + 8c_1\Big) - 2.\end{aligned}$$

The constant c_1 is determined by the initial conditions (p_0, Φ_0) and χ, specifically,

$$c_1(\chi, p_0, \Phi_0) = -\chi p_0^4 + p_0^2 + p_0\cos(\Phi_0). \tag{F.3}$$

The roots p_1 and p_2 give transient trajectories as a function of the relative phase Φ, and for $D = 0$ the peak occurs at $\Phi = 0$ or $\Phi = \pi$, depending on the system parameters χ and the initial conditions (p_0, Φ_0). With the transient amplitude roots given here and the steady state amplitude roots given in Appendix D, one can formulate the percent overshoot about equilibria **A** and **C** by following the procedure given in Section 3.3.1.

Appendix G

Amplitude Correction for Small Damping

It is now of interest to investigate a correction to the percent overshoot calculation for the case of small damping. As mentioned earlier, no exact integral of motion is known for equations (3.6) and (3.7) when $D \neq 0$, however, an approximate solution for the case of small damping $D << 1$ will be derived. The approach used here follows that of Denman's [18], who expands the constant of motion in a power series using the damping coefficient D and derives n partial differential equations to be solved at each order D^n. This expansion will only be solved up to first order in D, where the D^0 order solution will recover the result derived in equation (3.12) and the D^1 solution is summarized in Appendix H. The resulting constant of motion which is corrected for small damping is then compared with simulations of the average equations (equations (3.6) and (3.7)) to show its accuracy. This correction only provides an analytical result for the constant of motion, analytical results for the peak amplitude p_{max} of this constant of motion are intractable and these amplitudes are obtained

numerically and then used in the percent overshoot calculation.

Following the work of Denman's [18], one can determine a corrected constant of motion for the damped system by expanding the constant of motion $\Psi(p, \Phi, \chi, D)$ in a power series

$$\Psi(p, \Phi, \chi, D) = \Psi_0(p, \Phi, \chi) + D\Psi_1(p, \Phi, \chi) + D^2\Psi_2(p, \Phi, \chi) + ..., \tag{G.1}$$

where Ψ_0 is the constant of motion when $D = 0$ as found in equation (3.12) and Ψ_1, Ψ_2 are the first and second order corrections for the damped system, respectively. As will be shown, the exact solution for the first order damping correction Ψ_1 will be quite complicated rendering the second order or higher corrections not practical even if an exact solution exists. Therefore, for the remainder of the derivations the terms of order D^2 and above will be dropped from the series. To formulate the governing partial differential equation (PDE), one takes the total derivative of equation (G.1) w.r.t φ which results in

$$\frac{d\Psi}{d\varphi} = \frac{\partial\Psi_0}{\partial\varphi} + \frac{\partial\Psi_0}{\partial p}\frac{\partial p}{\partial\varphi} + D\left(\frac{\partial\Psi_1}{\partial\varphi} + \frac{\partial\Psi_1}{\partial p}\frac{\partial p}{\partial\varphi}\right) + ... = 0, \tag{G.2}$$

which is equal to zero since $\Psi = constant$ and $d\Psi = 0$. The term $\partial p/\partial\varphi$ was obtained earlier by dividing equation (3.6) by equation (3.7) resulting in

$$\frac{dp}{d\varphi} = \frac{p\sin(\Phi) + Dp^2}{\cos(\Phi) + 2p - 4\chi p^3}, \tag{G.3}$$

and this equation is no longer an exact first order differential equation when $D \neq 0$. The governing PDE's for the constants of motion Ψ_0 and Ψ_1 are obtained after plugging equation

(G.3) into equation (G.2) and equating powers of D

$$\frac{\partial \Psi_0}{\partial \varphi}\left(\cos(\Phi) + 2p - 4\chi p^3\right) + \frac{\partial \Psi_0}{\partial p} p \sin(\Phi) = 0, \tag{G.4}$$

$$\frac{\partial \Psi_1}{\partial \varphi}\left(\cos(\Phi) + 2p - 4\chi p^3\right) + \frac{\partial \Psi_1}{\partial p} p \sin(\Phi) + \frac{\partial \Psi_0}{\partial p} p^2 = 0. \tag{G.5}$$

As expected, the solution to equation (G.4) is the constant of motion for the undamped system found in equation (3.12). Using the result for Ψ_0 in equation (G.5), the first order correction Ψ_1 can be obtained in closed form with the aid of Mathematica and the result is summarized in Appendix H. Using the results for Ψ_0 and Ψ_1, the corrected constant of motion to first order can be constructed from equation (G.1)

$$\Psi = -\chi p^4 + p^2 + p\cos(\Phi) + D\Psi_1(p, \Phi, \chi) = c_2, \tag{G.6}$$

where c_2 is the constant of integration determined by the initial conditions (p_0, Φ_0), system parameters χ, and the damping coefficient D. Note that there are two separate Ψ_1 functions that satisfy equation (G.5), however, the function given in Appendix H contains the desired peak amplitude p_{max} which is corrected for small damping.

Shown in Fig. G.1 is the percent overshoot for zero initial conditions ($c_2 \approx 0$) which includes the analytical zero damping ($D = 0$) result from Fig. 3.6 as well as two additional curves for two levels of damping indicated in the Figure. Note that equation (H.1) cannot be evaluated at $p = 0$ or $\Phi = n\pi$ for all whole numbers n but this isn't a problem because as seen in Fig. 3.2 (a), (b), & (c), the damping slightly shifts the phase at which equation (G.6) is evaluated to get the peak amplitude so that it doesn't occur at $\Phi = 0$ or π as in the undamped case. The solid lines shown in Fig. G.1 are obtained by numerically solving

equation (G.6) for p_{max} after setting $c_2 = 0$ and evaluating Φ at its steady state value[1] using equation (3.10). The percent overshoot is then calculated by substituting p_{max} and the corresponding damped steady state amplitude obtained from either equation (D.1) or (D.2) depending on χ. The circles shown in Fig. G.1 are simulations of the average equations (equations (3.6) and (3.7)) for the two damping levels indicated in the Figure and undamped simulation is not shown since it was shown in Fig. 3.6. As may be expected, the damping increases the critical system parameter condition $\chi^\star = 4/27$ shown in Fig. 3.6 and this increases the system parameter regime for operation about the lower branch equilibria (**A**). The corrected constant of motion for small damping shows a good approximation up to about $D = 0.10$. Therefore, for small damping, equation (G.6) provides an alternative to simulations of the average equations when analyzing the transient response of a system. Lastly, it is noted the damping coefficient D of the scaled system (p, Φ) is related to the damping coefficient μ of the original system (r, Φ) through equation (3.8) and this can be related to the damping ratio ζ which will depend on the excitation frequency ω and the natural frequency ω_0.

[1]Note that this value of Φ satisfies $p' = 0$ (see equation (3.6)) which corresponds to the peak amplitude of a transient trajectory.

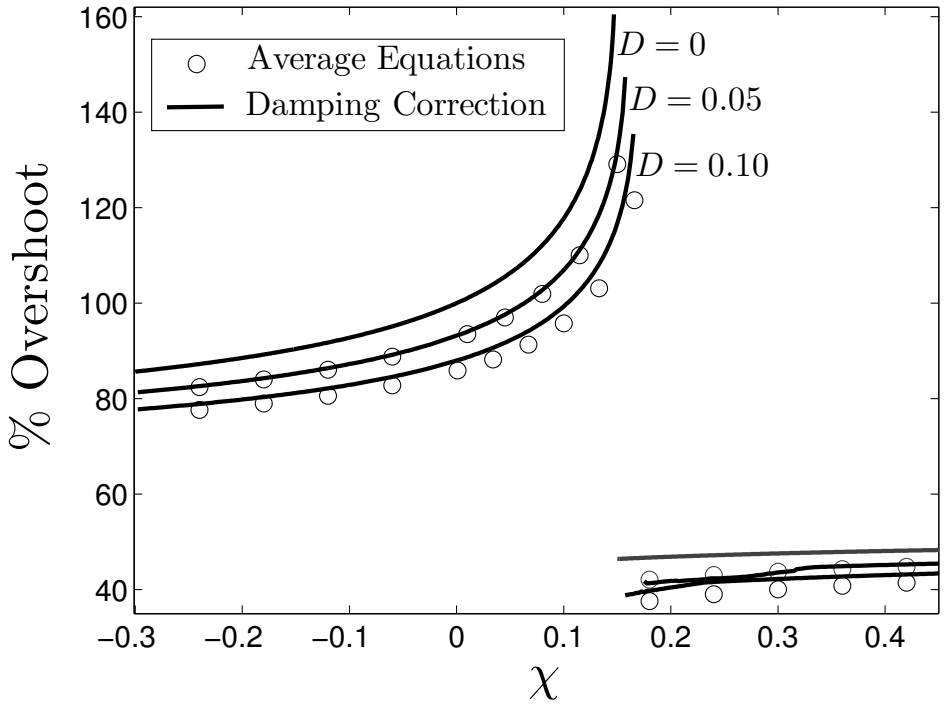

Figure G.1: Depicting the percent overshoot for the damped system subject to zero initial conditions. The damping levels include $D = 0$, $D = 0.05$, and $D = 0.10$ as labeled in the figure. The solid curves are obtained by numerically solving equation (G.6) which is the constant of motion for small damping. The circles are obtained by simulating the average equations (equations (3.6) and (3.7)) for the two levels of damping. The damping increases the critical system parameter $\chi^\star$ as shown in Fig. 3.6 and this increases the operating regime for a transient response about the lower branch equilibria (**A**). The constant of motion provides a very good approximation of the damped transient response of the system up to a damping level of about $D = 0.10$.

Appendix H

The Damped Transient Amplitude Response Polynomial

This appendix gives the exact analytical results needed for the percent overshoot calculation given in equation (3.11) when small damping ($D << 1$) is present. The damped percent overshoot calculation uses the peak transient amplitude and the steady state amplitude for a given set of system parameters χ, initial conditions (p_0, Φ_0), and the damping coefficient D. The peak amplitudes are obtained by numerically solving equation (G.6) where Ψ_1 is the first order correction for the damped system. There exists two solutions for Ψ_1 that satisfy the PDE in equation (G.5), but the solution containing the desired peak amplitude

information is given below

$$\Psi_1(p,\Phi,\chi) = \Bigg(-3(G_1-G_3)(G_1-G_4)(G_4-G_2)(G_2-p^2)^2 H_2 H_4 \chi + \tag{H.1}$$
$$-(G_1-G_4)H_1H_4(G_2-p^2)^2\Big(3G_2^2\chi - 3G_1G_4\chi + G_2(3G_1\chi+3G_4\chi-2) - 2p^2 +$$
$$+2\chi p^4 - 2p\cos(\Phi)\Big) +$$
$$+(G_1-G_2)\Bigg((G_1-G_4)H_3H_4(3G_1\chi+3G_2\chi+3G_3\chi+3G_4\chi-2)(G_2-p^2)^2 +$$
$$-(G_2-G_4)\Big(3G_4\chi p^4 - 3\chi p^6 + 3G_1\chi(G_3-p^2)(G_4-p^2) + 3G_3\chi p^2(p^2-G_4)\Big)\Bigg)\Bigg) /$$
$$\Big(2(G_1-G_2)(G_2-G_4)p\sin(\Phi)\Big),$$

where H_1, H_2, and H_3 are elliptic integrals of the first, second, and third kind, respectively; which are defined below

$$H_1 = F(\theta,m) = \int_0^\theta (1-m\sin(q)^2)^{-1/2}dq =$$
$$= F\left(\sin^{-1}\left(\sqrt{\frac{(G_2-G_4)(G_1-p^2)}{(G_1-G_4)(G_2-p^2)}}\right), \frac{(G_2-G_3)(G_1-G_4)}{(G_1-G_3)(G_2-G_4)}\right),$$
$$H_2 = E(\theta,m) = \int_0^\theta (1-m\sin(q)^2)^{1/2}dq =$$
$$= E\left(\sin^{-1}\left(\sqrt{\frac{(G_2-G_4)(G_1-p^2)}{(G_1-G_4)(G_2-p^2)}}\right), \frac{(G_2-G_3)(G_1-G_4)}{(G_1-G_3)(G_2-G_4)}\right),$$
$$H_3 = \Pi(n,\theta,m) = \int_0^\theta (1-n\sin(q)^2)^{-1}(1-m\sin(q)^2)^{-1/2}dq =$$
$$= \Pi\left(\frac{G_1-G_4}{G_2-G_4}, \sin^{-1}\left(\sqrt{\frac{(G_2-G_4)(G_1-p^2)}{(G_1-G_4)(G_2-p^2)}}\right), \frac{(G_2-G_3)(G_1-G_4)}{(G_1-G_3)(G_2-G_4)}\right),$$

and H_4 is defined as follows

$$H_4 = \sqrt{\frac{(G_1 - G_2)(G_3 - p^2)}{(G_1 - G_3)(G_2 - p^2)}} \sqrt{\frac{(G_1 - G_2)(G_2 - G_4)(G_1 - p^2)(G_4 - p^2)}{(G_1 - G_4)^2 (G_2 - p^2)^2}}.$$

To compute H_1 through H_4 and ultimately equation (H.1), the functions G_1 through G_4 are required which are defined below

$$\begin{aligned}
G_1 &= -\frac{1}{2\chi}\left(\sqrt{\frac{2}{\delta}\Big(J_2(1-\chi)-1\Big)+2-\frac{1}{3}\left(\frac{J_1}{2^{1/3}}+4J_2+\frac{J_3}{J_1}\right)}-\delta+1\right),\\
G_2 &= \frac{1}{2\chi}\left(\sqrt{\frac{2}{\delta}\Big(J_2(1-\chi)-1\Big)+2-\frac{1}{3}\left(\frac{J_1}{2^{1/3}}+4J_2+\frac{J_3}{J_1}\right)}-\delta+1\right),\\
G_3 &= -\frac{1}{2\chi}\left(\sqrt{\frac{2}{\delta}\Big(J_2(\chi-1)+1\Big)+2-\frac{1}{3}\left(\frac{J_1}{2^{1/3}}+4J_2+\frac{J_3}{J_1}\right)}+\delta+1\right),\\
G_4 &= \frac{1}{2\chi}\left(\sqrt{\frac{2}{\delta}\Big(J_2(\chi-1)+1\Big)+2-\frac{1}{3}\left(\frac{J_1}{2^{1/3}}+4J_2+\frac{J_3}{J_1}\right)}+\delta+1\right),
\end{aligned}$$

where

$$\delta = \sqrt{1+\frac{1}{3}\left(\frac{J_1}{2^{1/3}}-2J_2+\frac{J_3}{J_1}\right)}. \tag{H.2}$$

Finally, to compute the functions G_1 through G_4, the functions J_1 through J_3 are required which are defined below

$$
\begin{aligned}
J_1 =&\Bigg(2 - 18\chi + 27\chi^2 - 24\chi p^2 + 72\chi^2 p^2 + 120\chi^2 p^4 - 72\chi^3 p^4 - 320\chi^3 p^6 + 480\chi^4 p^8 + \\
&- 384\chi^5 p^{10} + 128\chi^6 p^{12} + \\
&- 24\chi p\Big(1 + 24\chi^2 p^4 - 32\chi^3 p^6 + 16\chi^4 p^8 - \chi(3 + 8p^2)\Big)\cos(\Phi) + \\
&+ 96\chi^2 p^2 (1 - 2\chi p^2)^2 \cos(\Phi)^2 - 128\chi^3 p^3 \cos(\Phi)^3 + 3\sqrt{3}\Bigg(\chi^3\Big(896\chi^3 p^8 - 768\chi^4 p^{10} + \\
&+ 256\chi^5 p^{12} - 4(1 + 4p^2) - 16\chi^2 p^4 (9 + 32p^2) + 9\chi(3 + 16p^2 + 16p^4) + \\
&- 16p\Big(1 + 64\chi^2 p^4 - 96\chi^3 p^6 + 48\chi^4 p^8 - \chi(9 + 16p^2)\Big)\cos(\Phi) + \\
&+ 128\chi p^2 (1 - 6\chi p^2 + 6\chi^2 p^4)\cos(\Phi)^2 - 256\chi^2 p^3 \cos(\Phi)^3\Big)\Bigg)^{1/2}\Bigg)^{1/3}, \\
J_2 =&\Big(1 + 2\chi p\Big(p - \chi p^3 + \cos(\Phi)\Big)\Big), \\
J_3 =&2^{1/3}\Big(1 + 24\chi^2 p^4 - 32\chi^3 p^6 + 16\chi^4 p^8 - 2\chi(3 + 4z^2) + \\
&- 8\chi p(1 - 2\chi p^2)^2 \cos(\Phi) + 16\chi^2 p^2 \cos(\Phi)^2\Big).
\end{aligned}
$$

BIBLIOGRAPHY

BIBLIOGRAPHY

[1] Light-Duty Vehicle Greenhouse Gas Emission Standards and Corporate Average Fuel Economy Standards; Final Rule. *Federal Register*, 75:25324–25728 (May 7, 2010).

[2] T. Abbasov and A. R. Bahadir. The investigation of the transient regimes in the nonlinear systems by the generalized classical method. *Mathematical Problems in Engineering*, 5:503–519, 2005.

[3] M. Albright, T. Crawford, and F. Speckart. Dynamic testing and evaluation of the torsional vibration absorber. In *SAE Paper No. 942519*, 1994.

[4] A. S. Alsuwaiyan. *Performance, Stability, and Localization of Systems of Vibration Absorbers*. PhD thesis, Michigan State University, 1999.

[5] A. S. Alsuwaiyan and S. W. Shaw. Performance and dynamic stability of general-path centrifugal pendulum vibration absorbers. *Journal of Sound and Vibration*, 252(5):791–815, 2002.

[6] A. S. Alsuwaiyan and S. W. Shaw. Steady-state response of systems of nearly-identical torsional vibration absorbers. *Journal of Vibration and Acoustics*, 125:80–87, 2003.

[7] A. K. Bajaj and J. M. Johnson. On the amplitude dynamics and crisis in resonant motion of stretched strings. *Philosophical Transactions: Physical Sciences and Engineering*, 338:1–41, 1992.

[8] W. E. Boyce and R. C. DiPrima. *Elementary Differential Equations and Boundary Value Problems*. John Wiley & Sons, Inc., 2000.

[9] V. K. Chandrasekar, M. Senthilvelan, and M. Lakshmanan. On the complete integrability and linearization of certain second-order nonlinear ordinary differential equations. *Proceedings of the Royal Society A*, 461:2451–2476, 2005.

[10] V. K. Chandrasekar, M. Senthilvelan, and M. Lakshmanan. On the lagrangian and hamiltonian description of the damped linear harmonic oscillator. *Journal of Mathematical Physics*, 43, 2007.

[11] C. P. Chao, C. T. Lee, and S. W. Shaw. Stability of the unison response for a rotating system with multiple centrifugal pendulum vibration absorbers. *Journal of Applied Mechanics*, 64:149–156, 1997.

[12] C. P. Chao and S. W. Shaw. The effects of imperfections on the performance of the subharmonic vibration absorber system. *Journal of Sound and Vibration*, 215(5):1065–1099, 1998.

[13] C. P. Chao and S. W. Shaw. The dynamic response of multiple pairs of subharmonic pendulum vibration absorbers. *Journal of Sound and Vibration*, 231(2):411–431, 2000.

[14] C. P. Chao, S. W. Shaw, and C. T. Lee. Non-unison dynamics of multiple centrifugal pendulum vibration absorbers. *Journal of Sound and Vibration*, 204(5):769–794, 1997.

[15] F. H. Clauser. The transient behavior of nonlinear systems. *IRE TRANSACTIONS ON CIRCUIT THEORY*, 7:446–458, 1960.

[16] H. H. Denman. Remarks on brachistochrone-tautochrone problems. *American Journal of Physics*, 53:781–782, 1985.

[17] H. H. Denman. Tautochronic bifilar pendulum torsion absorbers for reciprocating engines. *Journal of Sound and Vibration*, 159(2):251–277, 1992.

[18] H. H. Denman. Approximate invariants and lagrangians for autonomous, weakly nonlinear systems. *International Journal of Non-Linear Mechanics*, 29:409–419, 1994.

[19] H. H. Denman. Approximate invariants and lagrangians for autonomous, weakly nonlinear systems - ii. linear friction. *International Journal of Non-Linear Mechanics*, 33:301–314, 1998.

[20] M. D'Souza, A. Kumar, and R. D'Souza. Non-linear resonant transient and steady-state response in a classical model. *Journal of Modern Optics*, 28:1039 – 1050, 1981.

[21] D. H. Eckhardt. A nonlinear analysis of the moon's physical libration in longitude. *The Moon*, 2:309–319, 1971.

[22] A. G. Falkowski, M. R. McElwee, and M. A. Bonne. Design and development of the daimlerchrysler 5.7l hemisr engine multi-displacement cylinder deactivation system. In *SAE Non-Conference Specific Technical Papers*, 2004.

[23] H. Frahm. Device for damping of bodies. United State Patent No. 989958, 1911.

[24] B. K. Geist. Hingemaster: Calculating bifilar cut-outs for a pendulum absorber. PCTR7380 (Chrysler technical report), 2007.

[25] A. Gelb and W. E. Vander Velde. *Multiple-Input Describing Functions and Nonlinear System Design*. McGraw Hill Book Company, 1968.

[26] A. G. Haddow and S. W. Shaw. Centrifugal pendulum vibration absorbers: An experimental and theoretical investigation. *Nonlinear Dynamics*, 34:293–307, 2003.

[27] J. P. Den Hartog. *Tuned Pendulums as Torsional Vibration Eliminators*, pages 17–26. Stephen Timoshenko 60th Anniversary Volume. New York: The Macmillan Company, 1938.

[28] J. P. Den Hartog. *Mechanical Vibrations*. Dover, 1985.

[29] D. F. Hill. Transient and steady-state amplitudes of forced waves in rectangular basins. *16th ASCE Engineering Mechanics Conference*, 2003.

[30] Y. Ishida, T. Inoue, T. Fukami, and M. Ueda. Torsional vibration suppression by roller type centrifugal vibration absorbers. *Journal of Vibration and Acoustics*, 131, 2009.

[31] W. Ker Wilson. *Practical Solutions of Torsional Vibration Problems*, volume IV, chapter XXX. Chapman and Hall Ltd, London, 3rd edition, 1968.

[32] A. Kozmin, Yu. Mikhlin, and C. Pierre. Transient in a two-dof nonlinear system. *Nonlinear*, 51:141–154, 2008.

[33] C. T. Lee and S. W. Shaw. On the counteraction of periodic torques in rotating systems using centrifugally driven vibration absorbers. *Journal of Sound and Vibration*, 191(5):695–719, 1996.

[34] C. T. Lee and S. W. Shaw. The nonlinear dynamic response of paired centrifugal pendulum vibration absorbers. *Journal of Sound and Vibration*, 203(5):731–743, 1997.

[35] C. T. Lee, S. W. Shaw, and V. T. Coppola. A subharmonic vibration absorber for rotating machinery. *Journal of Vibration and Acoustics*, 119:590–595, 1997.

[36] G. Lopez. One-dimensional autonomous systems and dissipative systems. *Annals of Physics*, 251:372–383, 1996.

[37] G. Lopez, X. E. Lopez, and H. Hernandez. One-dimensional relativistic dissipative system with constant force and its quantization. *International Journal of Theoretical Physics*, 45:743–752, 2006.

[38] J. F. Madden. Constant frequency bifilar vibration absorber. United States Patent No. 4218187.

[39] L. I. Manevitch and A. I. Musienko. Limiting phase trajectories and energy exchange between anharmonic oscillator and external force. *Nonlinear Dynamics*, 58:633–642, 2009.

[40] E. Matta and A. De Stefano. Robust design of mass-uncertain rolling-pendulum tmds for the seismic protection of buildings. *Mechanical Systems and SignalProcessing*, 23:127147, 2009.

[41] E. Meissner. Equalising the speed of rotating shafting by oscillating systems. *Proc. 3rd International Congress for Applied Mechanics, Stockholm*, 3:199, 1930.

[42] Y. Mikhlin, G. Rudnyeva, T. Bunakova, and N. Perepelkin. Transient in 2-dof nonlinear systems. *Modeling, Simulation and Control of Nonlinear Engineering Dynamical Systems*, pages 129–140, 2009.

[43] R. J. Monroe. A nearly linear relationship between the angular encoder measurement and the resulting arc-length for non-circular paths. Technical report, Michigan State University, 2011.

[44] R. J. Monroe. Notes on transient dynamics of nonlinear oscillators. Technical report, Michigan State University, 2011.

[45] R. J. Monroe and S. W. Shaw. Nonlinear transient dynamics of pendulum torsional vibration absorbers. In *Proceedings of the ASME 2011 International Design Engineer-*

ing Technical Conferences & Computers and Information in Engineering Conference (IDETC/CIE 2011), 2011. In review.

[46] R. J. Monroe and S. W. Shaw. Nonlinear transient dynamics of pendulum torsional vibration absorbers, part i: Theory. Technical report, To be submitted to The Journal of Vibration and Acoustics, 2011.

[47] R. J. Monroe and S. W. Shaw. Nonlinear transient dynamics of pendulum torsional vibration absorbers, part ii: Experiment. Technical report, To be submitted to The Journal of Vibration and Acoustics, 2011.

[48] R. J. Monroe and S. W. Shaw. On the transient response of forced nonlinear oscillators. Technical report, Submitted to Nonlinear Dynamics, 2011.

[49] R. J. Monroe, S. W. Shaw, A. G. Haddow, and B. K. Geist. Accounting for roller dynamics in the design of bifilar torsional vibration absorbers. In *Proceedings of the ASME 2009 International Design Engineering Technical Conferences & Computers and Information in Engineering Conference (IDETC/CIE 2009)*, 2009.

[50] R. J. Monroe, S. W. Shaw, A. G. Haddow, and B. K. Geist. Accounting for roller dynamics in the design of bifilar torsional vibration absorbers. Technical report, Accepted for Publication in the Journal of Vibration and Acoustics, 2010.

[51] A. H. Nayfeh and D. T. Mook. *Nonlinear Oscillations*. Wiley, 1995.

[52] T. Nester, A. Haddow, P. Schmitz, and S. W. Shaw. Experimental observations of centrifugal pendulum vibraion absorbers. In *10th International Symposium on Transport Phenomena and Dynamics of Rotating Machinery (ISROMAC-10), Honolulu, Hawaii, March*, 2004.

[53] T. Nester, A. G. Haddow, and S. W. Shaw. Experimental investigation of a system with multiple nearly identical centrifugal pendulum vibration absorbers. In *Proceedings of the ASME 19th Biennial Conference on Mechanical Vibration and Noise*, Chicago, Illinois, 2003.

[54] T. M. Nester. Experimental investigation of circular path centrifugal pendulum vibration absorbers. M.S. thesis, Michigan State University, East Lansing, MI, 2002.

[55] T. M. Nester, A. G. Haddow, S. W. Shaw, J. E. Brevick, and V. J. Borowski. Vibration reduction in variable displacement engines using pendulum absorbers. In *Proceedings of*

the SAE Noise and Vibration Conference and Exhibition, number 2003-01-1484, Traverse City, Michigan, 2003.

[56] D. E. Newland. Nonlinear aspects of the performance of centrifugal pendulum vibration absorbers. *Journal of Engineering for Industry*, 86:257–263, 1964.

[57] B. J. Olson. *Order-Tuned Vibration Absorbers for Cyclic Systems with Applications to Turbomachinery*. PhD thesis, Michigan State University, 2006.

[58] M. Orlowski. Transient behavior of centrifugal pendulum vibration absorbers with tautochronic epicycloidal paths. Master's thesis, Michigan State University, 2007.

[59] D. Palmer. Theoretical and experimental investigation into the transient behavior of centrifugal pendulum vibration absorbers. M.S. thesis, Michigan State University, East Lansing, MI, 2005.

[60] R. Gladwin Pradeep, V. K. Chandrasekar, M. Senthilvelan, and M. Lakshmanan. Non-standard conserved hamiltonian structures in dissipative/damped systems: Nonlinear generalizations of damped harmonic oscillator. *Journal of Mathematical Physics*, 50, 2009.

[61] F. N. H. Robinson. Experimental observation of the large-amplitude solutions of duffing's and related equations. *IMA Journal of Applied Mathematics*, 42:177–201, 1989.

[62] B. Salomon. French Patent No. 748909, July 1933.

[63] R. R. R. Sarazin. British Patent No. 382787, November 1932.

[64] H. Sato and K. Asada. Laplace transform transient analysis of a non-linear system. *Journal of Sound and Vibration*, 121:473–479, 1988.

[65] P. M. Schmitz. Experimental investigation into epicycloidal centrifugal pendulum vibration absorbers. MS Thesis, Michigan State University, East Lansing, MI, 2003.

[66] S. W. Shaw. Engine excitation harmonics and applications to MDS transitions. Technical report, Michigan State University, 2007.

[67] S. W. Shaw and B. Balachandran. A review of nonlinear dynamics of mechanical systems in year 2008. *JSME Journal of System Design and Dynamics*, 2:611–640, 2008.

[68] S. W. Shaw and B. K. Geist. Tuning for performance and stability in systems of nearly-tautochronic torsional vibration absorbers. *Journal of Vibration and Acoustics*, 132, 2010.

[69] S. W. Shaw, M. B. Orlowski, and A. G. Haddow. Transient dynamics of centrifugal pendulum vibration absorbers. In *The 12th International Symposium on Transport Phenonmenon and Dynamics of Rotating Machinery*, 2008.

[70] S. W. Shaw, P. M. Schmitz, and A. G. Haddow. Tautochronic vibration absorbers for rotating systems. *Journal of Computational and Nonlinear Dynamics*, 1:283–293, 2006.

[71] R. A. Struble and S. M. Yionoulis. General perturbational solution of the harmonically forced duffing equation. *Archive for Rational Mechanics and Analysis*, 9:422–438, 1962.

[72] B. N. Taylor and C. E. Kuyatt. Guidelines for evaluating and expressing the uncertainty of nist measurement results. Technical report, National Institute of Standards and Technology (NIST), NIST Technical Note 1297 (1994 Edition).

[73] E. S. Taylor. Eliminating crankshaft torsional vibration in radial aircraft engines. *SAE Journal*, 38:81–89, 1936.

[74] W. T. Thomson and M. D. Dahleh. *Theory of Vibration with Applications*. Prentice Hall, 1997.

[75] B. J. Vidmar. The effects of coulomb friction on the performance of centrifugal pendulum vibration absorbers. Master's thesis, Michigan State University, 2009.

[76] B. J. Vidmar, B. F. Feeny, S. W. Shaw, A. G. Haddow, B. K. Geist, and N. J. Verhanovitz. The effects of coulomb friction on the performance of centrifugal pendulum vibration absorbers. Technical report, Submitted to Nonlinear Dynamics, 2011.

[77] M. A. Wachs. The main rotor bifilar absorber and its effect on helicopter reliability/maintainability. *SAE Technical Paper Series 730894*, 1973.